

FEEDBACK CONTROL OF OPTICALLY TRAPPED NANOPARTICLES
AND ITS APPLICATIONS

A Dissertation

Submitted to the Faculty

of

Purdue University

by

Jaehoon Bang

In Partial Fulfillment of the

Requirements for the Degree

of

Doctor of Philosophy

May 2020

Purdue University

West Lafayette, Indiana

THE PURDUE UNIVERSITY GRADUATE SCHOOL
STATEMENT OF DISSERTATION APPROVAL

Dr. Tongcang Li, Chair

Department of Physics and Astronomy, and School of Electrical and Computer
Engineering

Dr. Alexandra Boltasseva

School of Electrical and Computer Engineering

Dr. Francis Robicheaux

Department of Physics and Astronomy

Dr. Minghao Qi

School of Electrical and Computer Engineering

Approved by:

Dr. Dimitrios Peroulis

Head of the School Graduate Program

To my family.

ACKNOWLEDGMENTS

I remember that I was always dreaming of this moment since I had decided to challenge myself after my first attempt which ended up to be a failure. It was not an easy call and I had to regret the decision once in a while during my PhD. Life cannot be always fruitful but the fact came to me with a great pain. After the long suffering, finally I am here writing the acknowledgment of my thesis. And I am not surprised though my heart is not just full of delight as I imagined before, because the past six years allowed me to be more humble and matured. Today I only can think of all the helps and supports that made me to endure the time.

First of all, I want to express my deepest gratitude to my advisor, Professor Tongcang Li for his true support and guidance throughout my Ph.D studies. His patience and thoughtful advice always encouraged me when I was in trouble. I also want to emphasize how grateful I am to Professor Francis Robiceaux, for his precious advice and insightful discussions. I have no doubt that my research improved a step further because of the fruitful and rich discussions. I am truly thankful to my committee members, Professor Alexandra Boltasseva and Professor Minghao Qi, for their warm support.

Life would be much harder without the encouragement from all of my friends here at Purdue university. It is one of my best luck to have Jonghoon as a lab mate and a true friend. He is not just a perfect colleague but also one of the few person that I can fully rely on. It is really hard to express all my appreciation to him. There are countless people whom I am grateful to including my lab mates, all the members of PKTC and DKUMC. Especially, I want to express my heartfelt thanks to my close friends in the Monday tennis group. They are incomparably valuable to me and made it possible for me to enjoy the life here in West Lafayette.

Last but not the least, I want to give my deepest love to my family. I am thankful to my parents who gave me endless love and support. Their belief on me always gave me hope and power to go through the obstacles. It will be impossible to thank enough to my wife Jihye for her devotion to me and my family. Nothing would be possible without her love and support as a wife and mother. I want to share the joy with my little one Ellie, who became the motivation of my life. I am giving all my credit to Jihye and Ellie because they deserve it.

Above all, I confess with all my hearts that He is the One and the only One who paves the way and maketh me to lie down in green pastures. Thank You for everything.

April 25, 2020

Jaehoon Bang

TABLE OF CONTENTS

	Page
LIST OF FIGURES	viii
ABBREVIATIONS	xiv
ABSTRACT	xv
1 Introduction	1
1.1 Optical tweezers	1
1.2 Generation of complex optical tweezers and its applications	3
1.3 Levitated optomechanics using optical tweezers	5
1.4 Contents of this dissertation	5
2 Experimental realization of Feynman's ratchet	9
2.1 Motivation	9
2.1.1 Feynman's ratchet and pawl	9
2.1.2 Experimental efforts to realize Feynman's ratchet	9
2.2 Realization of Feynman's ratchet and pawl	10
2.2.1 Periodic lattice model of Feynman's ratchet	10
2.2.2 Generation of a periodic optical lattice	11
2.2.3 Experimental realization of Feynman's ratchet with feedback control	17
2.2.4 Feynman's ratchet as a microscopic heat engine	22
2.3 Conclusion	27
3 Levitation of nanodumbbell and observation of torsional motion	29
3.1 Motivation	29
3.2 Experimental Setup	30
3.3 Creating and loading nanodumbbells	34
3.4 Characteristics of nanodumbbells inside an optical trap	37

	Page
3.5 Determination of a levitated nanodumbbell	40
4 Feedback cooling of a nanodumbbell in five degrees of freedom	44
4.1 Motivation	44
4.2 Optical feedback cooling of a levitated nanoparticle	46
4.2.1 Feedback cooling of a mechanical oscillator	46
4.2.2 Active feedback cooling of a levitated particle	47
4.3 Force feedback control loop	50
4.3.1 Band-pass filter	53
4.3.2 Differential circuit	55
4.3.3 Variable gain amplifier	57
4.3.4 Unity gain inverting amplifier	59
4.3.5 Summing amplifier	59
4.4 Feedback cooling of a levitated nanoparticle	62
4.4.1 3D Feedback cooling of a levitated nanosphere	62
4.4.2 5D Feedback cooling of a levitated nanodumbbell	68
4.5 Conclusion	74
5 Rotation coupled nonlinear motion	75
5.1 Motivation	75
5.2 Experimental description	76
5.3 Nonlinearity of torsional motion and rotation coupling	76
5.4 Rotation coupled torsional motion	83
5.5 Conclusion	84
6 Future Work	88
6.1 Improving motional cooling	88
6.2 Engineering of a levitated particle	88
6.3 On-chip optical tweezer	91
REFERENCES	92

LIST OF FIGURES

Figure	Page
1.1 Brief schematic of an optical tweezer.	2
1.2 Typical optics configuration to create complex optical tweezers. $\lambda/2$: half-wave plate, DM: dichroic mirror, Obj.: objective lens, PD: photo diode. . .	4
1.3 Example of a ring trap generated using a 2-axis galvo-mirror.	6
1.4 Example of multiple optical tweezers generated using acousto-optic deflector (AOD).	7
2.1 Two modes (disengaged mode and engaged mode) of ratchet and pawl corresponding to each model (top: Jarzynski's model, bottom: Feynman's model). T_A : temperature generated using computer feedback control, T_B : temperature of the environment.	10
2.2 Setup of the experiment. A silica nanosphere (with a diameter of 780 nm) emerged in water was used for the experiment.	12
2.3 Picture of the optics setup. The red lines indicate the path of the trapping laser.	13
2.4 Schematics of generating 1D potential trap. Thin grey curves indicate each optical tweezer approximated in Gaussian. Green dashed boxes specify the region used in the experiment.	14
2.5 Calibration of a 1D potential trap. Example of a uniform flat potential before calibration (blue circles) and after calibration (red squares). . . .	15
2.6 Profile of potential energy for mode 1 (disengaged mode, red hollow squares) and mode 2 (engaged mode, blue filled circles). The black lines are used for simulation and are determined by fitting the measured potential. The corresponding temperature is 296 K. The asymmetry of the sawtooth potential is about 1:3.	18
2.7 50 trajectories (back ground) and the average (thick blue) of the particle when the virtual heat bath (T_A) is 30 K. The average displacement at 60 sec is $\langle \Delta x \rangle = 2.1 \pm 0.6 \mu m$	19
2.8 50 trajectories (back ground) and the average (thick blue) of the particle when the virtual heat bath (T_A) is 296 K. The displacement is $\langle \Delta x \rangle = -0.1 \pm 0.9 \mu m$	20

Figure	Page
2.9 50 trajectories (back ground) and the average (thick blue) of the particle when (T_A) is 3000 K . The displacement is $\langle \Delta x \rangle = -4.5 \pm 0.9 \mu m$	21
2.10 Velocity of the particle for different external loads. Each data point corresponds to an average of 50 trajectories. Blue squares show the result with a positive load ($-0.05 k_B T_B / \mu m$ slope), red circles without any load and black triangles with a negative load ($-0.14 k_B T_B / \mu m$ slope). Solid lines are simulation results.	23
2.11 Work demonstration using the optical ratchet.	25
2.12 Heat and entropy production of the optical ratchet.	26
3.1 Optically levitated nanodumbbell (b) as an analogous system of Cavendish torsion balance (a). The restoring force of a levitated nanodumbbell is provided from the linearly polarized optical tweezer whereas the classical Cavendish torsion balance uses a torsion wire [53].	29
3.2 Overall feature of the setup. A 1064 nm laser (Mephisto, Coherent, Inc.) is used for trapping. A $\frac{\lambda}{2}$ waveplate is inserted after the fiber to change the polarization direction of the trapping laser. A high NA objective lens ($NA = 0.85$, LCPLN100XIR, Olympus Corp.) is installed inside a customized vacuum chamber. The trapping laser then is collected with a condensor lens (C330TMD-B, Thorlabs, Inc.) and guided to four balanced detectors (PDB415C-AC or PDB425C-AC, Thorlabs, Inc.). A CMOS camera (DCC1545M, Thorlabs, Inc.) is installed at the side and a CCD camera (BFLY-U3-13S2C-CS, FLIR Systems, Inc.) is aligned at the back of the objective lens.	31
3.3 Example images of trapped SiO_2 particles observed with different cameras. 33	
3.4 SEM image of chemically synthesized nanodumbbells. Singlets and trimers are also observable. The size of a single sphere is around 160 nm . The scale bar indicates 500 nm	35
3.5 Optical image showing the sequence of physical creation of a nanodumbbell. Two individual particles are first trapped using two optical twizzers (top). One trap is moved closer to the other (middle) until the two traps merge (bottom).	36
3.6 Configuration of a nanodumbbell inside an optical trap. In this experiment, z - y' - z'' convention is used to define the Euler angles [89].	37

Figure	Page
3.7	Shape of trapping potentials as a function of displacement. The blue line indicates the potential of a translational motion along the y axis. The red line presents the potential of a torsional vibration in α direction. For direct comparison, the radius $r = 85$ nm is multiplied to the angle α for the rotational (torsional) potential. Inset is a SEM image of a nanodumbbell. 39
3.8	Power spectral density (PSD) measured for a nanodumbbell consisting of two 170 nm silica spheres. PSDs obtained from four different detectors x , y , z and α are shown together. The PSD for the β motion is achievable from the high frequency part of the x detector. These PSDs are taken at a pressure of 3×10^{-3} Torr with x , y and z motion cooling. The data acquisition time is 1 sec. 40
3.9	Ratio of damping rates for various shapes of nanoparticles [53]. 41
3.10	Example of Power spectral densities for (a) nanodumbbell and (b) nanosphere trapped with our system. Each PSDs corresponds to x (blue), y (orange), z (yellow), α (purple) and β (higher frequency part of blue) respectively. Different band-pass filters are applied for each degree of freedom. 43
4.1	Schematic illustration of 5D cooling. A 1064 nm laser is used to levitate a nanodumbbell in vacuum. Cooling lasers and their directions of propagation are illustrated in green (x -cooling laser, 532 nm) and orange (y - and z -cooling lasers, 976 nm). The polarization directions of the y - and z -cooling lasers are tilted to form an angle of about 10 degrees with respect to the polarization direction of the trapping laser. The polarization direction of the x -cooling laser is parallel to y axis. 49
4.2	Photo of optics configuration inside the vacuum chamber. The trapping laser (red arrow) is guided through a high NA objective lens. Each cooling laser are focused to the trapping position using aspheric lenses: 1) x -cooling laser: C280TMD-A, Thorlabs, Inc., 2) y -cooling laser: C280TMD-B, Thorlabs, Inc. and 3) z -cooling laser: C330TMD-B, Thorlabs, Inc. . . . 51
4.3	Schematic of the setup showing the sequence of cooling of a levitated nanodumbbell. The home built analog circuit is indicated with the dashed lines. The signal obtained from the balanced detector for both x and β motions is split into two and fed into two different derivative circuits to generate the corresponding cooling signals for the motion in x and β directions. After processed thorough the circuit, signals corresponding to α and β motions are added to the signals for z and y motions, respectively (Fig. 4.1). 52
4.4	Schematic of a first order active band-pass filter 54

Figure	Page
4.5 Schematic of a differential circuit. This circuit calculates the velocity of a levitated particle based on the displacement signal acquired from the balanced detector.	56
4.6 Schematic of a variable gain amplifier. This circuit amplifies the input signal V_{in} . The gain of the circuit can be controlled by tuning the potentiometer.	57
4.7 Voltage signal acquired from four balanced photo-detectors. The voltage oscillation of each plot represents the corresponding oscillation of each degree of freedom. 1ms of data is shown in the plot.	58
4.8 Relation between the motion of the particle and the feedback signal. The feedback signal has to be shifted by $\frac{\pi}{2}$ from the motional signal to achieve cooling.	60
4.9 Schematic of a summing amplifier. V_{out} can be determined as $V_{out} = -\frac{R_f}{R_1}[V_{in,1} + V_{in,2} + V_{in,3}]$ since we set $R_1 = R_2 = R_3$. A potentiometer is used for R_f to control the amplitude of the signal.	61
4.10 Experimentally measured damping rates of a silica nanosphere at different pressures. Each data point is a mean of five measurements and the error bars indicate the standard deviations. The lines show linear fittings of the data sets for different directions.	63
4.11 Motional cooling of a levitated SiO_2 nanosphere in x direction. The PSD in red is the case when the feedback cooling is not applied to the system. The pressure at this moment was 9.7 Torr. The PSD in blue shows the case when feedback cooling is applied at low pressure (6.0×10^{-4} Torr). The black dashes represent the fitting for each PSDs.	65
4.12 Motional cooling of a levitated SiO_2 nanosphere in y direction. The PSD in red is when the feedback cooling is not applied to the system. The corresponding pressure is 9.7 Torr. The PSD in blue is the case when feedback cooling is applied at the pressure of 6.0×10^{-4} Torr. The black dashes show the fitting for each PSDs.	66
4.13 Translational cooling of a levitated SiO_2 nanosphere in z direction. The red PSD shows when the feedback cooling is not applied at the pressure of 9.7 Torr. The PSD in blue is the case when feedback cooling is applied at the pressure of 6.0×10^{-4} Torr. The black dashes show the fitting for each PSDs.	67

Figure	Page
4.14 Translational cooling of a levitated SiO_2 nanodumbbell in x direction. The blue PSD shows when feedback cooling is not applied at the pressure of 1 <i>Torr</i> . The PSD in red is the case when feedback cooling is applied at the pressure of 1.8×10^{-3} <i>Torr</i> . The green PSD shows the noise level of the system when nothing is trapped. The black dashes show the fitting for each PSDs.	69
4.15 Translational cooling of a levitated SiO_2 nanodumbbell in y direction. The blue PSD shows when feedback cooling is not applied at the pressure of 1 <i>Torr</i> . The PSD in red is the case when feedback cooling is applied at the pressure of 1.8×10^{-3} <i>Torr</i> . The green PSD shows the noise level of the system when nothing is trapped. The black dashes show the fitting for each PSDs.	70
4.16 Translational cooling of a levitated SiO_2 nanodumbbell in z direction. The blue PSD shows when feedback cooling is not applied at the pressure of 1 <i>Torr</i> . The PSD in red is the case when feedback cooling is applied at the pressure of 1.8×10^{-3} <i>Torr</i> . The green PSD shows the noise level of the system when nothing is trapped. The black dashes show the fitting for each PSDs.	71
4.17 Torsional cooling of a levitated SiO_2 nanodumbbell in α direction. The blue PSD shows when feedback cooling is not applied at the pressure of 1 <i>Torr</i> . The PSD in red is the case when feedback cooling is applied at the pressure of 1.8×10^{-3} <i>Torr</i> . The green PSD shows the noise level of the system when nothing is trapped. The black dashes show the fitting for each PSDs.	72
4.18 Torsional cooling of a levitated SiO_2 nanodumbbell in β direction. The blue PSD shows when feedback cooling is not applied at the pressure of 1 <i>Torr</i> . The PSD in red is the case when feedback cooling is applied at the pressure of 1.8×10^{-3} <i>Torr</i> . The green PSD shows the noise level of the system when nothing is trapped. The black dashes show the fitting for each PSDs.	73
5.1 Relative frequency fluctuations of the two torsional hybrid modes ω_+ (red) and ω_- (blue) are shown in comparison with the c.m. motion in y direction (grey) at the pressure of 5 <i>Torr</i> . The frequency for each data points are determined from a 2 <i>ms</i> signal data. The frequency of the two torsional hybrid modes are normalized by the average of the two ($\frac{\omega_+ + \omega_-}{2}$) and the c.m. motion is normalized by the average of itself.	78

Figure	Page	
5.2	Relative frequency fluctuations of the two torsional hybrid modes ω_+ (red) and ω_- (blue). Grey shows the c.m. motion along y -direction. The data was taken at the pressure of 3.33×10^{-3} Torr. The frequency for each points are determined from a 2 ms signal data. As in Fig. 5.1, the frequency of the two torsional hybrid modes are normalized by the average of the two ($\frac{\omega_+ + \omega_-}{2}$) and the c.m. motion is normalized by the average of itself.	79
5.3	Relative frequency fluctuations for translational motions and torsional motions at 3.33×10^{-3} Torr. The black curve indicates the frequency fluctuation of x -direction and the blue curve shows the frequency fluctuation of y -direction. The characteristic frequency fluctuation for α -direction is shown in green. The red plot shows the scaled frequency change for ω_t based on the scaling factor retrieved from eq. 5.2.	80
5.4	Frequency correlations between different degree of freedoms. The correlations between different modes are plotted as a function of pressure. Each data point corresponds to an average of correlation for five sets of measurement. For each measurement, correlation is calculated from 500 PSDs. The error bar shows the standard deviation of the data set.	82
5.5	Experimental results of rotation coupled torsional motions in α (grey) and β (red) directions. The PSDs are taken at 3×10^{-3} Torr and the measurement time is 2 ms.	85
5.6	Simulation results of rotation coupled torsional motions in α (purple) and β (yellow) directions. The simulated time of motion is 1 ms and random noise is added to the background to mimic the experimental situation. . .	86
6.1	Power spectral densities of a levitated nano trimer. PSDs of each direction are plotted in blue (x & β), orange (y), yellow (z) and purple (α). Black curve shows the fitting for x , y and z . The signal for the PSD is taken for 1 s.	89
6.2	Torsional cooling of a levitated trimer. PSDs of a torsional motion in α -direction are plotted for a situations without cooling at 10 Torr (red) and with cooling at 1.7×10^{-3} Torr (blue). The black dashed lines show the Lorentzian fitting.	90

ABBREVIATIONS

1D	one dimension
3D	three dimension
5D	five dimension
DOF	degree of freedom
AOD	acousto-optic deflector
AOM	acousto-optic modulator
EOM	electro-optic modulator
CCD	charge-coupled device
CMOS	complementary metal–oxide–semiconductor
LED	light-emitting diode
RF	radio frequency
SLM	spatial light modulator
c.m.	center of mass
NA	numerical aperture
SEM	scanning electron microscopy

ABSTRACT

Bang, Jaehoon Ph.D., Purdue University, May 2020. Feedback Control of Optically Trapped Nanoparticles and its Applications. Major Professor: Tongcang Li.

In the 1970's, Arthur Ashkin developed a remarkable system called the "optical tweezer" which utilizes the radiation pressure of light to manipulate particles. Because of its non-invasive nature and controllability, optical tweezers have been widely adopted in biology, chemistry and physics. In this dissertation, two applications related to optical tweezers will be discussed. The first application is about the demonstration of multiple feedback controlled optical tweezers which let us conduct novel experiments which have not been performed before. For the second application, levitation of a silica nanodumbbell and cooling its motion in five degrees of freedom is executed.

To be more specific, the first chapter of the thesis focuses on an experiment using the feedback controlled optical tweezers in water. A well-known thought experiment called "Feynman's ratchet and pawl" is experimentally demonstrated. Feynman's ratchet is a microscopic heat engine which can rectify the random thermal fluctuation of molecules to harness useful work. After Feynman proposed this system in the 1960's, it has drawn a lot of interest. In this dissertation, we demonstrate a solvable model of Feynman's ratchet using a silica nanoparticle inside a feedback controlled one dimensional optical trap. The idea and techniques to realize two separate thermal reservoirs and to keep them in contact with the ratchet is discussed in detail. Also, both experiment and simulation about the characteristics of our system as a heat engine are fully explored.

In the latter part of the dissertation, trapping silica nanodumbbell in vacuum and cooling its motion in five degrees of freedom is discussed. A levitated nanoparticle in

vacuum is an extraordinary optomechanical system with an exceptionally high mechanical quality factor. Therefore, levitated particles are often utilized as a sensor in various research. Different from a levitated single nanosphere, which is only sensitive to force, a levitated nanodumbbell is sensitive to both force and torque. This is due to the asymmetry of the particle resulting it to have three rotational degrees of freedoms as well as three translational degrees of freedoms. In this dissertation, creating and levitating a silica nanodumbbell will be demonstrated. Active feedback cooling also known as cold damping will be employed to stabilize and cool the two torsional degrees of freedom of the particle along with the three center of mass DOF in vacuum. Additionally, both computational and experimental analysis is conducted on a levitated nanodumbbell which we call rotation-coupled torsional motion. The complex torsional motion can be fully explained with the effects of both thermal nonlinearity and rotational coupling. The new findings and knowledge of a levitated non-spherical particles leads us one step further towards levitated optomechanics with more complex particles.

1. INTRODUCTION

1.1 Optical tweezers

Since its first demonstration by Ashkin [1], optical tweezers has been used in various areas such as biology, physical chemistry and physics. Optical tweezers grant a unique platform that has an ability to trap and manipulate objects ranging from as small as a single atom to as large as micrometer particles by utilizing the optical gradient force (Fig. 1.1) [2].

Biology is one of the representative fields that often employs the technique of optical trapping for novel research. Thanks to the intrinsic force sensitivity [3,4] and maneuverability, investigations such as measuring the binding force between DNA strands [5], force measurement of molecular motors such as single kinesin molecules [6], probing the viscoelastic properties of bio-materials [7] could be achieved. Those bio-materials trapped with optical tweezers were also used to determine the heart of stochastic thermodynamics called fluctuation theorems [8–10].

Not only for biomolecules but also for inorganic materials such as colloidal particles in the hydrological environment has inspired researchers leading to various discoveries and verifications of physical science [11–13]. Recent development of the novel detection scheme accompanied with the optical tweezer allowed researchers to quantify the instantaneous Brownian velocity of a colloidal particle in both air and liquid environments [14,15].

Besides the particles trapped in a liquid environment where the momentum relaxation time is too short because of large friction, optically levitated particles in air or vacuum [16] opens up new possibilities to use the levitated particles as a platform for studying complex phenomena in physics [17–19].

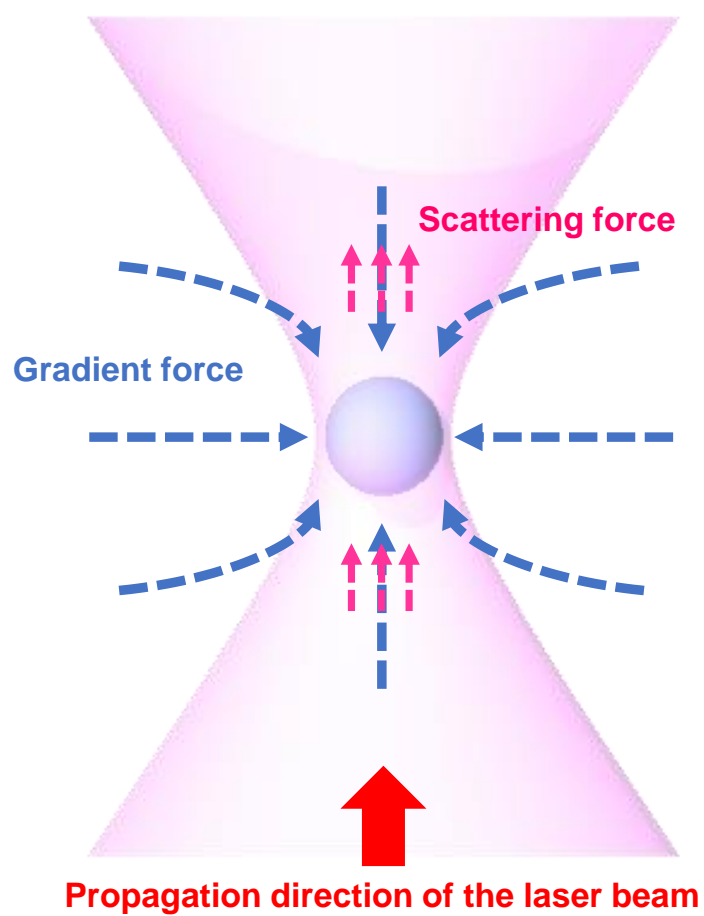


Fig. 1.1. Brief schematic of an optical tweezer.

1.2 Generation of complex optical tweezers and its applications

On top of the advantages and applications of optical tweezers explained in section 1.1, substantial effort has been put in by various research groups to modify the trap site of the optical tweezer for the demonstration of even more innovative experiments [20, 21]. Even though the naming or application differs from each other, the underlying principle of the technique is relatively simple. The incident trapping beam is modulated using either spatial light modulators (SLM) [22], acousto-optic modulators (AOM) [23] or moving mirrors driven by galvano motors [13]. The modified complex wavefront is transferred to the focus of the objective lens using a telescope configuration to create the desired optical trap at the trapping site (Fig. 1.2).

More than 400 optical traps at the same trapping site inside a water chamber has been successfully demonstrated [22]. Not only that, demonstration of selective rearrangement after trapping multiple atoms will allow researchers to mimic the nature of condensed matter and the effect of defects [24, 25]. Even though the trapping of multiple particles in the size of nano or micro-meter in vacuum environment is still challenging because of the high laser power requirement, progress has been gradually made [26, 27].

One of the most important achievements using this complex optical tweezer is the production of higher order modes of the laser wave front like the Laguerre Gaussian (LG) mode [28]. Different from ordinary Gaussian beam optical traps, photons in the LG mode experience additional momentum which is the orbital angular momentum. Researchers successfully observed the interaction of this angular momentum between the photons and matter using these complex optical tweezers [20]. Successful access to the angular momentum of photons will benefit the data transfer for quantum information using photons [29].

Yet another important contribution of the complex optical tweezer is the investigation of diffusion for colloidal particles in 1D or 2D. By generating a scanning optical tweezer or partially overlapping multiple optical tweezers, one can confine a particle

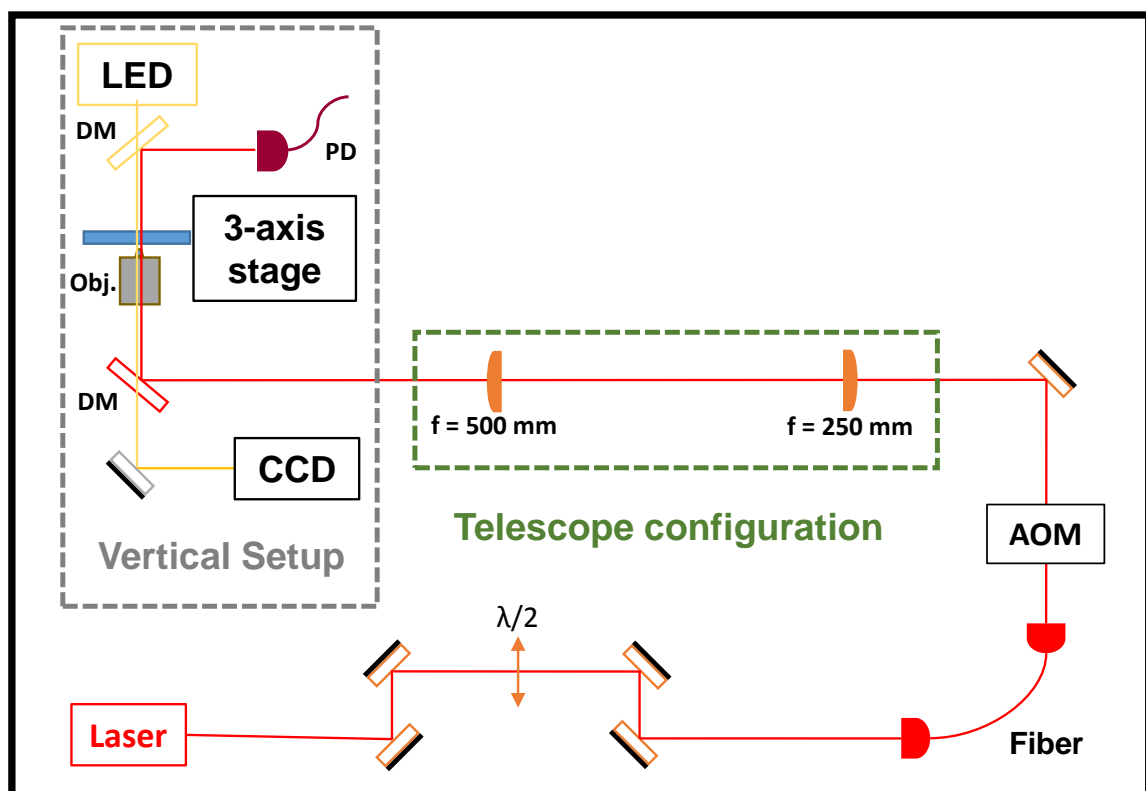


Fig. 1.2. Typical optics configuration to create complex optical tweezers. $\lambda/2$: half-wave plate, DM: dichroic mirror, Obj.: objective lens, PD: photo diode.

inside a finite dimension trap which allows the particle to diffuse only in certain directions. Using this approach, researchers were able to study the unique behavior of single file diffusion [30] as well as the effect of optical ratchets which resembles the behavior of molecular motors [23, 31].

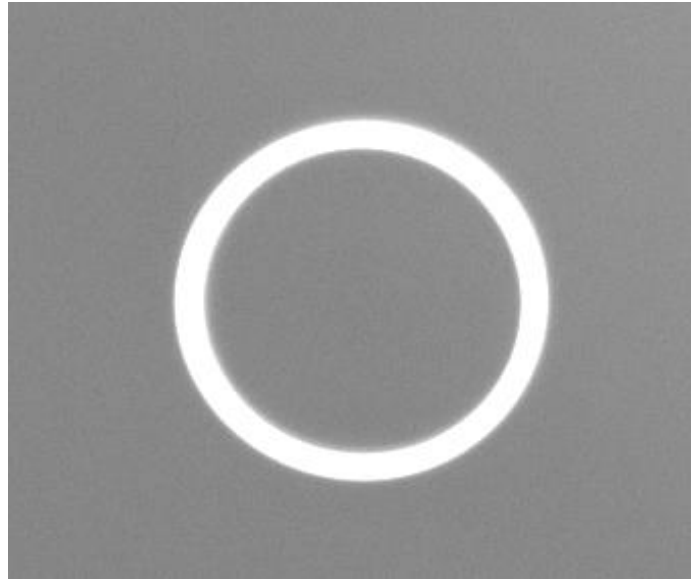
1.3 Levitated optomechanics using optical tweezers

Optomechanics is a field that couples optical and mechanical DOFs by utilizing the momentum transfer of photons [32, 33]. Feedback cooling [34, 35] or amplifying of integrated cavity mirrors as well as side band cooling [36–38] of microstructures has been successfully demonstrated by employing the radiation pressure of lasers. Levitated optomechanics, where the test mass is “levitated” in space, went through a similar trend. The motion of the levitated particle was cooled down using feedback cooling [39–41] or cavity cooling [42–47]. Due to the well isolated nature and robustness, optically levitated particles demonstrated various kinds of precision measurements including force [4], acceleration [48], torque [49] and temperature [50].

Besides the well-known harmonic oscillation, levitated particles have exceptional intrinsic advantage compared to a clamped oscillator, where the test mass can rotate freely. Full rotation of silicon nanorods [51, 52] along with gigahertz rotation of asymmetric silica particles [49, 53, 54] successfully exhibited the potential of levitated optomechanics as a new candidate for novel experiments [55].

1.4 Contents of this dissertation

In the following chapters, trapping and manipulation of silica particles in both water and vacuum environment using optical tweezers will be demonstrated. Chapter 2 will discuss about the realization of a thought experiment called “Feynman’s Ratchet and Pawl.” Description about Feynman’s ratchet and the technical difficulties of realizing the experiment is provided. Also, the methods to overcome the difficulties by utilizing a computer controlled multiple optical tweezer will be discussed in details.

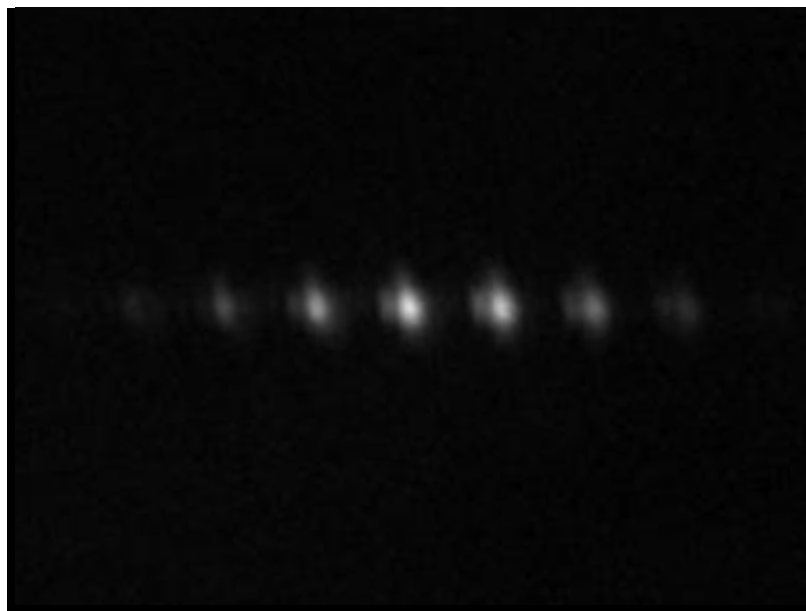


(a) Reflected image of an optical ring trap generated with a galvo-mirror.

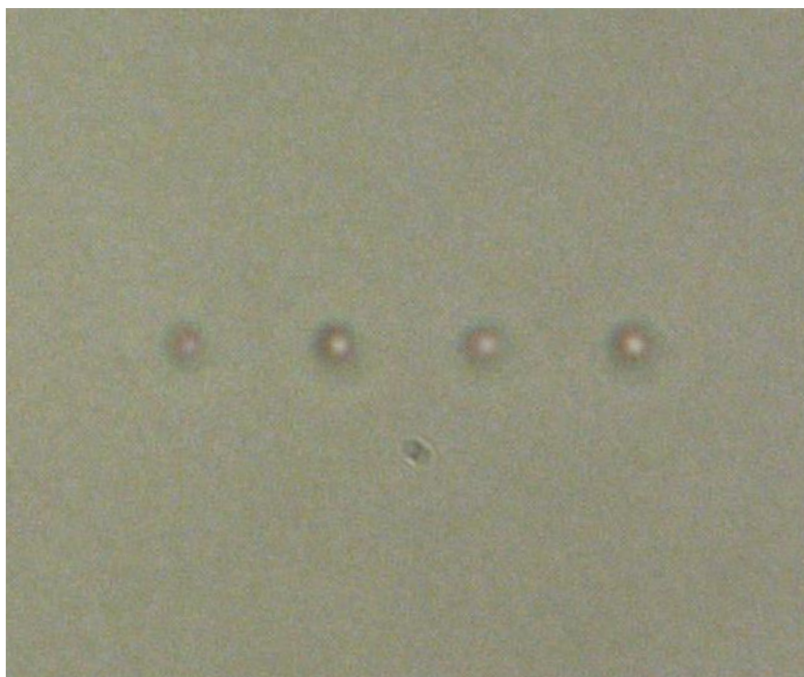


(b) Multiple silica microspheres (with diameter of $1.5 \mu m$) trapped inside a ring trap. The distortion is because of alignment imperfection of the imaging system.

Fig. 1.3. Example of a ring trap generated using a 2-axis galvo-mirror.



(a) Reflected image of multiple optical tweezers generated using an AOD



(b) Optically trapped nanodiamond clusters using multiple optical tweezers. The size of a single diamond is roughly 100 nm .

Fig. 1.4. Example of multiple optical tweezers generated using acousto-optic deflector (AOD).

In chapter 3, a levitated optomechanical system to trap a silica nanodumbbell will be introduced. The experimental details about the system as well as a brief theory about the torsional motion of a levitated nanodumbbell is provided. Chapter 4 will cover the five dimensional cooling of a levitated nanodumbbell in vacuum. The translational and torsional motions of a levitated nanodumbbell is cooled down to a few kelvin. In chapter 5, the nonlinearity of a levitated nanodumbbell is explored. The unusual behavior of the levitated nanodumbbell is analyzed in both theory and experiment. Finally, in chapter 6, possible future directions are proposed. Especially, a preliminary discussion of a levitated trimer particle is given. The triangle trimer could be a good prototype exploring a possibility of a new geometry of a levitated particle such as an elliptical disk.

2. EXPERIMENTAL REALIZATION OF FEYNMAN'S RATCHET

2.1 Motivation

2.1.1 Feynman's ratchet and pawl

Feynman's ratchet and pawl is one of the representative conceptual systems exploring the possibility of harnessing useful work from random fluctuations [56]. The system consists of two critical components which are the ratchet and the vane. Each component is immersed in its own heat reservoir and is connected with an axle. The ratchet is regulated by a pawl so that the random perturbation generated by the collision of gas molecules on the vane side could be rectified to a unidirectional rotation. As an effort to better understand stochastic thermodynamics, several theoretical research projects have been conducted using this beautiful system using random fluctuation [57–65]. Furthermore, the intrinsic characteristic of the system, which is the asymmetry with the combination of Brownian motion, became a suitable platform to study the behavior of molecular motors [66–69].

2.1.2 Experimental efforts to realize Feynman's ratchet

However, due to the difficulty of realizing two separate thermal baths and keeping the two heat baths simultaneously in contact with the system, construction of a ratchet associated with two thermal baths has not been realized. In this chapter, realizing "Feynman's ratchet and pawl" employing a feedback controlled multiple optical tweezers will be discussed in detail. The demonstrated Feynman's ratchet captures all the essential features that makes this work unique from others.

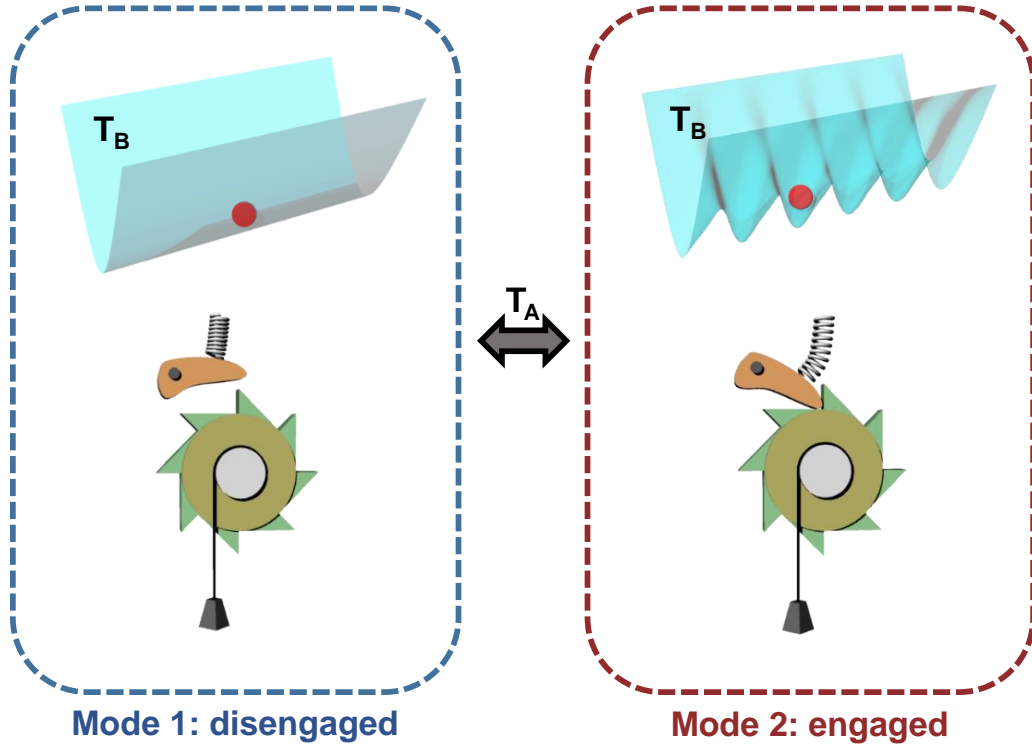


Fig. 2.1. Two modes (disengaged mode and engaged mode) of ratchet and pawl corresponding to each model (top: Jarzynski's model, bottom: Feynman's model). T_A : temperature generated using computer feedback control, T_B : temperature of the environment.

2.2 Realization of Feynman's ratchet and pawl

2.2.1 Periodic lattice model of Feynman's ratchet

C. Jarzynski and O. Mazonka [62] proposed a solvable model of the Feynman's ratchet by assuming a freely diffusing particle inside a periodic lattice potential. As shown in Fig. 2.1, the periodic potential has two different modes which are the uniform potential mode and the sawtooth potential mode. The uniform potential mode corresponds to the situation when the pawl is disengaged from the mechanical ratchet and the sawtooth potential mode corresponds to the situation when the pawl is

attached to the ratchet. Consequently, the switching between the two potential modes expresses the Brownian motion of the pawl which is determined by the temperature of the heat reservoir A (T_A). The random collision of the gas molecules on the vane side (heat bath B, T_B) can be thought as the particle's diffusive Brownian motion inside the periodic potential. The overall motion of the particle inside the optical periodic lattice can be expressed as a coupled motion of particle diffusion inside the lattice and switching of the two potential modes. The evolution of the probability distribution of the Brownian particle inside a specific 1D potential can be described by the reaction-diffusion equation [70]:

$$\frac{\partial P_i(x, t)}{\partial t} = \frac{\partial}{\partial x} \left[\frac{U'_i(x)}{\gamma} P_i(x, t) \right] + D \frac{\partial^2 P_i(x, t)}{\partial x^2} + k_{ji} P_j(x, t) - k_{ij} P_i(x, t) \quad (2.1)$$

where $P_i(x, t)$ is the probability density of the particle at position x at time t in potential mode i ($i = 1, 2$), $U_i(x)$ the potential energy at position x in mode i , γ the Stokes friction coefficient, $D = \frac{k_B T_B}{\gamma}$ the diffusion constant, and k_{ij} (k_{ji}) the switching rate from potential i (j) to j (i) ($i \neq j$). Here we assume overdamped condition and ignore the inertia of the particle. According to the Metropolis algorithm [71], k_{ij} is:

$$k_{ij} = \Gamma \min \left[1, \exp \left(- \frac{U_j(x) - U_i(x)}{k_B T_A} \right) \right] \quad (2.2)$$

where Γ is a constant. (The Γ used in this chapter is not related with the damping rate introduced in next chapters.) Later in this chapter, this equation is used to create a virtual heat bath on the system using computer feedback control for an optimized value of Γ .

2.2.2 Generation of a periodic optical lattice

In order to generate a fully controllable periodic potential, an acousto-optic deflector (AOD, DTD-274HA6, IntraAction Corp.) was used in combination with the telescope system to generate multiple optical tweezers at the trapping region (Fig. 2.2). Nineteen optical tweezers were created with a desired uniform spacing to realize an

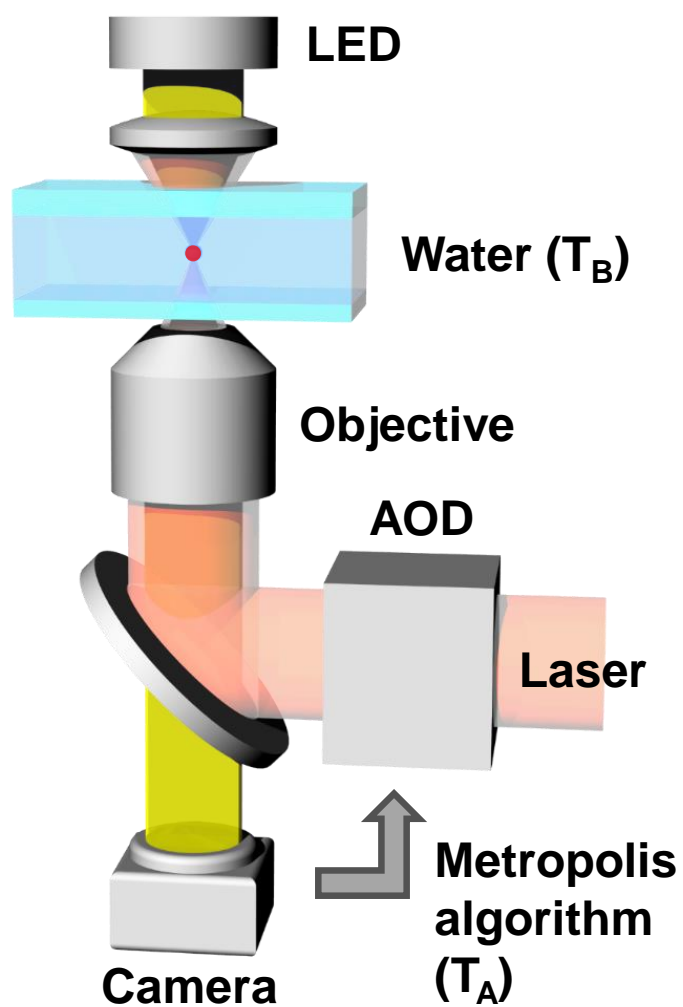


Fig. 2.2. Setup of the experiment. A silica nanosphere (with a diameter of 780 nm) emerged in water was used for the experiment.

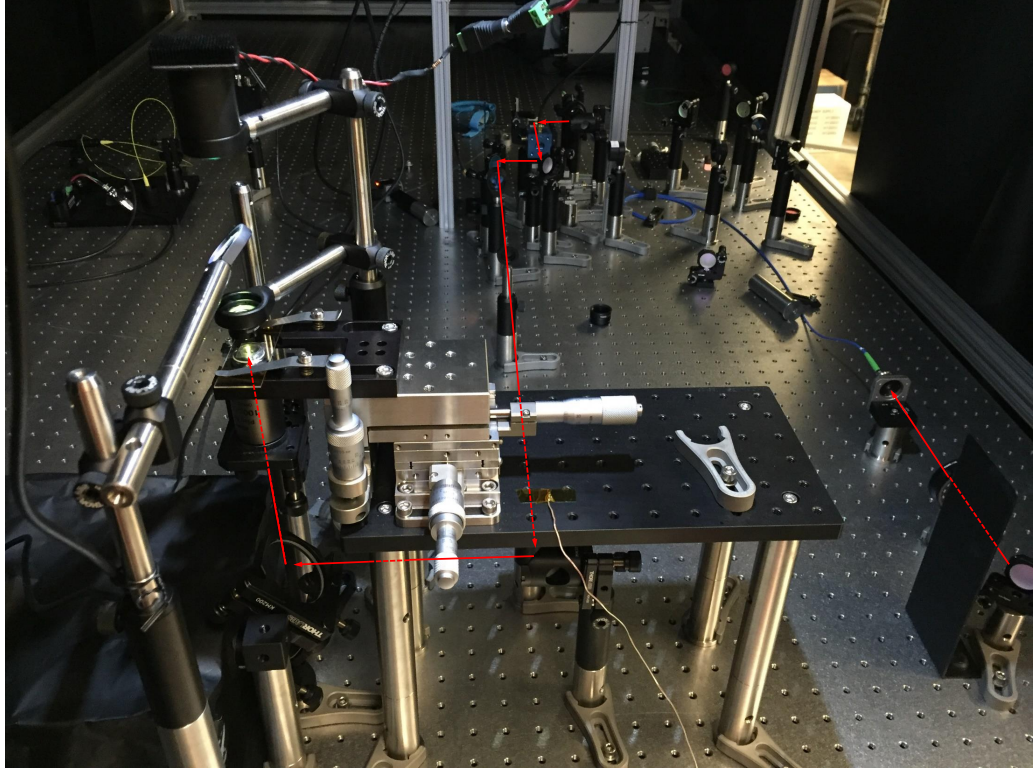


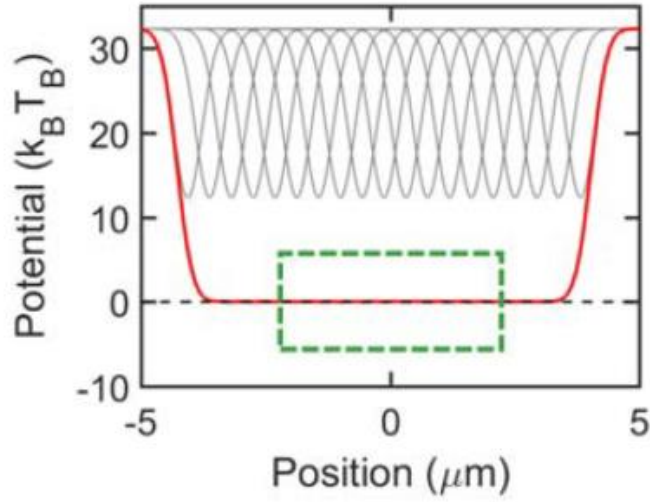
Fig. 2.3. Picture of the optics setup. The red lines indicate the path of the trapping laser.

optical lattice that either has a smooth potential or a sawtooth potential with three teeth along the effective trapping area.

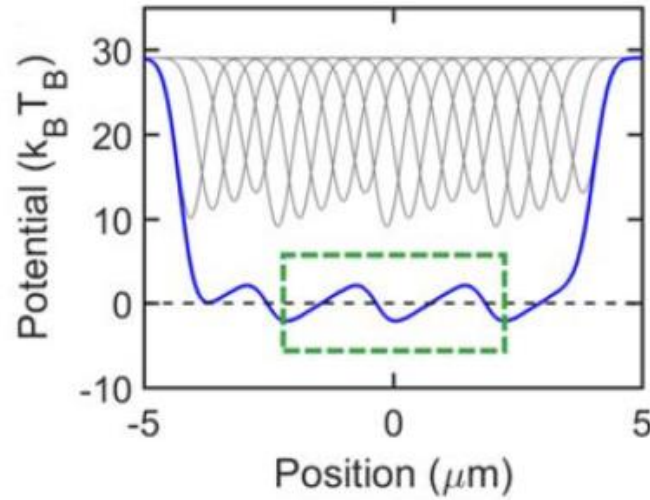
To control the power and spacing of each individual optical tweezer, customized wave functions were generated using an arbitrary function generator (33500B, Keysight Technologies). The wave function fed to the AOD is:

$$f = \sum_{i=1}^n c_i \sin(\omega_i t + \phi_i) \quad (2.3)$$

where c_i is used to control the power of each individual optical tweezer, ω_i to control the spacing, ϕ_i to keep the total power of the radio frequency (RF) signal below to the input capacity of the amplifier without losing too much power for each individual tweezer.



(a) Methods of generating a flat potential (red) using 19 optical tweezers are shown. Note that all tweezers have same power (grey dash).



(b) Generating of a sawtooth potential (blue) using 19 optical tweezers. The power of each individual tweezer is adjusted to effectively express the sawtooth feature.

Fig. 2.4. Schematics of generating 1D potential trap. Thin grey curves indicate each optical tweezer approximated in Gaussian. Green dashed boxes specify the region used in the experiment.

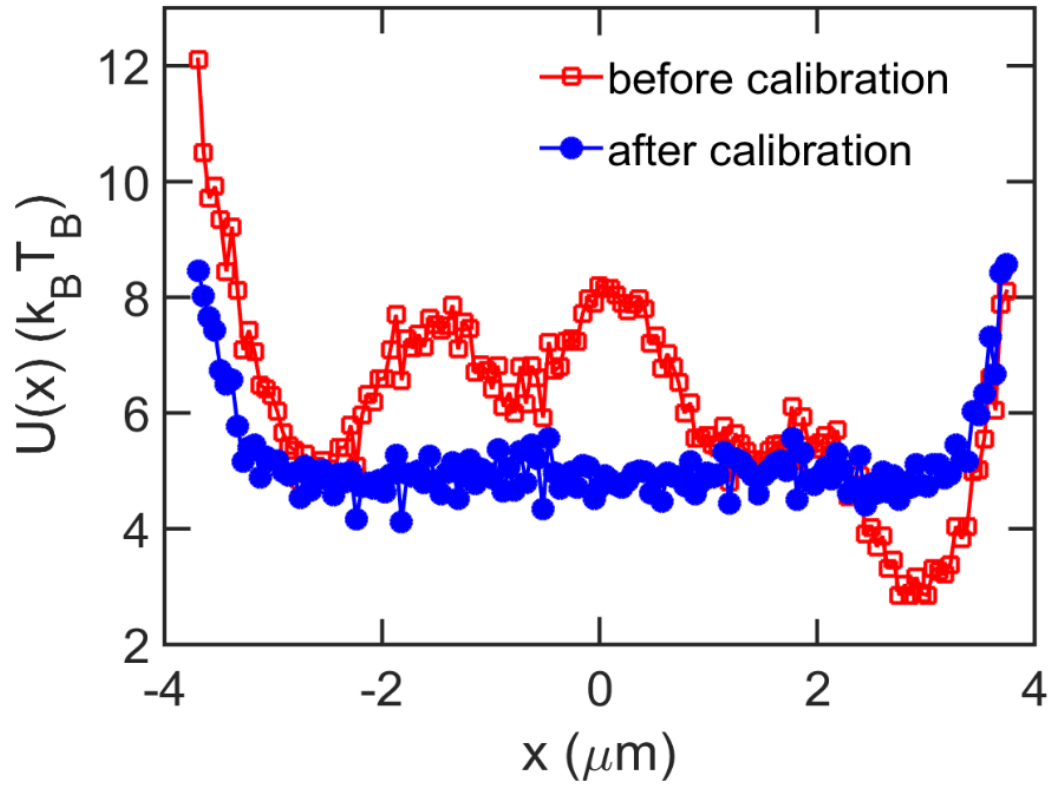


Fig. 2.5. Calibration of a 1D potential trap. Example of a uniform flat potential before calibration (blue circles) and after calibration (red squares).

Using a one dimensional (1D) optical trap, silica nanoparticle with a diameter of 780 *nm* emerged in a water chamber was trapped and used for the experiment. Because of the gradient force formed by the optical trap, the silica particle can only diffuse in 1D along the trap and is confined for the other dimensions. The position of the water chamber was adjusted using an high-precision XYZ stage (562-XYZ, Newport) so that the optical trap could lie around 10 μm higher than the bottom of the water chamber. This gap allows one to neglect the effect of surface while minimizing the distortion of laser wavefront caused by the interface between different media. In order to observe the effect of the thermal fluctuation, precise adjustment on each optical tweezers was required. Thus, precise measurement of the relative potential energy was preceded for each optical trap. To determine the relative potential of each optical lattice, free Brownian motion of the particle was observed every 5 *ms* with a CMOS camera for the corresponding potential mode. The relative potential energy can be calculated from the equation [23]:

$$U(x) = -k_B T_B \ln \frac{N(x)}{N_{total}} \quad (2.4)$$

where k_B is the Boltzman constant, T_B the temperature of the chamber, $N(x)$ the bin number at position x and N_{total} the total number of position data. More than 500,000 data points were used for every measurement and after several trial and error based on the measured results, the desired level of precision could be achieved. In the end, the standard deviation of the uniform potential for the detached mode used in the real experiment was $0.15 k_B T_B$ which is small enough to neglect its influence to the particle motion. The sawtooth potential was created similarly to achieve the desired shape for the experiment (Fig. 2.6). The height of the sawtooth (depth from bottom to peak) was designed to be $4.8 k_B T_B$ and the asymmetry ratio was 3:1. Both the depth and ratio of asymmetry are important factors influencing the evolution of probability distribution. Here, the factors are chosen so that the effect of different temperature conditions could be observed with in a reasonable time period without losing the stability of the system.

2.2.3 Experimental realization of Feynman's ratchet with feedback control

As already discussed in previous sections, two individual thermal baths have to be in contact with the system. In this system, one heat bath is the water chamber where the temperature is $T_B = 296K$. The other heat bath, where the ratchet and pawl is emerged in Feynman's original thought experiment, is artificially generated using a computer controlled feedback loop. Similar to the potential calibration, the position of the silica particle was recorded every 5 milliseconds (ms). Additionally, every 200 ms , the computer program (coded using Labview) randomly switched the potential trap between the two modes based on the probability determined by the position of the particle and chosen temperature (T_A). This process acts as a virtual second heat bath connected to the system. The switching probability is calculated from the Metropolis algorithm [62,71]:

$$P_{switch} = \min[1, \exp \frac{-\Delta E}{k_B T_A}] \quad (2.5)$$

where k_B is the Boltzmann constant and T_A is the temperature set for the virtual heat bath. $\Delta E = U_2(x) - U_1(x)$ when switching from potential mode 1 (disengaged mode) to mode 2 (engaged mode) and $\Delta E = U_1(x) - U_2(x)$ for the opposite case.

In Feynman's original thought experiment, the ratchet and vane are rotating which means that the 1D trap has to be infinitely long for both directions to fully capture the nature of the rotating ratchet. However, as shown in Fig. 2.6, only 3 periods of the sawtooth could be realized due to experimental limitations (such as limited laser power and input power limit of the AOD driver). Therefore, to overcome the finite length of the trap and fully resemble the rotating ratchet, we use a computer program and modify the experimental procedure. The full experimental process is as follows:

1. Particle was trapped using a single optical tweezer and placed at the center of the effective trapping region ($x = 0$).
2. The trap was changed to 1D trap in mode 2 to start the experiment.

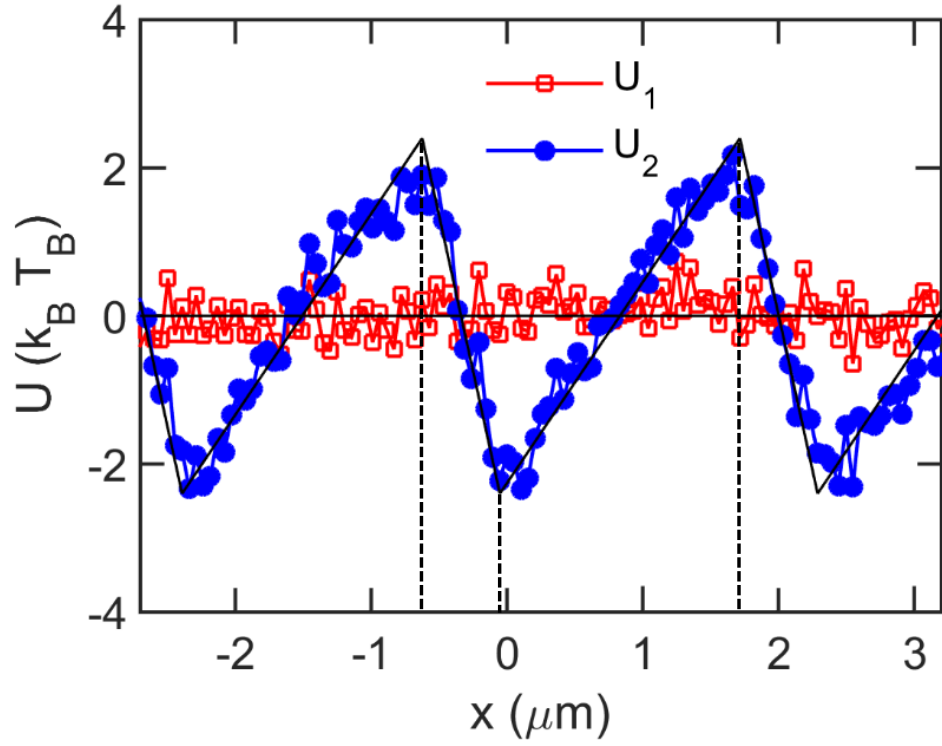


Fig. 2.6. Profile of potential energy for mode 1 (disengaged mode, red hollow squares) and mode 2 (engaged mode, blue filled circles). The black lines are used for simulation and are determined by fitting the measured potential. The corresponding temperature is 296 K. The asymmetry of the sawtooth potential is about 1:3.

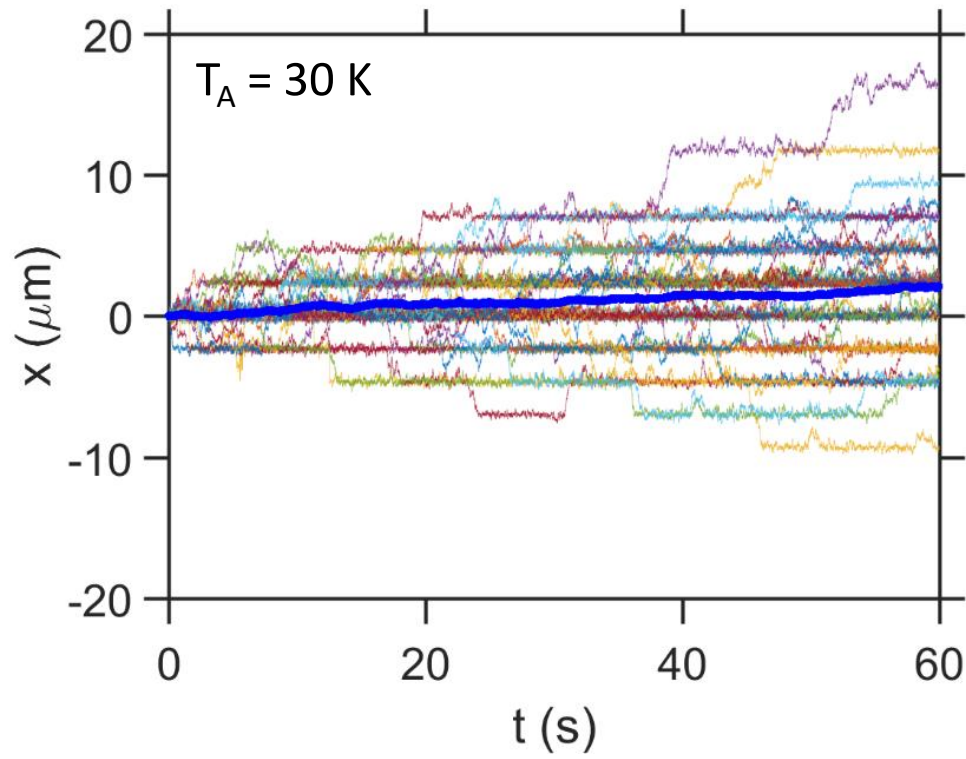


Fig. 2.7. 50 trajectories (back ground) and the average (thick blue) of the particle when the virtual heat bath (T_A) is 30 K . The average displacement at 60 sec is $\langle \Delta x \rangle = 2.1 \pm 0.6 \mu\text{m}$.

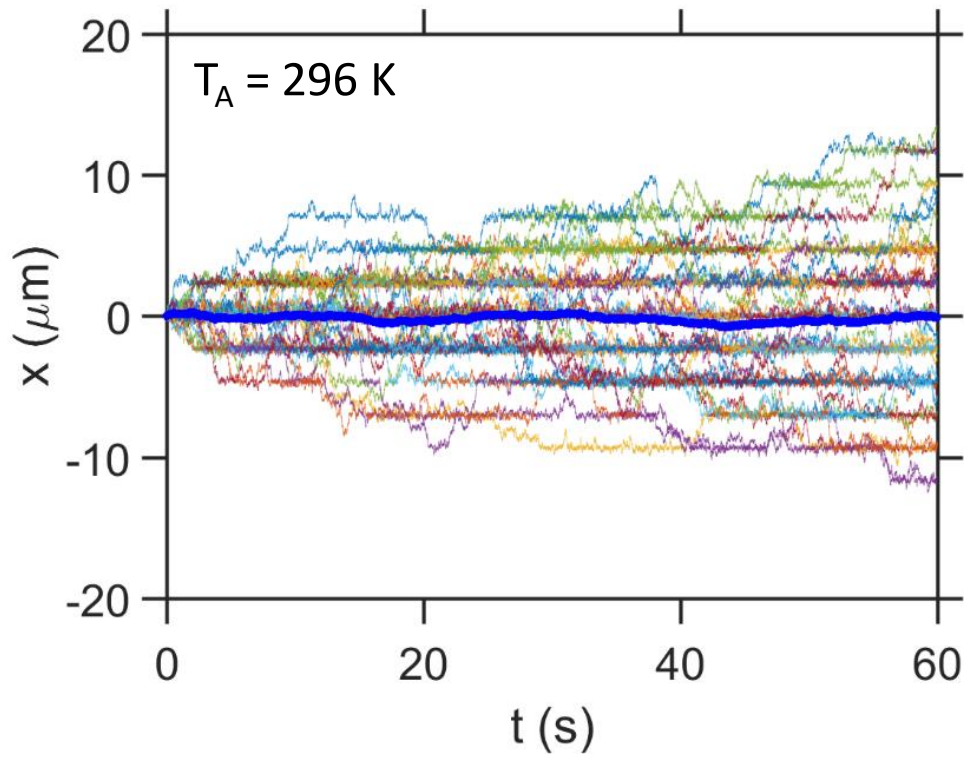


Fig. 2.8. 50 trajectories (back ground) and the average (thick blue) of the particle when the virtual heat bath (T_A) is 296 K . The displacement is $\langle \Delta x \rangle = -0.1 \pm 0.9 \mu\text{m}$.

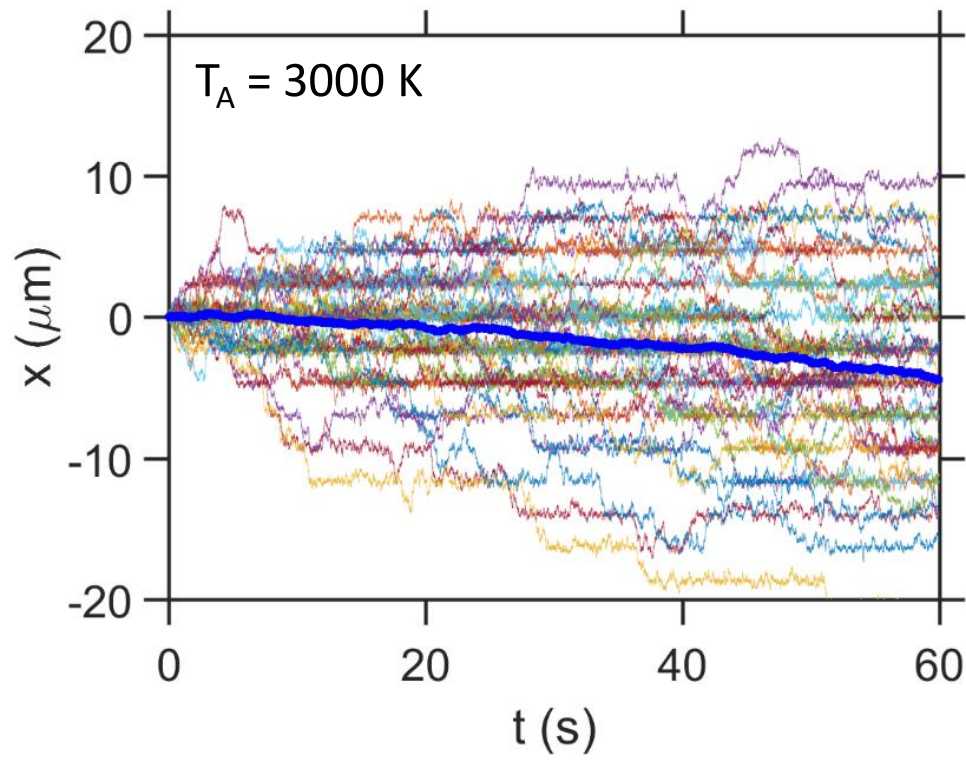


Fig. 2.9. 50 trajectories (back ground) and the average (thick blue) of the particle when (T_A) is 3000 K . The displacement is $\langle \Delta x \rangle = -4.5 \pm 0.9 \mu\text{m}$.

3. As the particle diffuses inside the trap, the displacement of the particle was observed for every 5 ms.
4. Every 200 ms, the trap switched randomly based on the possibility calculated at the position of the particle at the moment.
5. If the particle arrives to one of the position where the two minima on both ends are (no matter of the current potential mode), the particle was drawn back to the center. The drawing back motion was not recorded.
6. The experiment was restarted while maintaining the same condition as before.

Fig. 2.7, 2.8 and 2.9 shows the result of 50 particle trajectories (thin lines on background) and its average trajectory (thick blue line) for $T_A = 30K$ (Fig. 2.7), $T_A = 296K$ (Fig. 2.8) and $T_A = 3000K$ (Fig. 2.9). Each trajectory was recorded for 60 seconds. As clearly shown in Fig. 2.8, the average displacement remains near $0 \mu m$. This results agrees well with Feynman's prediction [56] that the ratchet will not turn when the two thermal bath have the same temperature even though the sawtooth potential is asymmetric. The more interesting part is shown in Fig. 2.9. If $T_A > T_B$, the ratchet rotates in the forbidden direction which is also emphasized in Feynman's lecture [56].

2.2.4 Feynman's ratchet as a microscopic heat engine

Since the system consists of two thermal baths, it can be understood as a micro-sized heat engine. To determine the characteristic of the system as a heat engine, an additional potential slope was added to the 1D optical trap. The slope effectively works as an external load so that the capability of the system as a heat engine could be revealed. Fig. 2.10 presents the average velocity of the particle for different temperatures. The blue rectangular points are the case when a positive effective load is added to the system. In real experiment, $-0.05 k_B T_B / \mu m$ of extra potential energy was added to the original potential trap. The red circle represents the situation of no

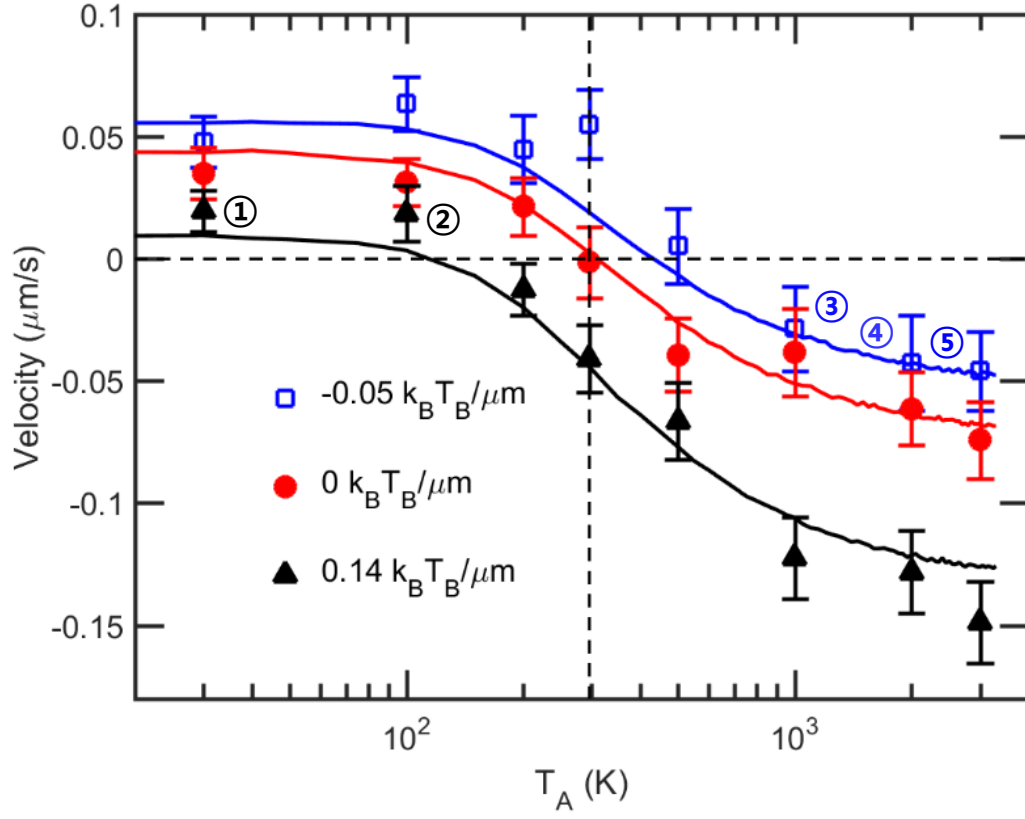


Fig. 2.10. Velocity of the particle for different external loads. Each data point corresponds to an average of 50 trajectories. Blue squares show the result with a positive load ($-0.05 k_B T_B / \mu\text{m}$ slope), red circles without any load and black triangles with a negative load ($-0.14 k_B T_B / \mu\text{m}$ slope). Solid lines are simulation results.

external load. At last, the black triangles show the average velocity when a negative external load is added ($0.14 k_B T_B / \mu m$ was added to the trap.) Here, each point corresponds to fifty 60-s trajectories and the solid lines are the simulated result of our system. The simulation was designed to exactly follow the experimental procedure so that it could reflect the real situation. The work done by the system is:

$$\langle W \rangle = f \langle \Delta x \rangle \quad (2.6)$$

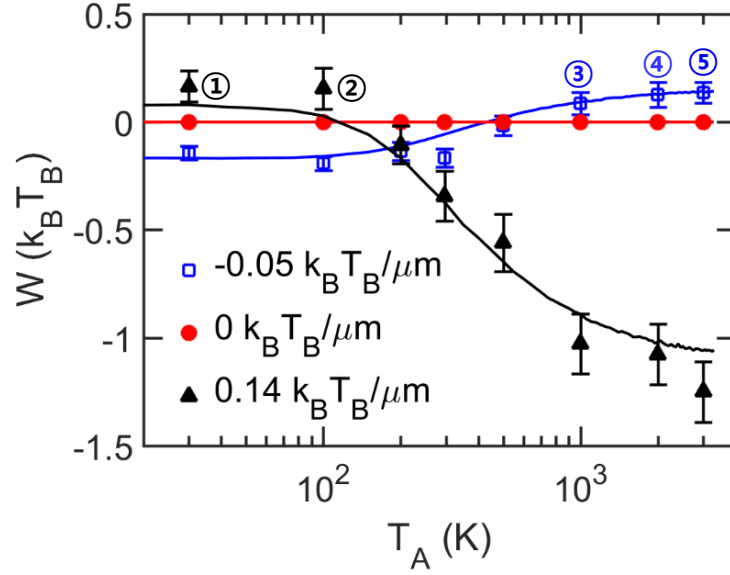
where f is the slope of the system and Δx is the particle's displacement.

As numbered in Fig. 2.10 and Fig. 2.11, positive work is done when the velocity of the particle is positive under positive slope (① and ②) and negative under negative slope (③, ④ and ⑤). From theoretical predictions, six data points were supposed to do positive work (Fig. 2.11(b)) but since two points of the experimental conditions are lying too close to the edge of the heat engine regime (shaded in cyan), we could only observe five points that are performing positive work. The largest amount of work extracted was $0.16 k_B T_B$ in 60 seconds (⑤).

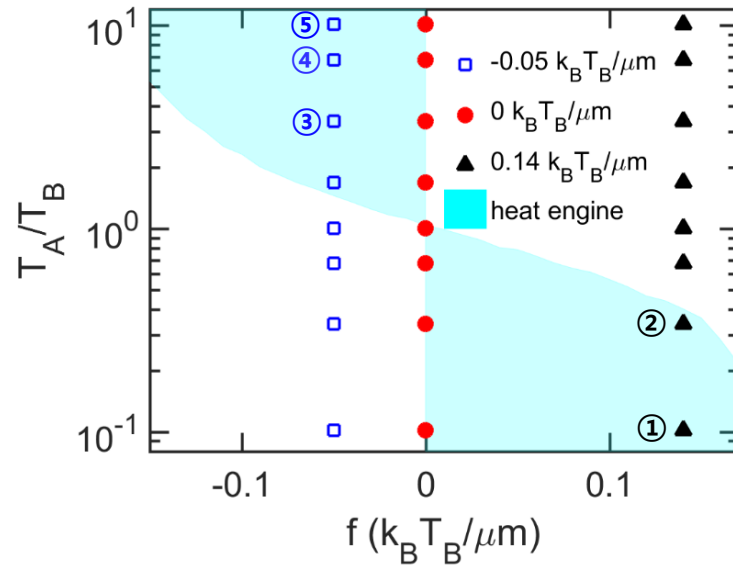
Fig. 2.12(a) shows the heat dissipation from the two thermal reservoir in the presence of negative slope (positive external load). The heat dissipation of reservoir A (Q_A) is defined as a sum of the potential energy change of the particle due to the switching of the two potential modes. On the other hand, heat dissipation for the reservoir B (Q_B) is the sum of the potential energy change of the particle caused by the diffusion while the potential mode is unchanged. Since we have already determined the work and heat for the system, the net entropy production can also be calculated from the equation:

$$dS = -\frac{\langle Q_A \rangle}{T_A} - \frac{\langle Q_B \rangle}{T_B}. \quad (2.7)$$

At thermal equilibrium ($T_A = T_B$), entropy is not produced because the net heat flux is zero (Fig. 2.12(b)). As already indicated in “Figure 2.12(b)”, the average entropy production does not vary too much for different external loads. This is because in Feynman's ratchet, the energy of the high temperature bath mainly dissipates through heat. This is also related to the low efficiency of Feynman's ratchet, since

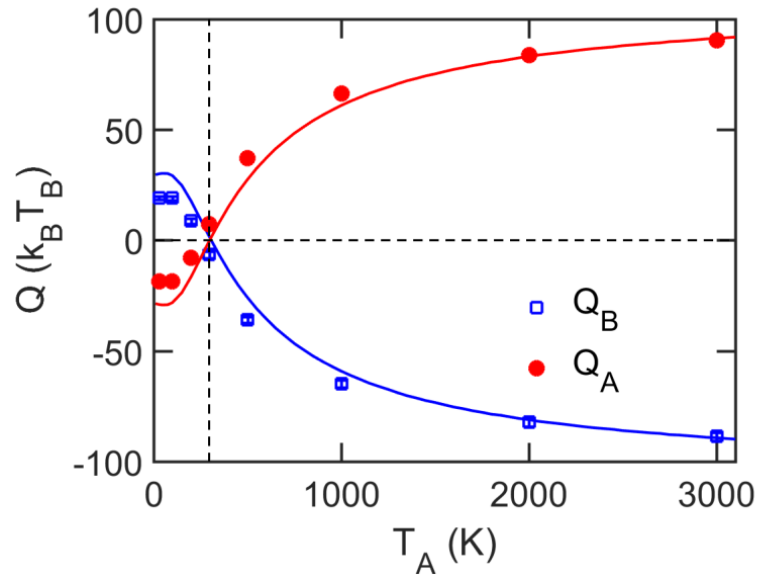


(a) Work done by the system under different loads. The slope of blue squares, red circles and black triangles correspond to $-0.05 k_B T_B / \mu m$, $0 k_B T_B / \mu m$ and $0.14 k_B T_B / \mu m$ respectively.

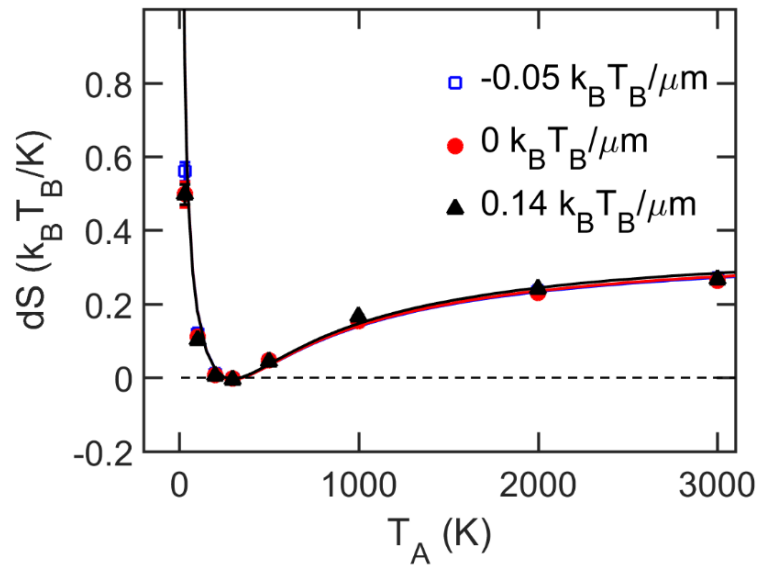


(b) The parameter map for our system with the respective points.

Fig. 2.11. Work demonstration using the optical ratchet.



(a) Calculated heat for different temperatures in the case of negative slope ($-0.05k_B T_B/\mu m$).



(b) Averaged total entropy production of the system as a function of temperature.

Fig. 2.12. Heat and entropy production of the optical ratchet.

only a small portion of energy in the higher temperature bath can be converted to work. The efficiency of an engine can be calculated as:

$$\eta = \frac{\langle W \rangle}{\langle Q_{high} \rangle} \quad (2.8)$$

where Q_{high} is the heat flux from the higher temperature bath. Indeed the efficiency of our ratchet was calculated to be low ($\eta = 0.0015$) as predicted in other theoretical analyses [58,61]. Although Feynman himself believed that the ratchet and pawl can achieve the same efficiency as a Carnot engine [56], the two system operate under a fundamentally different condition. A Carnot engine is a theoretical model that follows a process called the “Carnot cycle”. The Carnot cycle includes two isothermal and two adiabatic processes which are assumed to be reversible. This means each process should be in equilibrium or near equilibrium state. However, Feynman’s ratchet relies on the thermal fluctuation which operates under non equilibrium state. In other words, since the two thermal baths with different temperatures are always in contact with the system, Feynman’s ratchet never achieves the thermal equilibrium states.

2.3 Conclusion

In this chapter, demonstration of Feynman’s ratchet and pawl with a SiO_2 nanosphere and a modified 1D optical trap was introduced. The realization of two individu with baths that continuously and simultaneously influence the system is the key breakthrough of this work. The water chamber was the first thermal reservoir which regulates the diffusive Brownian motion of particle in this experiment. The second thermal bath was virtually generated using a computer feedback control. Consequently, the effect of different temperatures and the characteristics of our system as a heat engine could be studied in depth. Using this system in advance, research related to thermodynamics and information processing [72–75] can be studied since the effect of the temperature difference of two thermal baths on the particle motion is already observed in this experiment. If the switching mechanism is properly modified, it is

also possible to mimic and study the motion of a molecular motor which will lead to a better understanding of its motion and efficiency [66, 68, 69, 76, 77].

3. LEVITATION OF NANODUMBELL AND OBSERVATION OF TORSIONAL MOTION

3.1 Motivation

There has been extensive studies done with spherical particles in levitated optomechanics [4, 14, 44, 78–83] and they are successfully breaking ground in the field of precision measurement. On the other hand, there are also growing interest in levitated nonspherical particles which have additional degrees of freedom for control [49, 52, 53, 84–89]. Levitated nonspherical particles like nanorods and nanodumbbells have been proposed to be a suitable candidate for detecting the Casimir torque [90], studying many-body phase transitions [91] and creating rotational matter-wave interferometers [92]. Moreover, levitated microdisks [93] have been proposed for gravitational wave detection [94].

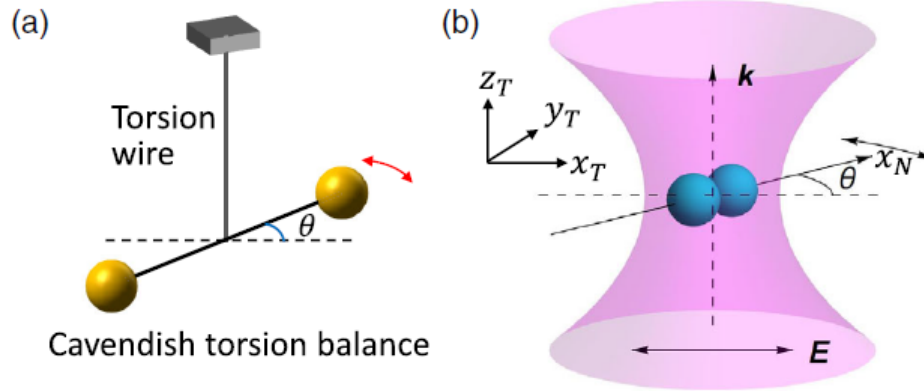


Fig. 3.1. Optically levitated nanodumbbell (b) as an analogous system of Cavendish torsion balance (a). The restoring force of a levitated nanodumbbell is provided from the linearly polarized optical tweezer whereas the classical Cavendish torsion balance uses a torsion wire [53].

An optically levitated nanodumbbell for example is a novel analogy of a Cavendish torsion balance which was used to measure the gravitational force and the Coulomb force (Fig. 3.1). A torsion balance consists of a dumbbell and a torsion wire which is holding the dumbbell. Thus the dumbbell is able to rotate when external torque is applied until the restoring torque exerted from the torsion wire balances the external torque out. Compared to the torsion balance, the restoring force of an optically levitated nanodumbbell results from the optical tweezer itself, where the linearly polarized laser provides different potential energy depending on the relative angle of the trapped nanodumbbell. Because of the small mass of a nanodumbbell, the torque sensitivity of a levitated nanodumbbell is expected to be as high as $10^{-28} Nm/\sqrt{Hz}$ in high vacuum [53,90]. Therefore the system is a good candidate to measure extremely small torques like Casimir torque in vacuum environment.

All of the proposed particles have similar characteristics when trapped with an optical tweezer. Top like particles are invariant with respect to rotations around their symmetry axis and are thus free to rotate around that symmetric axes inside the optical trap. Consequently, many applications mentioned above require consideration of their motional degree of freedom in all five dimensions which couple to the trapping light. In this chapter, we establish a levitated optomechanical system suitable for trapping silica nanodumbbells. Silica nanodumbbells are so far the only defined non-spherical nanoparticles that survive under high vacuum environment [49, 53]. Details about the optical setup as well as the essential characteristic of a levitated nanodumbbell will be discussed extensively.

3.2 Experimental Setup

Fig. 3.2 is the schematic of our setup. A 1064 *nm* laser (Mephisto, Coherent, Inc.) is used for trapping. The maximum power of the laser is about 2W and the power of the trapping beam at the focus is estimated to be about 200 *mW*. The trapping laser is first guided through a polarization maintaining fiber (P3-1064PM-

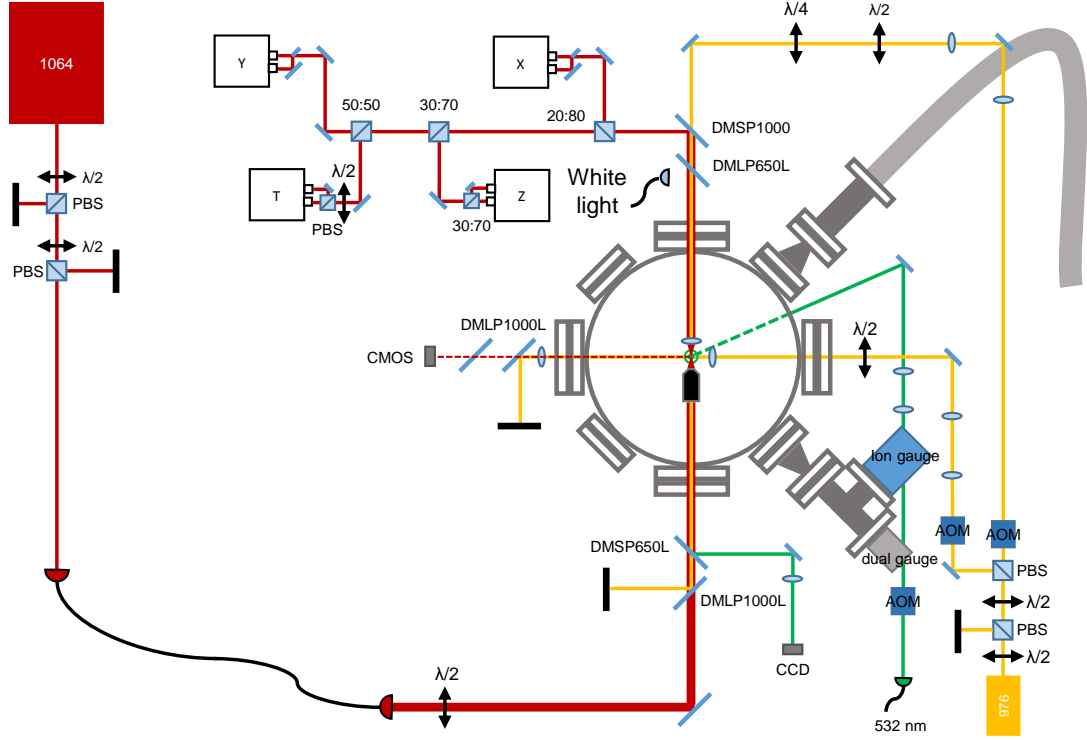
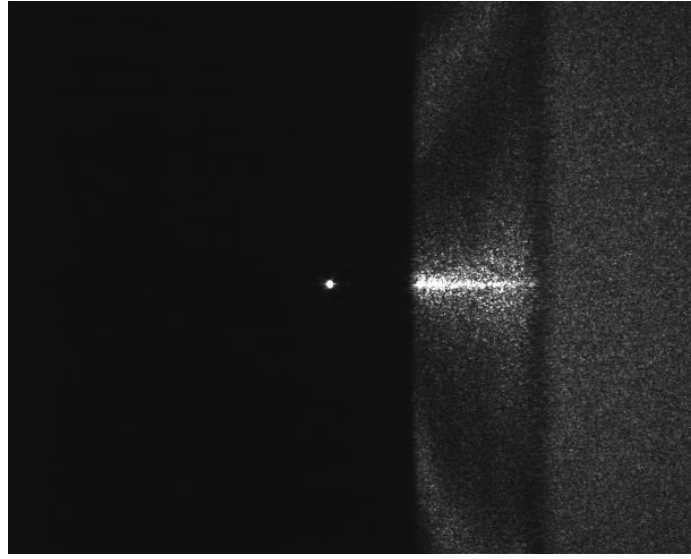


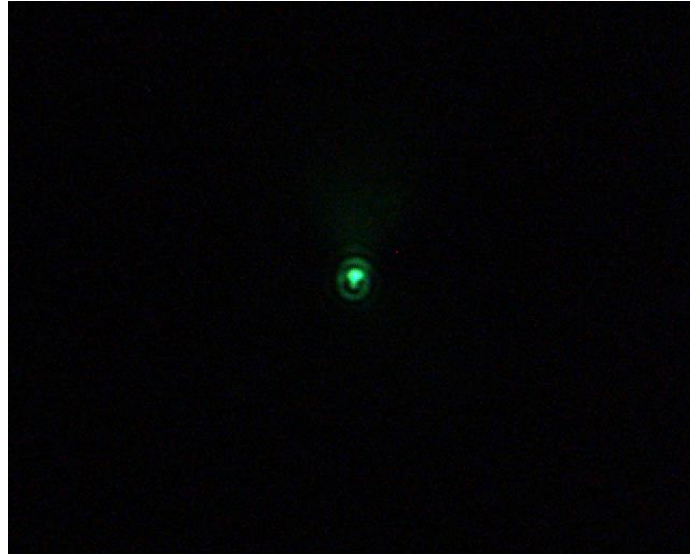
Fig. 3.2. Overall feature of the setup. A 1064 nm laser (Mephisto, Coherent, Inc.) is used for trapping. A $\frac{\lambda}{2}$ waveplate is inserted after the fiber to change the polarization direction of the trapping laser. A high NA objective lens ($NA = 0.85$, LCPLN100XIR, Olympus Corp.) is installed inside a customized vacuum chamber. The trapping laser then is collected with a condensor lens (C330TMD-B, Thorlabs, Inc.) and guided to four balanced detectors (PDB415C-AC or PDB425C-AC, Thorlabs, Inc.). A CMOS camera (DCC1545M, Thorlabs, Inc.) is installed at the side and a CCD camera (BFLY-U3-13S2C-CS, FLIR Systems, Inc.) is aligned at the back of the objective lens.

FC-2, Thorlabs, Inc.) which filters out higher order modes and only releases zero order Gaussian modes of the laser. This not only helps to improve the trapping but also significantly increases the quality of detection. The collimator used at the end of the fiber (F810FC-1064, Thorlabs, Inc.) has a waist diameter of 8 *mm*. The large expansion of the laser beam enables the objective lens to tightly focus the laser and achieve a stiff trapping potential. A $\frac{\lambda}{2}$ waveplate is inserted after the fiber in order to control the polarization direction of the trapping laser. A high NA objective lens ($NA = 0.85$, LCPLN100XIR, Olympus Corp.) is installed inside a customized vacuum chamber. When the trapping laser propagates through the objective lens, the laser is tightly focused and forms an optical trap near the focus of the objective lens. Then the laser is collected with a condenser lens (C330TMD-B, Thorlabs, Inc.) after the trapping position. The collected laser beam is guided to four balanced detectors (PDB415C-AC or PDB425C-AC, Thorlabs, Inc.) in order to monitor and record the motion of the particle in five dimensions. When a particle is trapped, it can be optically verified with the scattered light from the trapped particle using either the CMOS camera (DCC1545M, Thorlabs, Inc.) installed at the side of the trap or the CCD camera (BFLY-U3-13S2C-CS, FLIR Systems, Inc.) aligned at the back of the objective lens (Fig. 3.3).

The vacuum chamber is connected to a dry turbo pump (HiCube 30 Eco, Pfeiffer Vacuum Inc.) allowing the chamber to reach pressures to around 5×10^{-5} *Torr* in the optimal condition. Two pressure gauges are attached to measure a wide range of pressure. The first pressure gauge is the 910 DualTrans (MKS Instruments.) which is able to measure from 1500 *Torr* to 10^{-5} *Torr* and the second is an ion gauge (KJLC 354 Series, Kurt J. Lesker Company) which covers from 5×10^{-2} *Torr* to 1×10^{-9} *Torr*. The observed signals from the balance detectors are sent to a high speed digitizer (CSE8382, DynamicSignals LLC) for recording and post analyzing of the acquired data.



(a) Image of an optically trapped SiO_2 nanoparticle taken with the side CMOS camera. The white spot is from the scattered light of the 1064 nm laser after hitting the particle.



(b) Sample image of an optically trapped silica nanoparticle observed with the back side CCD camera. The green light is the scattered light from the 532 nm laser used for cooling.

Fig. 3.3. Example images of trapped SiO_2 particles observed with different cameras.

3.3 Creating and loading nanodumbbells

Before trapping a nanodumbbell, first we have to be able to create it. Different methods are used to create nanodumbbells including chemical synthesis and physical attaching.

Chemical synthesis was done by our colleagues in Peking university (Fig. 3.4). They first synthesized silica nanospheres with a standardized method. Then aggregation is induced between the particles by chemically treating the surface of each particle to be reactive. After the particles get aggregated, extra coating on the clusters was performed to prevent further aggregation. Then sorting of the particles were done with a centrifuge in order to selectively collect nanodumbbells [95]. Unfortunately, the chemically synthesized nanodumbbells do not survive well under high vacuum environment. We attribute this because of the surface impurity caused by complex chemical steps which can significantly increases the absorption of the laser.

Another method we tried is a physical attachment (Fig. 3.5). We used an AOM in front of the optical trap in order to create multiple optical tweezers similar as in Chapter 2. We first create two individual optical tweezers and spray particles on top of the two traps using a nebulizer. When both traps trap a particle, we move one tweezer towards the other until it merges to one. This method has an advantage in terms of excluding heavy chemistry. However, the chance of having single particles on both traps is quite low. Thus, we found a rather simple but more effective way of creating nanodumbbells.

Creation of nanodumbbells is achievable by controlling the density of the nano particle in the solution. Since the loading of particles is done with a nebulizer (Mabis MiniBreeze Ultrasonic Nebulizer, Mabis Healthcare) it becomes possible to dilute the solution until each water droplets coming out from the nebulizer contains only two particles. When the water droplet gets trapped, the water will evaporate and the two particles inside the water droplet will merge to one and become a nanodumbbell. Of

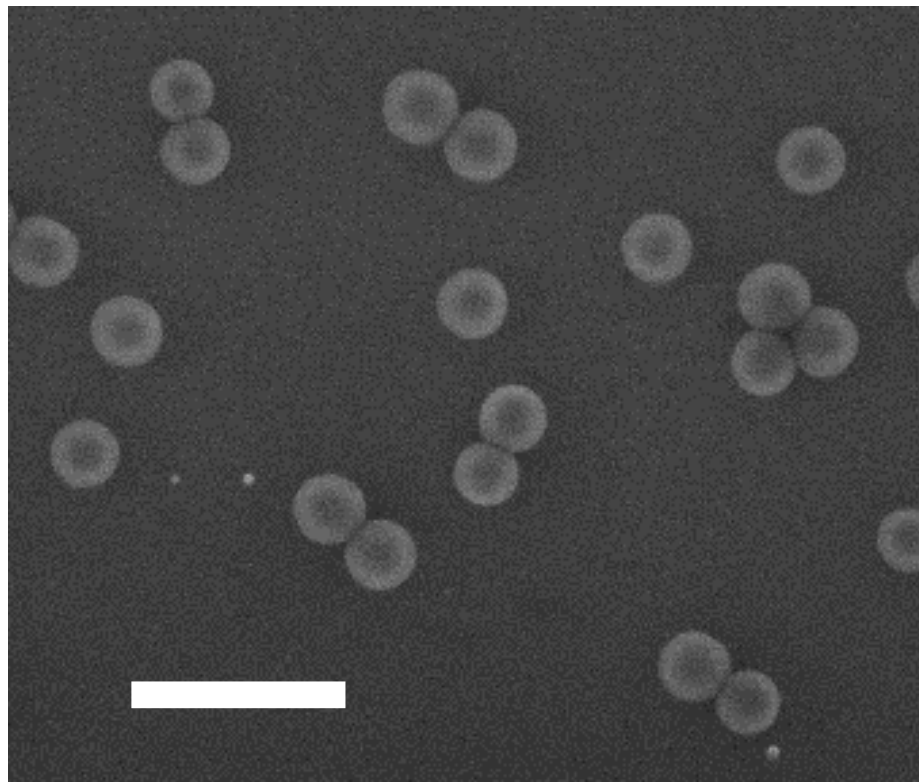


Fig. 3.4. SEM image of chemically synthesized nanodumbbells. Singlets and trimmers are also observable. The size of a single sphere is around 160 nm . The scale bar indicates 500 nm .

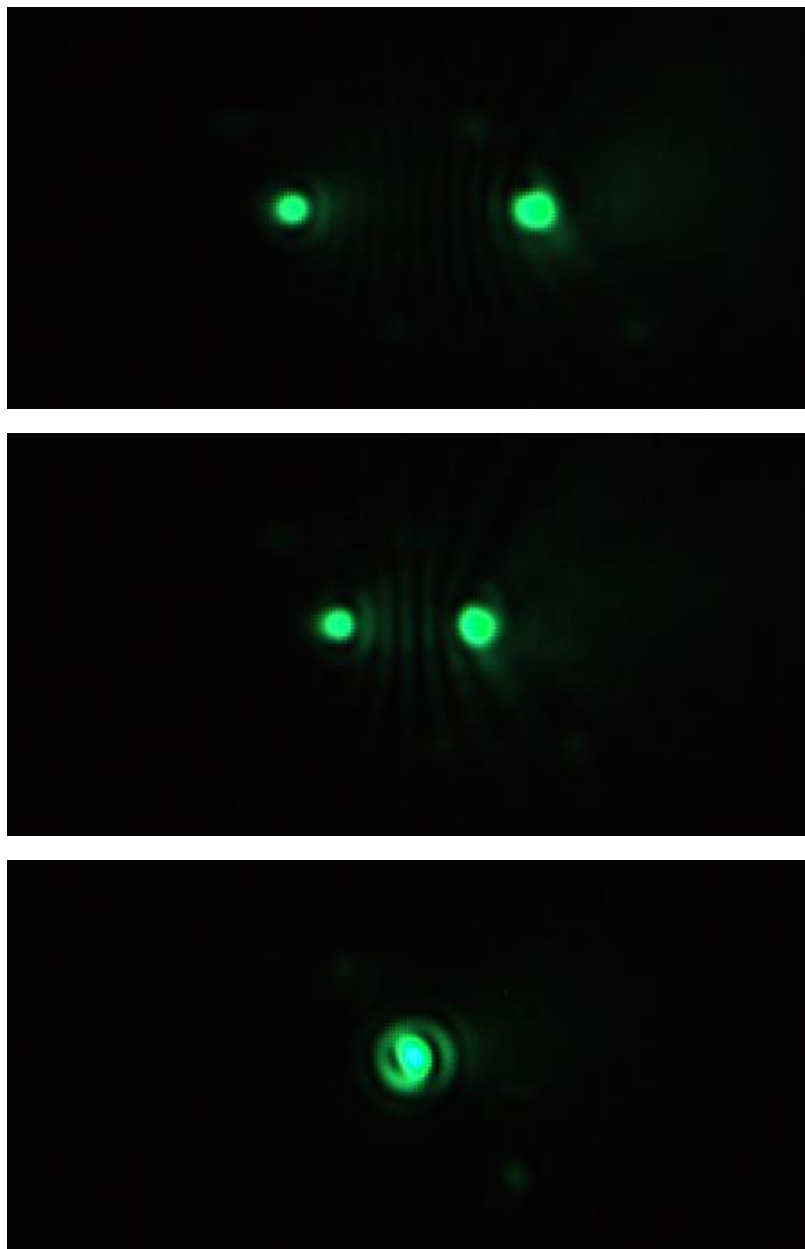


Fig. 3.5. Optical image showing the sequence of physical creation of a nanodumbbell. Two individual particles are first trapped using two optical tweezers (top). One trap is moved closer to the other (middle) until the two traps merge (bottom).

course this process is not always guaranteed but depends on the probability. Thus we have to come up with a measure that can confirm the shape of the particle.

3.4 Characteristics of nanodumbbells inside an optical trap

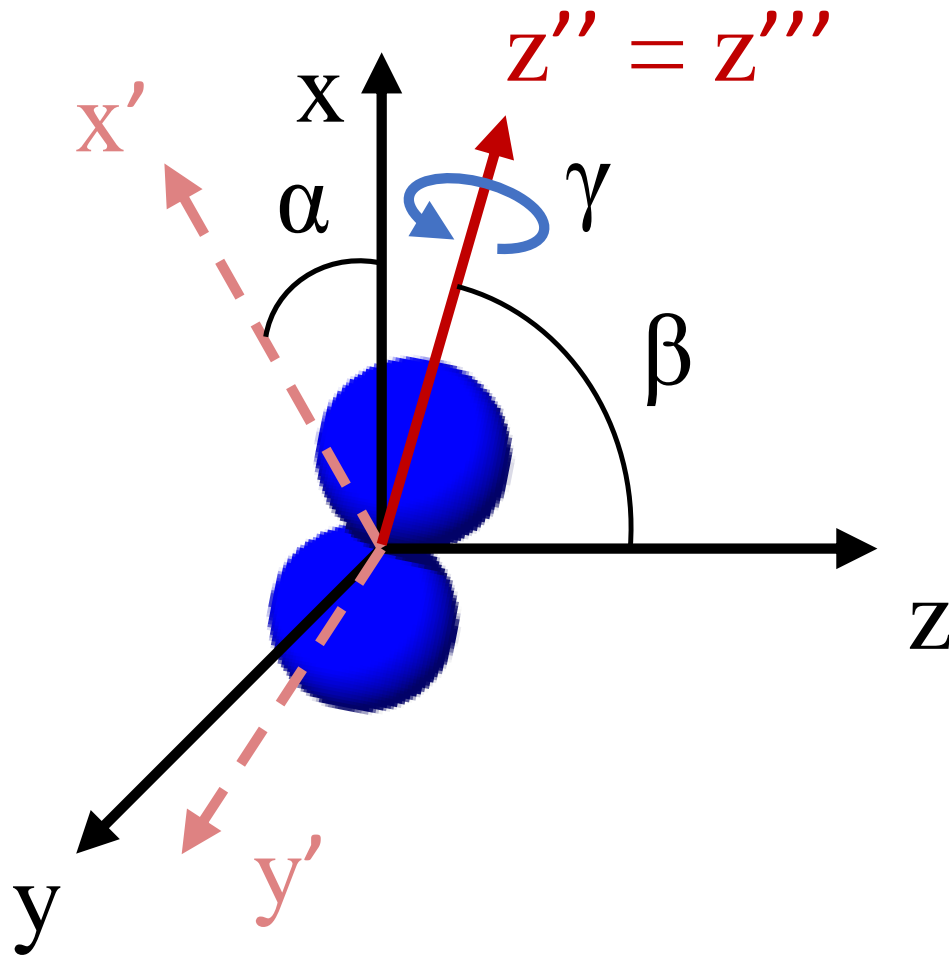


Fig. 3.6. Configuration of a nanodumbbell inside an optical trap. In this experiment, z - y' - z'' convention is used to define the Euler angles [89].

We already know that the particles trapped in an optical tweezer gets confined close to the focus of the laser because of the gradient forces. In case of torsional motion, the confinement comes from the polarization difference of the non-spherical particle along different geometric axes. Due to the difference of polarizability for different dimensions, the long axis of the nanodumbbell tries to align to the laser's polarization direction at the focus. This helps the particle to minimize its potential energy. The collisions of surrounding air molecules induce the nanodumbbell to undergo a confined Brownian motion in 3 translational and 2 torsional vibration modes. However, due to the symmetry of the nanodumbbell along its long axis, it experiences free Brownian rotation around its symmetric axis without any confinement.

Fig. 3.6 shows the Euler convention (z - y' - z'') used to express the rotation of the trapped nanodumbbell. The trapping laser is linearly polarized along the x -direction. Consequently, the trapped nanodumbbell tends to align along the x -axis. The two torsional motions that we are interested in are α and β respectively. Note that the symmetric axes of free rotation of the nanodumbbell is aligned to ($z'' = z'''$) and the angle is defined as γ . Other axis are omitted to keep the schematic simple. The potential energy of a small nanodumbbell in a linearly-polarized Gaussian optical tweezer can be written as:

$$U(\alpha, \beta, x, y, z) = -\frac{1}{4}[\alpha_{\perp} + (\alpha_{\parallel} - \alpha_{\perp}) \cos^2(\alpha) \sin^2(\beta)] \times \frac{E_0^2}{1 + (\frac{z}{z_0})^2} \exp[-\frac{2x^2}{w_x^2(z)} - \frac{2y^2}{w_y^2(z)}], \quad (3.1)$$

where α_{\parallel} (α_{\perp}) is the polarizability parallel (perpendicular) to the axis of the nanodumbbell and E_0 is the electric field amplitude of the trapping laser at the focus. $w_{x,y}(z) = w_{x,y}(z=0) \cdot \sqrt{1 + z^2/z_0^2}$ is the beam waist radius, and z_0 is the Rayleigh range of the optical tweezers. From the equation above, it can be predicted that the nanodumbbell gets trapped close to the focus and simultaneously aligned parallel to the polarization axis of the trapping laser. The equilibrium orientations of the nanodumbbell are when $\alpha = 0$ and $\beta = \frac{\pi}{2}$. The trapping potential $U(\alpha, \beta, x, y, z)$ is independent of γ since the particle is symmetric along the γ degree of freedom

(Fig. 3.6). The trapping potential as a function of the motion along the y axis $U_y \equiv U(\alpha = 0, \beta = \frac{\pi}{2}, x = 0, y, z = 0)$ and the trapping potential as function of the rotation along α direction $U_\alpha \equiv U(\alpha, \beta = \frac{\pi}{2}, x = 0, y = 0, z = 0)$ are shown in Fig. 3.7.

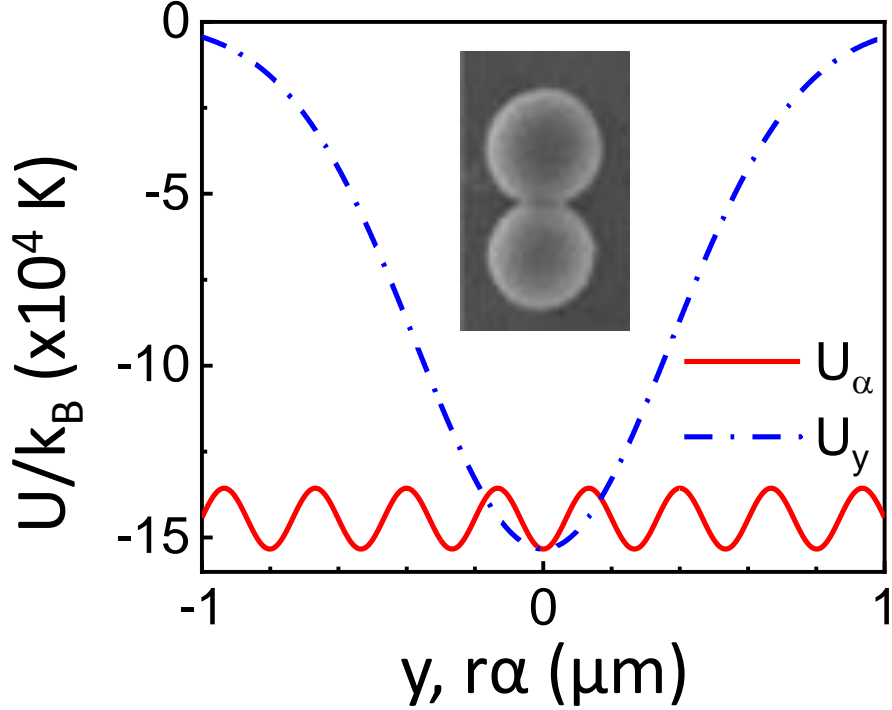


Fig. 3.7. Shape of trapping potentials as a function of displacement. The blue line indicates the potential of a translational motion along the y axis. The red line presents the potential of a torsional vibration in α direction. For direct comparison, the radius $r = 85$ nm is multiplied to the angle α for the rotational (torsional) potential. Inset is a SEM image of a nanodumbbell.

The out-going laser beam after the trap is collected with a collimation lens and guided to four balanced photodetectors to observe the motion of each degree of freedom. Except the measurement of the torsional vibration in the β direction, the optical configurations to detect the motion of the nanodumbbell are similar to those of our previous reports [53, 86]. As shown in Fig. 3.8, the signal obtained from the

detector which is for the translational motion in the x -direction also contains the information of the torsional vibration in the β -direction. This is because the rotation of the nanodumbbell along the β direction deflects the laser beam in the β direction, which eventually causes a shift of the laser beam along the x axis [89]. Since the c.m. motion and the torsional vibration have different frequencies, those signals can be well separated by using band-pass filters.

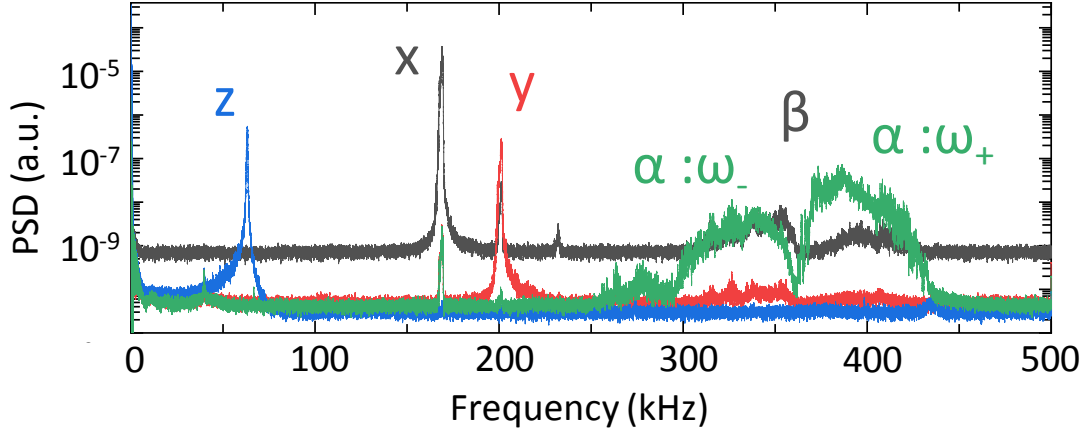


Fig. 3.8. Power spectral density (PSD) measured for a nanodumbbell consisting of two 170 nm silica spheres. PSDs obtained from four different detectors x , y , z and α are shown together. The PSD for the β motion is achievable from the high frequency part of the x detector. These PSDs are taken at a pressure of 3×10^{-3} Torr with x , y and z motion cooling. The data acquisition time is 1 sec.

3.5 Determination of a levitated nanodumbbell

Because of the method used to trap nanodumbbells, a standardized procedure to recognize the shape of the trapped particle is necessary. Since the trapped particles are only in the size of around 300 nm, it is impossible to observe the shape of the trapped particle by an optical microscope image. Yet, there is a relatively simple method to distinguish the geometry for different particles. Because of the geometrical

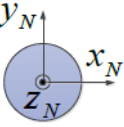
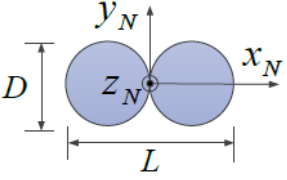
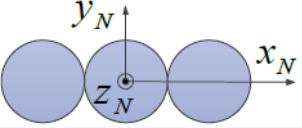
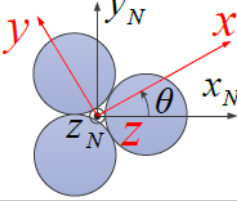
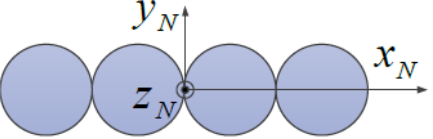
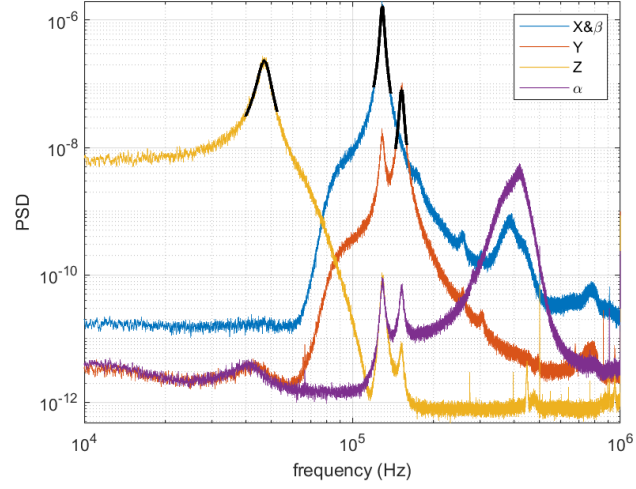
Particle type		Γ_y/Γ_x	Γ_z/Γ_x
Sphere		1	1
Dumbbell		$L/D = 1.9$	1.276
		$L/D = 2.0$	1.258
Chain trimer		1.378	1.378
Triangle trimer		0.997-1.004	1.133-1.136
Chain tetramer		1.448	1.448

Fig. 3.9. Ratio of damping rates for various shapes of nanoparticles [53].

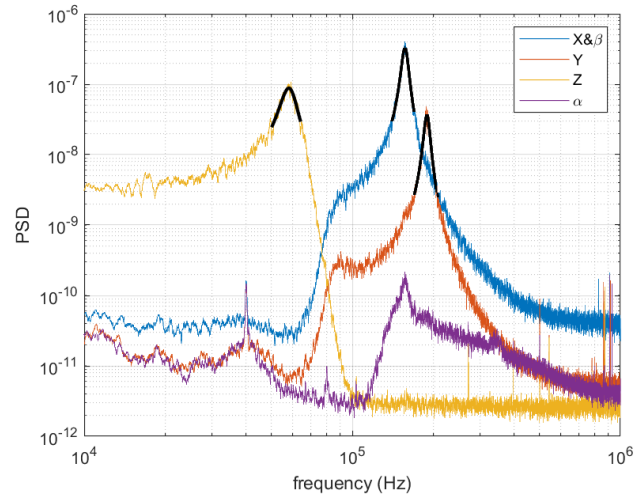
difference, the ratio of the damping rates among different dimensions suppose to be different. Therefore, if we are able to know the ratios for different particle geometries, it becomes possible to recognize the geometry of the trapped particle in situ. To know the ratios, a “Direct Simulation Monte Carlo (DSMC)” simulation was performed to determine the damping rate of various shape of the particles [53]. The result of the simulation is shown in Fig. 3.9. Obviously, the damping rate ratio of a spherical particle is “1” because of the symmetry. On the other hand, the ratio of damping rate for different dimension becomes “1.276” when the particle is a dumbbell with $L/D = 1.9$ (which is close to our case). Thus, measuring the damping rate for each dimensions provides us the idea of what we have in the trap. Damping rates can be measured by fitting the PSDs of each dimensions with [96]:

$$S(\omega) = a_0 \frac{\Gamma_0}{(\Omega^2 - \omega^2)^2 + \omega^2 \Gamma_0^2}, \quad (3.2)$$

where a_0 , Γ_0 and Ω_0 are the fitting parameters. By extracting Γ_0 for each direction, we can confirm the geometry of the trapped particle. Examples of power spectral densities for nanodumbbell and nanosphere are shown in Fig. 3.10. From Fig. 3.10(a), it can be seen that for a nanodumbbell, not only the ratio of damping rates are as expected ($\Gamma_x/\Gamma_y = 1.275$) but also a distinct peak shows up on the α signal (purple). Compared to the nanodumbbell, nanospheres do not have obvious peaks in the torsional directions.



(a) Power spectral densities of a nanodumbbell. PSDs of each directions are fitted to determine the damping rate(black). $\Gamma_x/\Gamma_y = 1.275$.



(b) Power spectral densities of a single nanosphere. PSDs of each directions are fitted to determine the damping rate(black). $\Gamma_x/\Gamma_y = 1.00$.

Fig. 3.10. Example of Power spectral densities for (a) nanodumbbell and (b) nanosphere trapped with our system. Each PSDs corresponds to x (blue), y (orange), z (yellow), α (purple) and β (higher frequency part of blue) respectively. Different band-pass filters are applied for each degree of freedom.

4. FEEDBACK COOLING OF A NANODUMBELL IN FIVE DEGREES OF FREEDOM

4.1 Motivation

In recent years levitated optomechanics has provided a fruitful platform for fundamental physics and applications [97, 98]. After the demonstration of millikelvin cooling of the c.m. motion of a levitated microsphere in vacuum several years ago [39], researchers are now able to cool the c.m. motion of a nanosphere to microkelvin temperatures and observe its quantum behavior [43, 99, 100]. Compared to experiments with levitated spherical nanoparticles, however, experiments with levitated nonspherical nanoparticles are still in their early stages. One of the main reasons is that optically levitating a nonspherical nanoparticle in high vacuum was not very successful for a long time [52]. Until now, people believe that the reason for losing particles in a high vacuum environment is because of the heating due to the absorption of the trapping laser [50]. Even these days, no other nano-material than high purity silica (SiO_2) and calcite (CaCO_3) were successfully trapped in high vacuum using optical tweezers. Therefore, in order to trap and maintain a nonspherical particle in high vacuum environment using optical tweezers, it is unavoidable to find particles which has geometrical asymmetry and good optical properties (less absorption) at the same time.

Recently, this challenge was partially overcome by optically levitating high-purity silica multi-particles with 1550 *nm* lasers [53, 54, 88]. Before, most of the optical tweezers were realized using 1064 *nm* lasers [14, 40]. However, the photon absorption rate of SiO_2 is about twice less in the case of shining a 1550 *nm* laser compared to a 1064 *nm* laser [101]. The low absorption rate indicates less heating of the trapped particles which again is closely related to the loss mechanism. As a result, by using a

1550 *nm* laser for the trapping beam, nonspherical particles were able to be trapped in higher vacuum and even could be driven to rotate at GHz frequencies with a circularly-polarized laser [49,53,54]. The fast rotating nonspherical silica particles in high vacuum indeed opened up a new chapter in rotational levitated optomechanics.

Nonetheless, there are still remaining questions requiring a different path than rotational levitation. One of the challenges of a fast rotating particle comes from the different intrinsic nature of a full rotation compared to a simple translational oscillation. To be more specific, the translational motion of a levitated particle inside an optical tweezer is possible to be safely considered as a harmonic oscillator assuming the particle stays near the focus [102]. Thus, characterising the system becomes relatively straight forward similar to the case of other mechanical oscillators [103]. However, in case of continuously rotating objects, no conservative force exist which makes the system harder to characterize using traditional concepts of harmonic oscillators such as conservative energy or temperature. Moreover, observing the direction of rotation becomes technically challenging especially when the rotational speed is extremely high. Absence of the directional information can be disadvantageous when the system needs to be used as a sensor when vectorial information are required.

Consequently, an asymmetric particle yet staying stationary in vacuum environment is necessary to complement the gap of the rotational levitation. In this chapter, 5D cooling of a levitated silica nanodumbbell will be discussed in details. As discussed in the previous chapter, the nanodumbbell will undergo confined Brownian motion in three translational and two torsional vibration modes. The sixth degree of freedom is not confined and experiences free Brownian rotation around its symmetric axis. For the rest of this chapter, basic concepts of feedback cooling, experimental setup to realize feedback cooling and the results of 5D cooling will be covered.

4.2 Optical feedback cooling of a levitated nanoparticle

4.2.1 Feedback cooling of a mechanical oscillator

Cooling the Brownian motion of a mechanical oscillator is a well known technology and diverse methods are introduced for both active and passive cooling [104,105]. Millikelvin temperatures are achieved for different designs of mechanical oscillators using feedback cooling [104–106]. By means of coupling an optical cavity to the mechanical cavity, quantum ground state cooling has been demonstrated for a fabricated nanomechanical oscillator [107].

These methodologies are analogously adopted to the field of levitated optomechanics as mentioned in the previous section. To be more specific, both active cooling [4, 39–41, 99, 108] and cavity cooling schemes were tested on levitated particles [42, 43, 46, 47]. Active cooling uses electromagnetic field to provide additional damping to the particle where the damping effect due to the surrounding gas molecules significantly decreases as the system reaches to vacuum environment. Usually a laser is commonly used as the source of an electromagnetic field but other sources such as electric field induced by a plate capacitor also could be used [99]. On the other hand, passive cooling is a technique achieving energy transfer from a mechanical cavity to a coupled optical cavity by detuning the driving frequency. Among these different cooling methods, the first motional quantum ground state cooling was achieved by cavity cooling [43].

Even though the best cooling result was achieved by cavity cooling, it does not necessarily imply that other methods are useless. In most cases, active feedback cooling is easier to be integrated with an levitated optomechanical system because in a levitated optomechanical system, it is challenging to keep the cavity mirrors flawless because of the particle loading process. Also, so far, only cavity cooling mediated by side scattered light could achieve ground state cooling which bears the possibility of having limitation for certain degrees of freedom. Lastly, even though active feedback cooling did not reach quantum ground state yet, the ability to cool the mechanical

motion of the levitated particle is approaching to that of cavity cooling and researchers are able to observe quantum phenomena using active feedback cooling [41, 100].

For the 5D cooling of a levitated nanodumbbell in this chapter, we use active feedback cooling to cool all five degrees of freedom interacting with the trapping laser.

4.2.2 Active feedback cooling of a levitated particle

In the relatively short history of levitated optomechanics, two representative cooling schemes are widely used. One is the force feedback cooling [39] and the other is parametric feedback cooling [40]. These two cooling techniques share a common basis in the sense that both provide additional damping to the particle with lasers. The intensity of cooling lasers are modulated using optical modulators (such as AOM or EOM) based on the observed motion of the particle. The main difference of these two is that force feedback cooling uses additional cooling lasers on top of the trapping laser whereas parametric feedback cooling modulates the intensity of trapping laser itself. Both techniques have their own advantage and disadvantage. In case of force feedback cooling, the biggest disadvantage is the additional heating because of the presence of the cooling lasers. As previously mentioned, photons get absorbed by the levitated particle which causes temperature increase of the particle. The increased temperature not only lead the system to be highly nonlinear but also increases the possibility of the particle to be lost. Also, careful alignment of the cooling lasers regarding to the position and configuration of the optical tweezer is required to achieve optimal cooling. On the other hand, the principle of cooling using radiation pressure is relatively easier than that of a parametric feedback cooling which makes the electrical feedback circuit less complex. This is technically important because as the analog circuit requires more components it becomes more challenging to reduce the noise of the outcoming signal. The higher the signal noise becomes, the worse cooling is achieved. Contrarily, parametric feedback cooling does not require an additional cool-

ing laser since the trapping laser itself is modulated to cool the motion of the particle. The absence of additional laser not only causes less heating of the trapped particle but also reduces the complexity of optics dramatically compared to force feedback scheme. However, modulating the trapping laser is disadvantageous for detection because for most of the levitated optomechanical systems, the motion of the trapped particle is monitored by detecting the trapping laser itself. In order to distinguish the signal of the trapped particle from the modulation, two different methods have been exploited. First method is to use a probing laser which has a different polarization direction from the trapping laser [40]. Using a separate probing laser however loses the advantage of parametric feedback cooling in certain extent. The other method is to use a high order band-pass filter or phase lock loop (PLL) [109] which makes the circuit highly complex and cost inefficient.

In this experiment, in order to cool the translational and torsional vibrations of a nanodumbbell, three linearly polarized cooling lasers are applied along x , y and z directions as illustrated in Fig. 4.1. A wavelength of 532 nm laser is used for the x -cooling whereas the wavelengths of the y - and z -cooling lasers are chosen to be 976 nm . The reason for choosing different tones of lasers is to minimize the interference between each cooling lasers, as well as to lessen the absorption of the silica particle (by using 976 nm laser instead of only using 532 nm laser for all three directions). The three cooling lasers are focused at the trapping position using aspheric lenses. However, the waists of the cooling lasers are intentionally set to be larger than the trapping laser to only provide scattering force to the particle without adding unnecessary gradient forces which can distort the trapping potential. The intensities of the x - and y -cooling lasers are estimated to be roughly 1 $mW/\mu m^2$, and the intensity of the z cooling laser to be roughly 5 $mW/\mu m^2$. Similar to other experiments using force feedback cooling [4, 39], the scattering forces from the three cooling lasers are used to cool the three corresponding c.m. motions of the levitated nanodumbbell. In order to cool the torsional vibrations (α and β), the polarization axes of the y - and z -cooling lasers are intentionally tilted by about 10 degrees with respect to the direction of

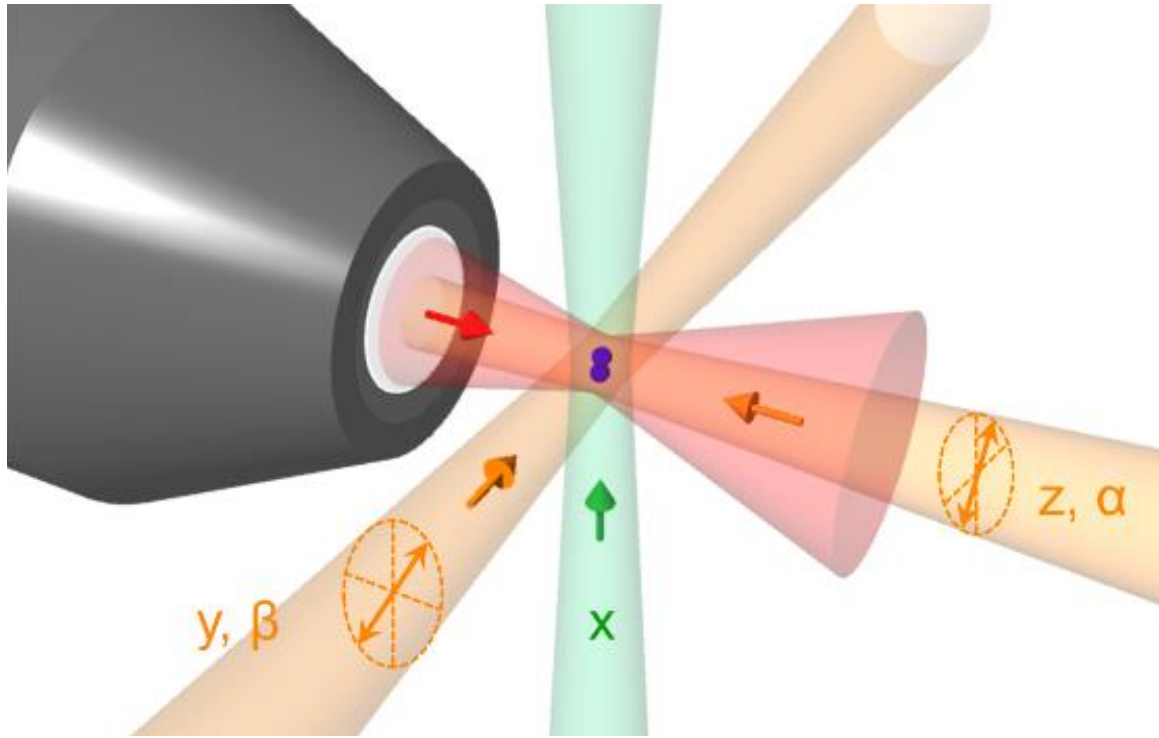


Fig. 4.1. Schematic illustration of 5D cooling. A 1064 nm laser is used to levitate a nanodumbbell in vacuum. Cooling lasers and their directions of propagation are illustrated in green (x -cooling laser, 532 nm) and orange (y - and z -cooling lasers, 976 nm). The polarization directions of the y - and z -cooling lasers are tilted to form an angle of about 10 degrees with respect to the polarization direction of the trapping laser. The polarization direction of the x -cooling laser is parallel to y axis.

polarization of the trapping laser (Fig. 4.1). By tilting the polarization direction, the z -cooling laser can exert a drag torque on the nanodumbbell to cool its α torsional mode, where as the y -cooling laser can cool its β torsional vibration mode with the same principle. The occurrence of the drag torque can be understood in the same way as the confinement of the nanodumbbell inside a linearly polarized optical trap, where the top like particle tries to match its long axis parallel to the polarization direction to minimize the potential energy. The polarization direction of the x -cooling laser is kept to be parallel to the y axis in order to prevent disturbance of other torsional modes.

4.3 Force feedback control loop

Fig. 4.3 shows the full configuration of the feedback control loop used in 5D cooling. As shown in Fig. 4.3, three translational and two torsional motion signals of the nanodumbbell are observed using the four balanced detectors. Five home-built analog circuits (indicated in the dashed box in Fig. 4.3) are used to process the corresponding cooling signals. Each signal is sent to the according electronic circuits to generate a feedback signal corresponding to the motion of the particle. The feedback signals produced using the analog circuit are fed into three different acousto-optic modulators (1206C and 1205C, Isomet Corporation, DTD-274HD6, IntraAction Corp.) in order to control the powers of the three cooling lasers. As stated above, the cooling lasers provide additional damping to the particle depending on the intensity and propagation direction of the laser. The powers of the cooling lasers are modulated as $\Delta P_x = -C_x \frac{dx}{dt}$, $\Delta P_y = -C_y \frac{dy}{dt} - C_\beta \frac{d\beta}{dt}$ and $\Delta P_z = -C_z \frac{dz}{dt} - C_\alpha \frac{d\alpha}{dt}$ to achieve 5D cooling. Note that the two torsional signals β and α are added to y and z direction respectively. Here C_x , C_y , C_z , C_α and C_β are modulation coefficients controlled by variable gain amplifiers. The feedback circuit consists of an active band-pass filter, differential circuit, variable gain amplifier and a unity gain inverting amplifier (which is in parallel with a voltage follower). The signal after the variable gain amplifier is

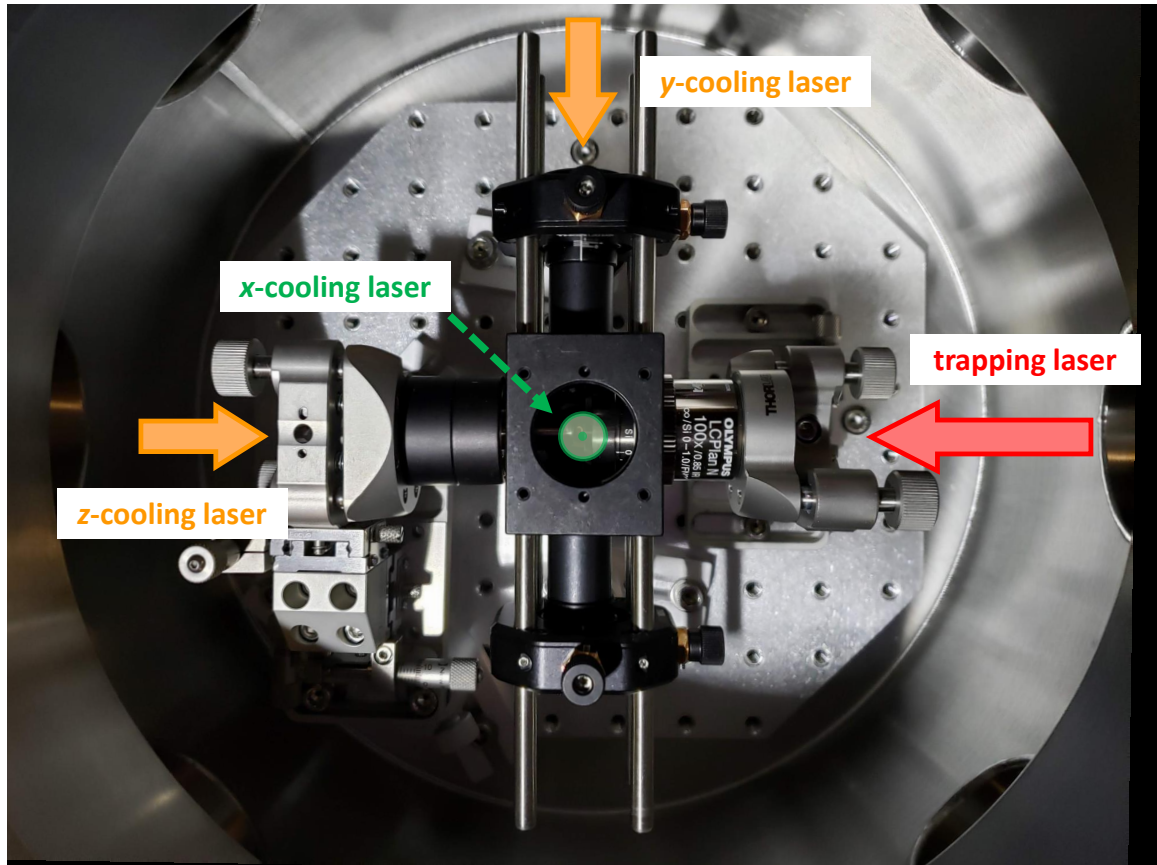


Fig. 4.2. Photo of optics configuration inside the vacuum chamber. The trapping laser (red arrow) is guided through a high NA objective lens. Each cooling laser are focused to the trapping position using aspheric lenses: 1) x -cooling laser: C280TMD-A, Thorlabs, Inc., 2) y -cooling laser: C280TMD-B, Thorlabs, Inc. and 3) z -cooling laser: C330TMD-B, Thorlabs, Inc.

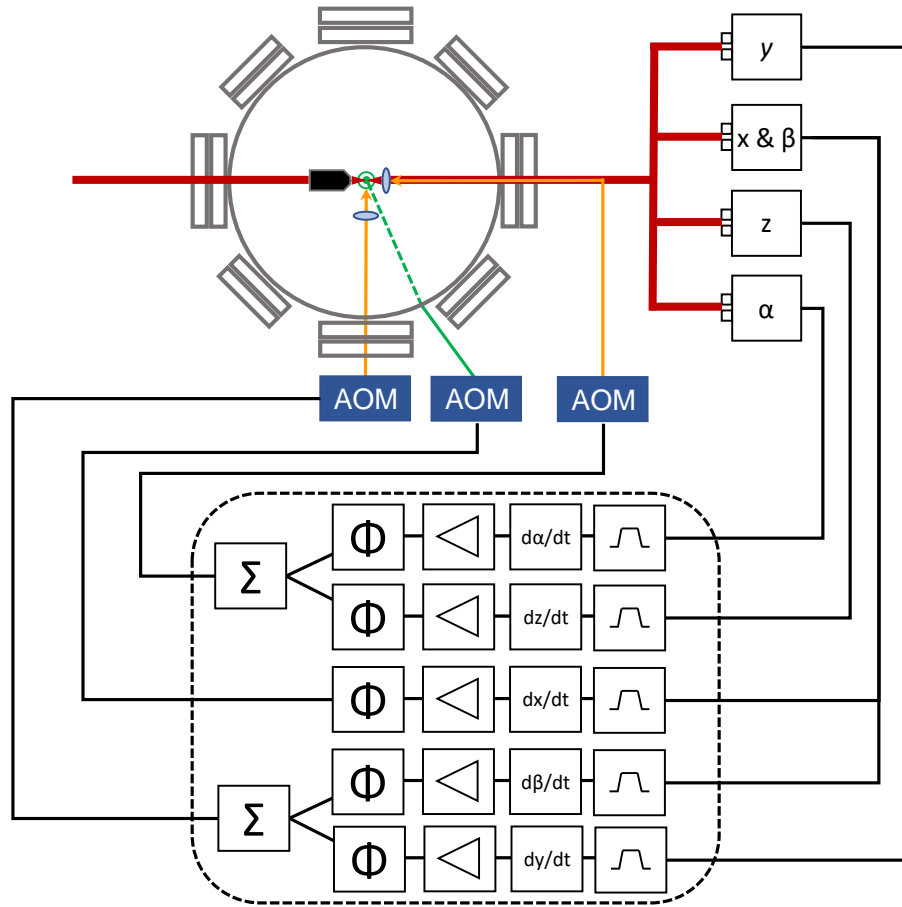


Fig. 4.3. Schematic of the setup showing the sequence of cooling of a levitated nanodumbbell. The home built analog circuit is indicated with the dashed lines. The signal obtained from the balanced detector for both x and β motions is split into two and fed into two different derivative circuits to generate the corresponding cooling signals for the motion in x and β directions. After processed thorough the circuit, signals corresponding to α and β motions are added to the signals for z and y motions, respectively (Fig. 4.1).

split to two and fed to either a voltage follower or an inverting amplifier. With this design, it becomes easier to choose the right signal with the right phase since the relative phase difference between the observed motion and the feedback signal has to be correctly adjusted to achieve cooling. In order to achieve high quality motion signals as well as to distinguish the β torsional vibration from the x translational mode, additional higher order band-pass filters were used in series in front of the home built circuits.

4.3.1 Band-pass filter

Band-pass filters filter out signals in the unwanted bands and increases the quality of the signal in the desired band width. Even though the levitated optomechanical system is built to be secure from environmental noise to some extent, fully protecting the system from various noise sources is extremely challenging. If certain noise signals are added to the feedback signal, it will be reflected to the intensity modulation of a cooling laser. This will perturb the optimum cooling and raise the temperature of the corresponding motion. Thus, using band-pass filters with the right bandwidth is necessary to realize motion cooling. The home built circuit used in this experiment has multiple band-pass filters at the beginning. In order to cut the low frequency mechanical noise and high frequency radio frequency noise, a simple active band-pass filter was arranged at the beginning (Fig. 4.4). The high frequency cutoff for this band-pass filter could be calculated as $f_H = \frac{1}{2\pi R1C1}$. Similarly, the low cutoff frequency is $f_L = \frac{1}{2\pi R2C2}$. The input signal (V_{in}) usually decreases as it passes the filter. Therefore, amplifying the signal can become important in many cases. The amplification factor of the signal for this design is roughly decided by the ratio of the two resistors as $A_v = \frac{R3}{R4}$. For the circuit used in this experiment, the gain is set to be $A_v = 10$. The cutoff frequencies are set to be $f_H = 1kHz$ and $f_L = 1MHz$ respectively.

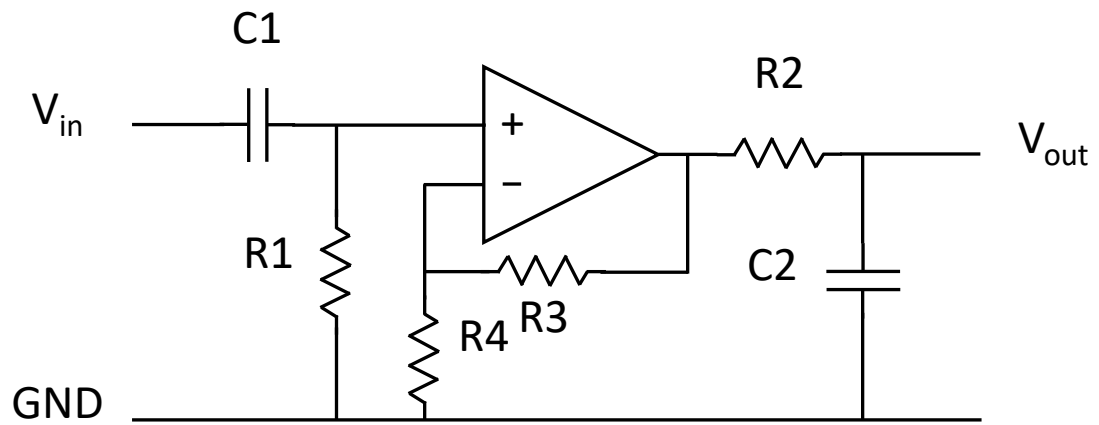


Fig. 4.4. Schematic of a first order active band-pass filter

This kind of band-pass filter covering a wide band illustrated above works decently for low frequency mechanical noise or high frequency electrical noises. However, the moderate filtration is sometimes not enough for cooling. This is because for most cases, the detected signal from a balanced detector does not only have the desired signal but also contains small portions of signal from other directions. The presence of unwanted signals can be caused due to alignment imperfection, time and pressure dependent drifting of the system and distortion of the trapping laser because of the high NA objective lens. Nonetheless, in order to achieve optimal cooling, it is necessary to filter out other signals from other degrees of freedom. Usually, the characteristic frequencies of motion in each degrees of freedom are not well separated requiring higher order filters. Fifth-order or sixth order elliptic filters are thus added to reject unwanted signals and only select the desired signal for cooling.

4.3.2 Differential circuit

The differential circuit is the most important block in the sequence of force feedback circuitry. The differential circuit calculates the derivative of the motional signal and provides velocity information for cooling. For simplicity, if assuming only one directional motion of a levitated nanodumbbell, the equation of motion could be expressed as [96]:

$$\ddot{x} + \Gamma_0 \dot{x} + \Omega^2 x = \Lambda \zeta(t), \quad (4.1)$$

where $\Omega = \sqrt{k/M}$ is the natural frequency of the particle, Γ_0 the damping rate, $\Lambda = \sqrt{2k_B T \Gamma_0 / M}$ and $\zeta(t)$ the stochastic random noise. As stated above, if the motional signal $x(t)$ goes through the differential circuit, it becomes $\dot{x}(t) = v(t)$. Thus, if the feedback signal is applied in the form of radiation pressure, Eq. 4.1 becomes:

$$\ddot{x} + \Gamma_0 \dot{x} + \Omega^2 x = \Lambda \zeta(t) \mp C_{fb} v(t), \quad (4.2)$$

where C_{fb} is a constant determined by the amplification factor of the whole feedback loop. Based on the configuration of the feedback loop including optical configuration,

C_{fb} can be either positive or negative. By rearranging the feedback force term, we can get [96]:

$$\ddot{x} + (\Gamma_0 \pm \Gamma_{fb})\dot{x} + \Omega^2 x = \Lambda\zeta(t), \quad (4.3)$$

where we set $C_{fb} = \Gamma_{fb}$. The equation indicates that the feedback force applied to the system can be thought as a change in damping rate and only changes the damping rate of the system. More importantly, depending on the direction of the feedback constant Γ_{fb} , the feedback scheme can either increase (effective cooling of motion) or decrease (effective heating) the damping rate.

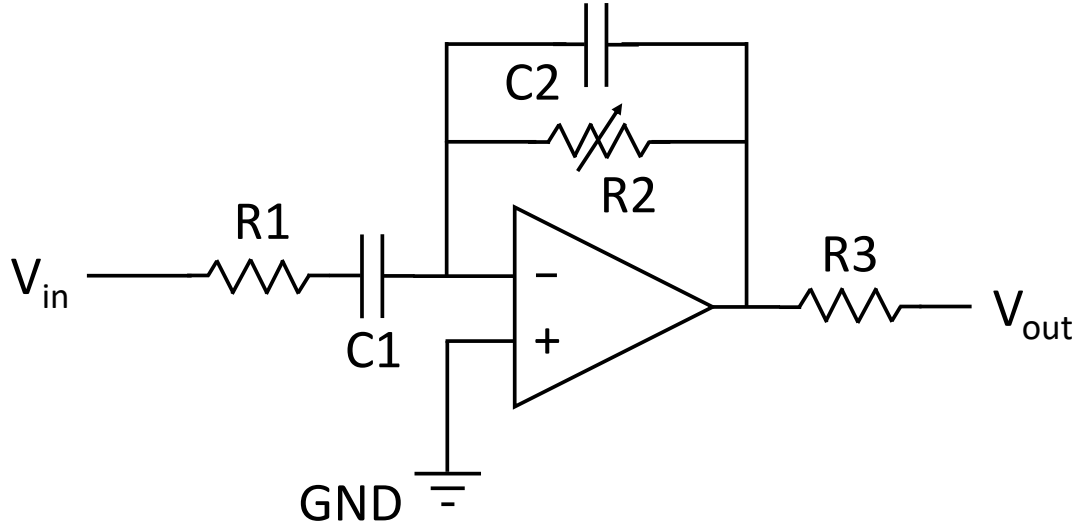


Fig. 4.5. Schematic of a differential circuit. This circuit calculates the velocity of a levitated particle based on the displacement signal acquired from the balanced detector.

The schematic of the differential circuit is shown in Fig. 4.5. An ultralow noise ($1.1 \text{ nV}/\sqrt{\text{Hz}}$) operational amplifier (OPA1611, Texas Instruments) is used for the circuit. The time of differentiation can be determined as $C1 \times R2$ [96]. The resistance of $R2$ is tuned so that the gain of the differentiator is unity.

4.3.3 Variable gain amplifier

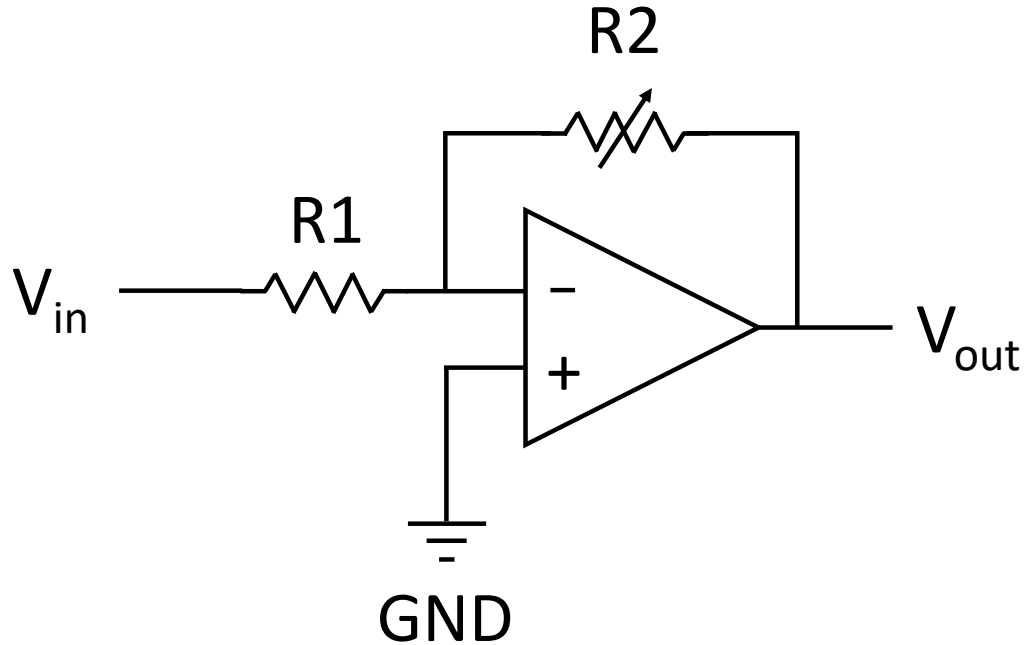


Fig. 4.6. Schematic of a variable gain amplifier. This circuit amplifies the input signal V_{in} . The gain of the circuit can be controlled by tuning the potentiometer.

Adjusting the amplitude of the feedback signal is important mainly because of two reasons. The first reason is the fact that every instruments have different range of input and output voltages. For example, the RF output of the balanced detectors used in this experiment (PBD4x5C-AC, Thorlabs, Inc.) is $\pm 3.6V$ and the actual signal acquired from each detectors vary because the optical paths are different (Fig. 4.7). On the other hand, the acousto-optic deflector used for the z -cooling (DTD-274HA6, IntraAction Corp.) has an input voltage range of $0V$ to $1V$. Therefore, every feedback channel has to be adjusted to have the right amplification to achieve maximum mod-

ulation without exceeding the range of voltage input of the AOM. Another important reason is the fact that as the particle gets cooler, the amplitude of the detection signal gets smaller. Therefore, it becomes necessary to increase the gain of the circuit as the vacuum level goes higher to further cool the motion of the particle. The gain of the amplifier can be determined as $A_v = \frac{R2}{R1}$. Considering the stability of the op-amp, each components are chosen to be $R1 = 1k\Omega$ and $R2 = 10k\Omega$ respectively.

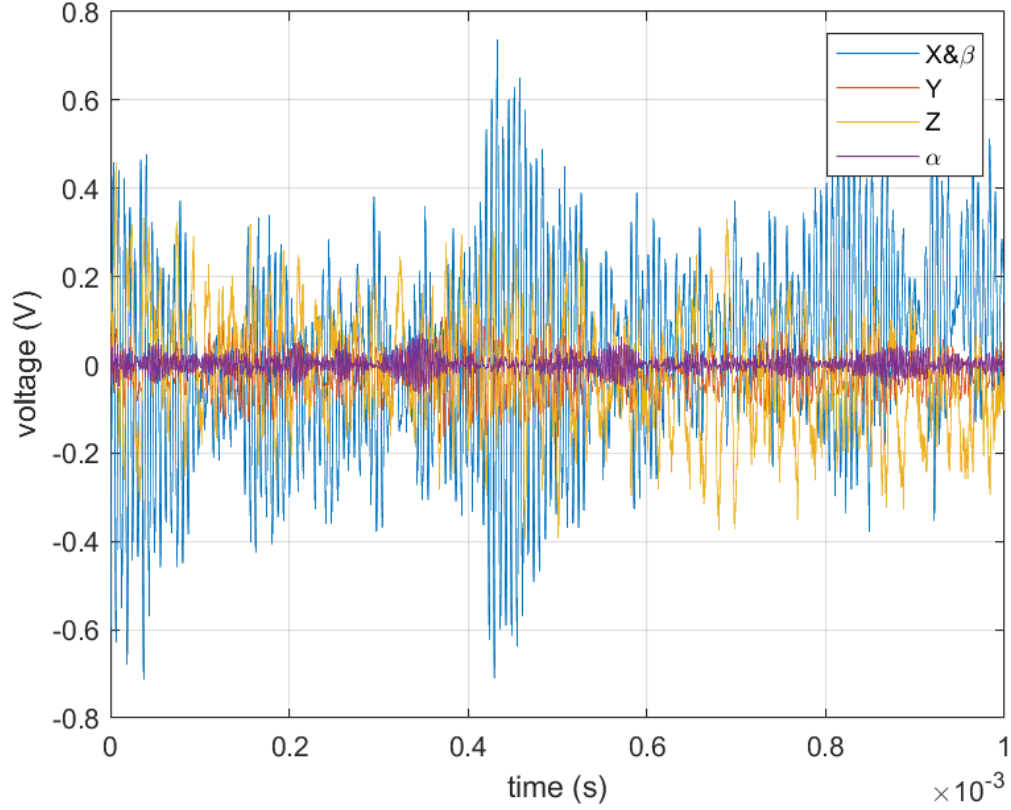


Fig. 4.7. Voltage signal acquired from four balanced photo-detectors. The voltage oscillation of each plot represents the corresponding oscillation of each degree of freedom. $1ms$ of data is shown in the plot.

4.3.4 Unity gain inverting amplifier

The unity gain inverting amplifier in this experiment is used as a phase shifter. In order to achieve motional cooling of the levitated particle, it is important to provide a counter acting force (in this case the radiation pressure of the cooling lasers) with the right phase (Fig. 4.8). Initially, an all-pass filter was planned to be used in order to precisely adjust the phase delay. However, all-pass filters are highly sensitive to the frequency of an input signal which can be disadvantageous for our system (because the frequency of oscillation starts to fluctuate as the system goes to higher vacuum.) Even though phase delays occur at every step of the feedback loop, the accumulated phase delay is quite small considering the frequency of the motion we are dealing with (typically in the order of 100 kHz). The more important part to be considered is the unwanted inversion of the signal along the feedback loop. For example, some components in the feedback circuit have negative gain which inverts the signal by 180 degrees. Also, the directional relation between the particle's motion and the propagation direction of the cooling laser matters. From Fig. 4.8, it can be seen that a wrongly inverted feedback signal will rather heat up the motion instead of cooling it down. Thus, the ability to invert the feedback signal is necessary. In our feedback circuit, the output signal from the differentiator is split to two to have two options. One line is connected to a voltage follower which will keep the phase of the signal and the other is connected to the inverter to flip the signal by 180 degrees. The inverter was simply realized by changing "R2" in Fig. 4.6 from a potentiometer to a fixed resistor which satisfies $R1 = R2$.

4.3.5 Summing amplifier

As shown in Fig. 4.3, the two torsional cooling signals for α and β motions are added on top of the translational cooling signals for z and y motions using summing amplifiers. This could be possible since the frequencies of the translational motions (typically 50 kHz 200 kHz) are different from the frequencies of the torsional vibra-

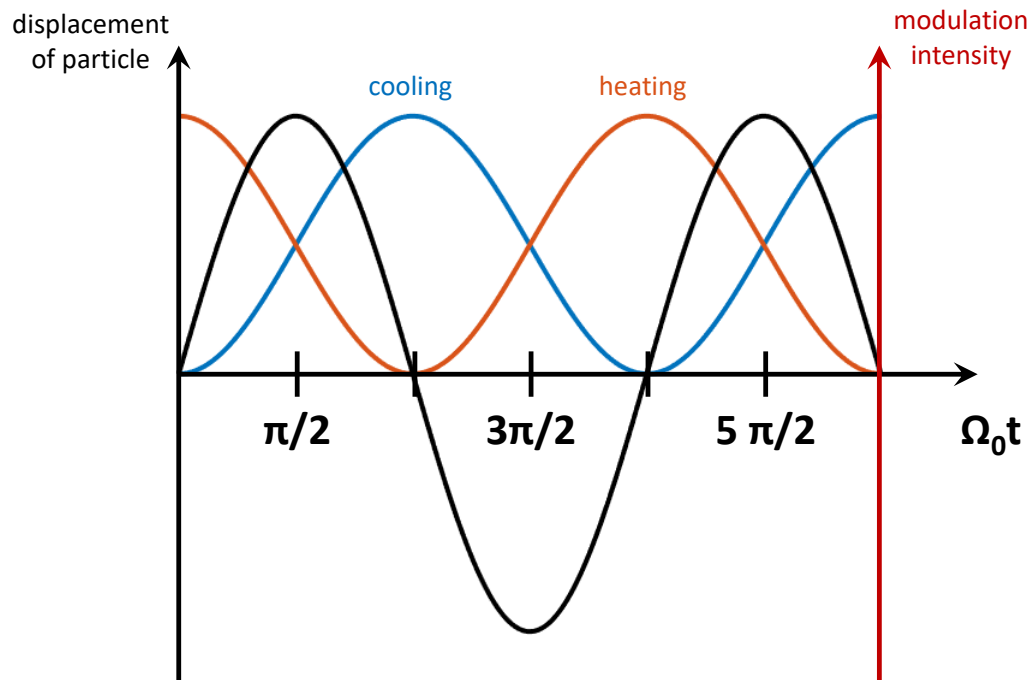


Fig. 4.8. Relation between the motion of the particle and the feedback signal. The feedback signal has to be shifted by $\frac{\pi}{2}$ from the motional signal to achieve cooling.

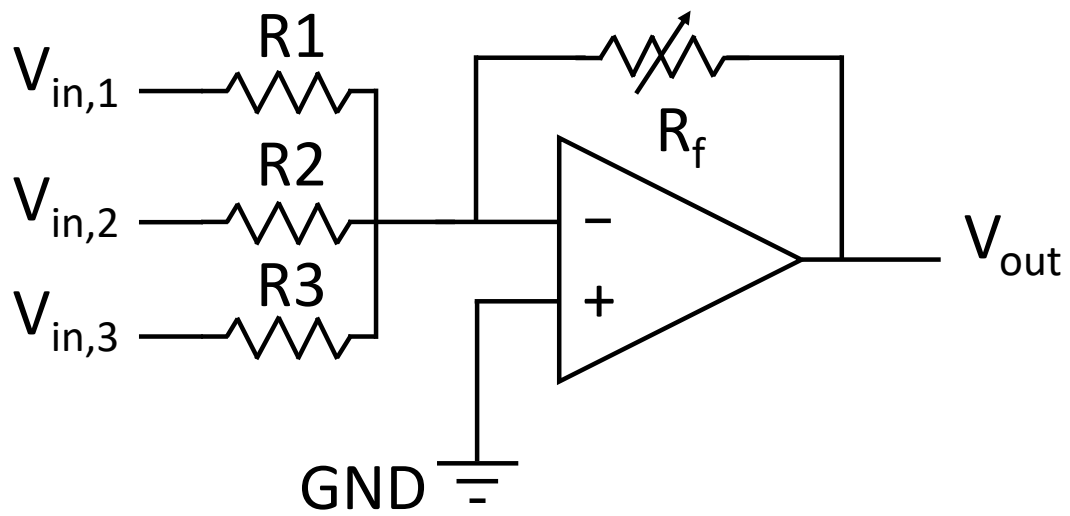


Fig. 4.9. Schematic of a summing amplifier. V_{out} can be determined as $V_{out} = -\frac{R_f}{R_1}[V_{in,1} + V_{in,2} + V_{in,3}]$ since we set $R1 = R2 = R3$. A potentiometer is used for R_f to control the amplitude of the signal.

tions ($300kHz$ $600kHz$). The two signals are safely superposed without conflicts. Fig. 4.9 shows the schematic configuration of the summing amplifier used in the circuit. The output signal (V_{out}) can be calculated as:

$$V_{out} = - \left[\frac{R_f}{R1} V_{in,1} + \frac{R_f}{R2} V_{in,2} + \frac{R_f}{R3} V_{in,3} \right]. \quad (4.4)$$

Here we set the resistance of R1, R2 and R3 to be the same. A potentiometer is used to adjust the amplitude of the added output signal.

4.4 Feedback cooling of a levitated nanoparticle

4.4.1 3D Feedback cooling of a levitated nanosphere

Unlike the nanodumbbells which have resolvable rotational degrees of freedom, spherical particles only have three translational degrees of freedom that needs to be considered with its symmetry. Before trying to cool five degrees of freedom of a levitated nanodumbbell, cooling all three directions of motion for a levitated nanosphere was performed. The hydraulic diameter of the levitated SiO_2 nanosphere (SS02N, Bangs Laboratories, Inc.) was determined to be 134 nm by substituting the measured damping rate to the equation [39]:

$$\Gamma_0 = \frac{6\pi\eta r}{M} \frac{0.619}{0.619 + Kn} (1 + c_K), \quad (4.5)$$

where η is the viscosity coefficient of air, r the radius of microsphere and Kn the Knudsen number. Note that $c_K = (0.31Kn)/(0.785 + 1.152Kn + Kn^2)$. The damping rate is proportional to the pressure at low pressures where $Kn \gg 1$ [96]. The measured damping rates ($\Gamma_0/2\pi$) for the 134 nm particle in x , y and z directions at different pressures are shown in Fig. 4.10.

The PSD under force feedback cooling can be determined from Eq. 4.3:

$$S_{fb}(\omega) = \frac{2k_B T_0}{M} \frac{\Gamma_0}{(\Omega^2 - \omega^2)^2 + \omega^2(\Gamma_0 + \Gamma_{fb})^2}, \quad (4.6)$$

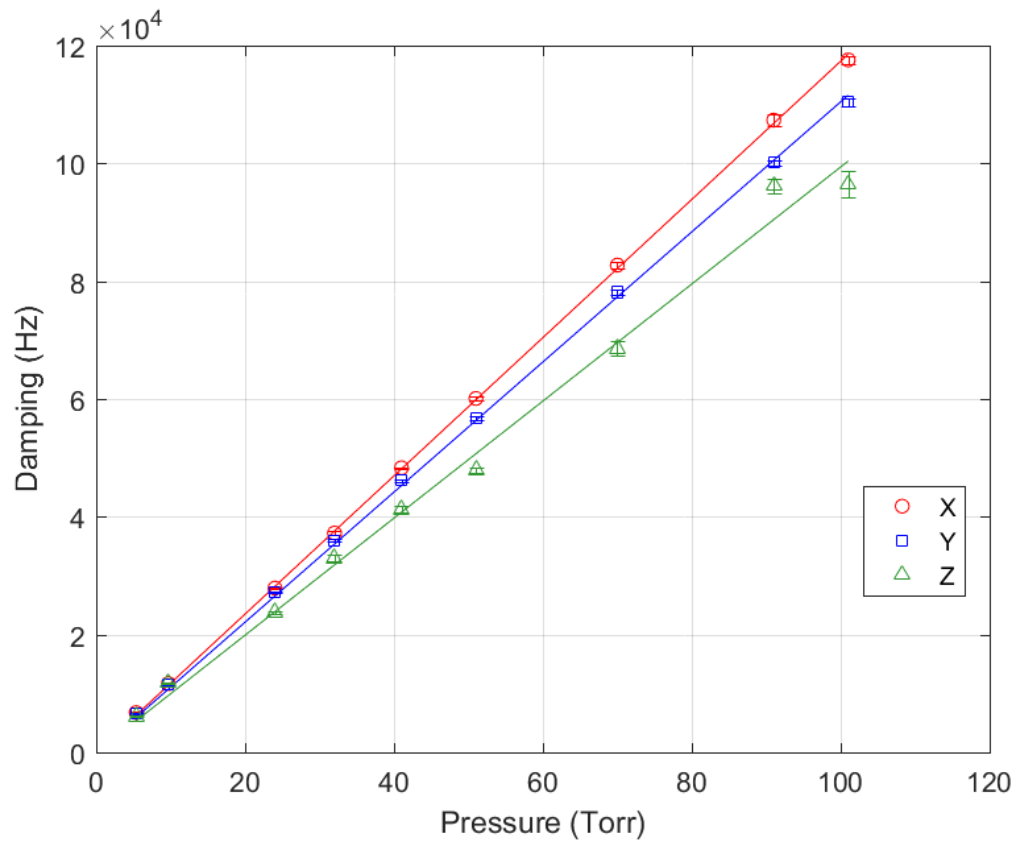


Fig. 4.10. Experimentally measured damping rates of a silica nanosphere at different pressures. Each data point is a mean of five measurements and the error bars indicate the standard deviations. The lines show linear fittings of the data sets for different directions.

where the external force due to the feedback laser can be expressed as $F_{cool} = -\Gamma_{fb}\dot{x}$. If we integrate both sides of Eq. 4.6 over ω we can get [110]:

$$\langle x^2 \rangle = \frac{k_B T_0}{M \Omega^2} \frac{\Gamma_0}{\Gamma_0 + \Gamma_{fb}}. \quad (4.7)$$

From the equipartition theorem we know that $M \Omega^2 \langle x^2 \rangle / 2 = k_B T / 2$. Thus, we can define the effective cooling temperature T_{fb} as [40, 96]:

$$T_{fb} = T_0 \frac{\Gamma_0}{\Gamma_0 + \Gamma_{fb}}. \quad (4.8)$$

From Eq. 4.6, we can notice that the damping rate increases as the effective temperature goes down. By substituting Eq. 4.8 to Eq. 4.6, we can obtain the expected PSD in the presence of feedback cooling which is:

$$S_{fb}(\omega) = \frac{2k_B T_{fb}}{M} \frac{\Gamma_{tot}}{(\Omega^2 - \omega^2)^2 + \omega^2 \Gamma_{tot}^2}, \quad (4.9)$$

where $\Gamma_{tot} = \Gamma_0 + \Gamma_{fb}$.

The result of 3D cooling is shown in Fig. 4.11, Fig. 4.12 and Fig. 4.13 which correspond to the power spectral densities of the translational motions in x , y and z directions respectively. The red PSD plots are taken at the pressure of 9.7 *Torr* and the cooling lasers were off. The blue PSD plots correspond to the case when the cooling lasers are applied at low pressure (6.0×10^{-4} *Torr*). In this experiment, since there is no need to cool the rotational degrees of freedom, the relative angle of polarization direction of the cooling laser does not have effect on the motion of the particle. The PSDs taken at 9.7 *Torr* (red PSD plots) can be safely regarded as the case when the particle is thermalized at room temperature (296.5 *K*). Thus, the PSDs can be fitted with the following equation:

$$S_{RT}(\omega) = a_0 T_{RT} \frac{\Gamma_0}{(\Omega^2 - \omega^2)^2 + \omega^2 \Gamma_0^2}, \quad (4.10)$$

where a_0 , Γ_0 and Ω are the fitting parameters. Here, we assume $T_{RT} = 296.5$ *K*. Note that $a_0 = \frac{2k_B}{M}$, where k_B is the Boltzmann constant and M is the mass of the particle. Therefore, once a_0 is retrieved from the fitting, it can be thought as a

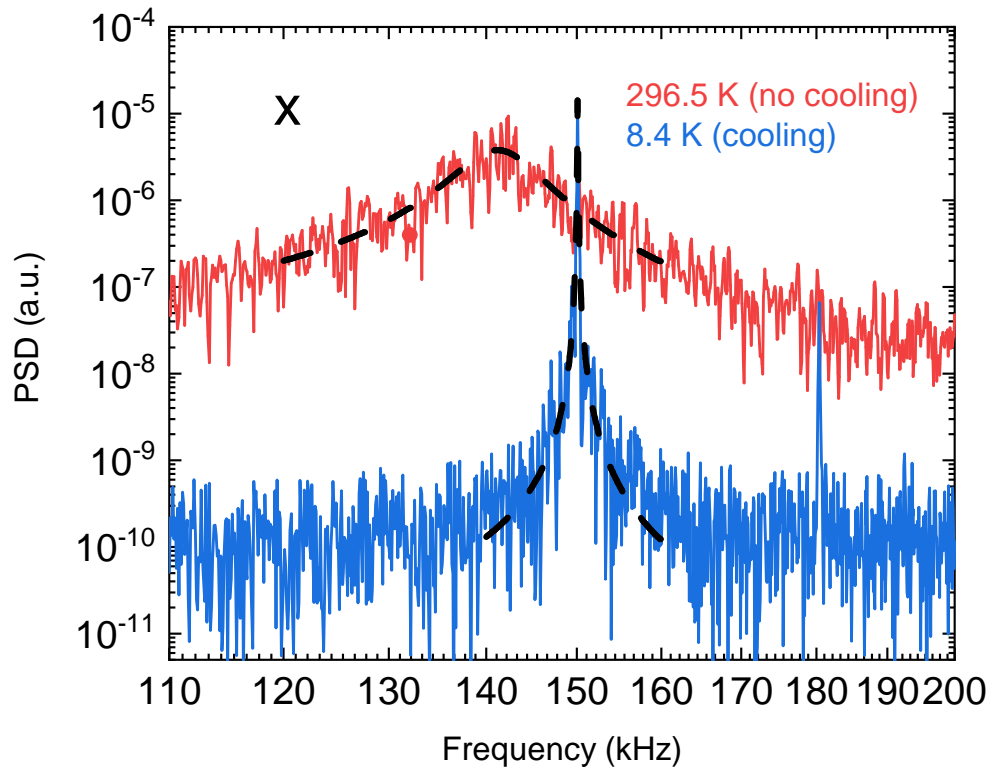


Fig. 4.11. Motional cooling of a levitated SiO_2 nanosphere in x direction. The PSD in red is the case when the feedback cooling is not applied to the system. The pressure at this moment was 9.7 Torr . The PSD in blue shows the case when feedback cooling is applied at low pressure ($6.0 \times 10^{-4} \text{ Torr}$). The black dashes represent the fitting for each PSDs.

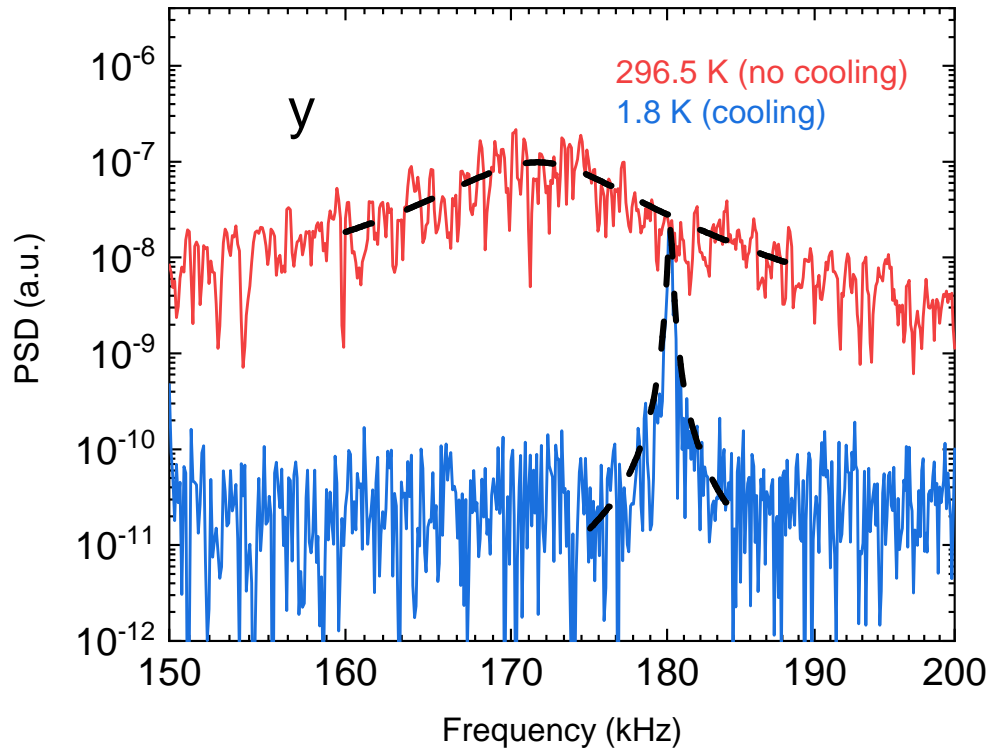


Fig. 4.12. Motional cooling of a levitated SiO_2 nanosphere in y direction. The PSD in red is when the feedback cooling is not applied to the system. The corresponding pressure is 9.7 Torr . The PSD in blue is the case when feedback cooling is applied at the pressure of $6.0 \times 10^{-4} \text{ Torr}$. The black dashes show the fitting for each PSDs.

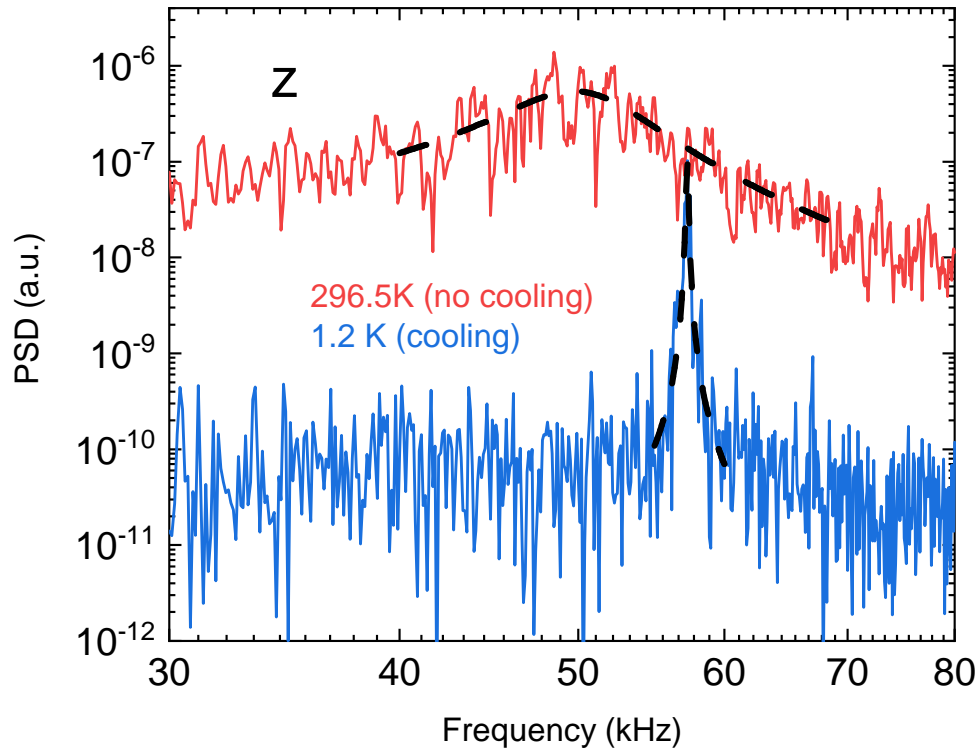


Fig. 4.13. Translational cooling of a levitated SiO_2 nanosphere in z direction. The red PSD shows when the feedback cooling is not applied at the pressure of 9.7 Torr . The PSD in blue is the case when feedback cooling is applied at the pressure of $6.0 \times 10^{-4} \text{ Torr}$. The black dashes show the fitting for each PSDs.

constant regardless of the frequency and damping rate. Using a_0 , we can determine the effective temperature T_{fb} by fitting the blue PSDs, which corresponds to the case when we have cooling lasers on at low pressure (6.0×10^{-4} Torr), with Eq. 4.9. The PSDs are obtained from 10 ms data set which is long enough considering the damping rates (which are usually around 100 Hz) for the blue PSDs. In this experiment, the motional temperature achieved for each direction x , y and z at the pressure of 6.0×10^{-4} Torr are 8.4 K, 1.8 K and 1.2 K respectively. Considering former experiments [39, 40], further cooling can be achieved when the vacuum reaches to a lower pressure. In our case however, the limiting pressure reachable is around 7×10^{-5} Torr which can be improved by adding different types of pumps (e.g. ion pumps) which are suitable to achieve high vacuum.

4.4.2 5D Feedback cooling of a levitated nanodumbbell

As discussed before, nonspherical particles are intrinsically asymmetric for certain degrees of freedom compared to spherical particles which requires additional cooling on expanded dimensions. In order to explore the possibility of cooling the rotational degrees of freedom, we demonstrated cooling of a levitated nanodumbbell in five degrees of freedom. The five degrees of freedoms include 3 translational DOFs (x , y and z) and 2 rotational DOFs (α and β). The results of 5D cooling of a levitated nanodumbbell are shown in Fig. 4.14, Fig. 4.15, Fig. 4.16, Fig. 4.17 and Fig. 4.18. Nanodumbbells consisting of two 120 nm-diameter spheres (SISN120, nanoComposix) are used in this experiment. Influences on the PSDs due to feedback cooling in each degree of freedom are plotted for different pressures. The c.m. motions of the nanodumbbell are cooled to few kelvin at 1.8×10^{-3} Torr in all three directions. On top of the translational cooling, the librational motion of the two torsional modes are also reduced by feedback cooling. Since both hybrid modes (ω_+ , ω_-) contribute to the torsional motions along α and β directions, we have to consider both peaks together to extract the motional temperature. The temperature of the librational

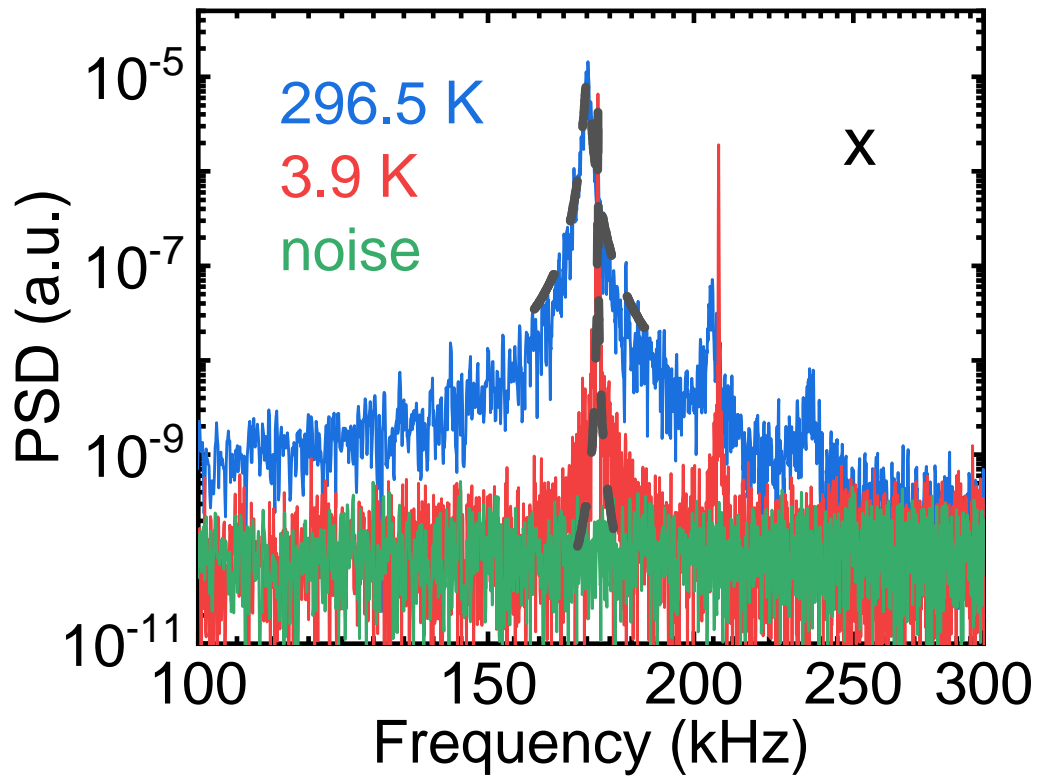


Fig. 4.14. Translational cooling of a levitated SiO_2 nanodumbbell in x direction. The blue PSD shows when feedback cooling is not applied at the pressure of 1 Torr . The PSD in red is the case when feedback cooling is applied at the pressure of $1.8 \times 10^{-3} \text{ Torr}$. The green PSD shows the noise level of the system when nothing is trapped. The black dashes show the fitting for each PSDs.

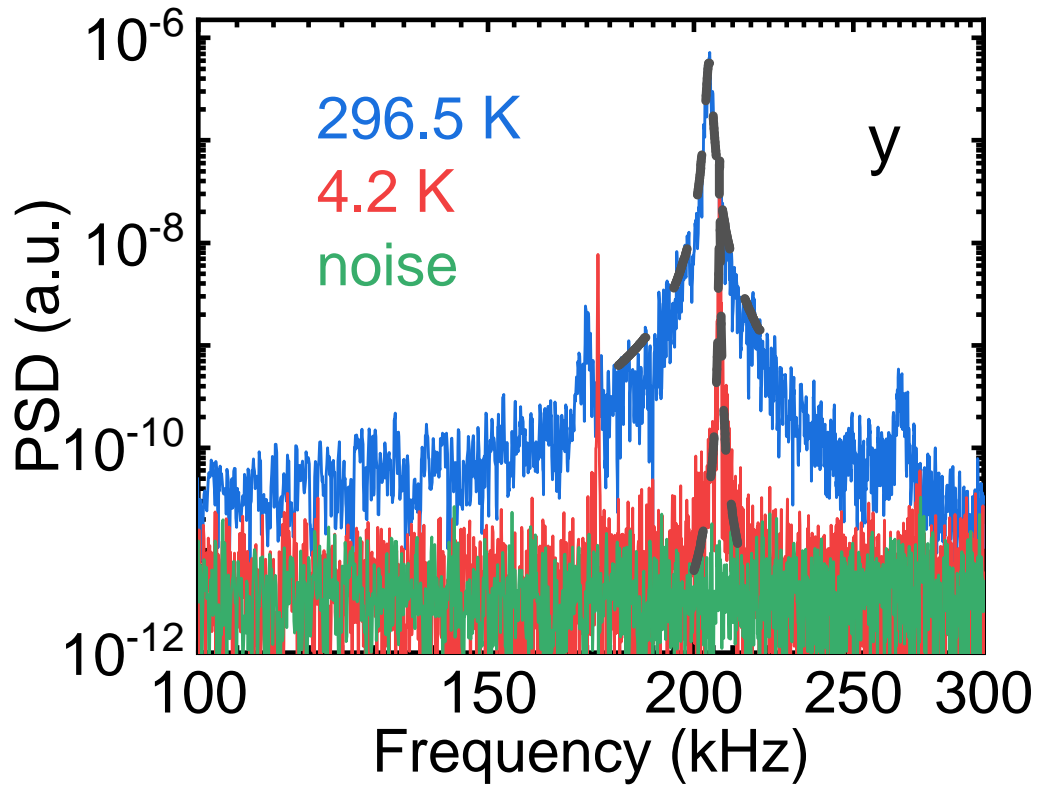


Fig. 4.15. Translational cooling of a levitated SiO_2 nanodumbbell in y direction. The blue PSD shows when feedback cooling is not applied at the pressure of 1 Torr . The PSD in red is the case when feedback cooling is applied at the pressure of $1.8 \times 10^{-3} \text{ Torr}$. The green PSD shows the noise level of the system when nothing is trapped. The black dashes show the fitting for each PSDs.

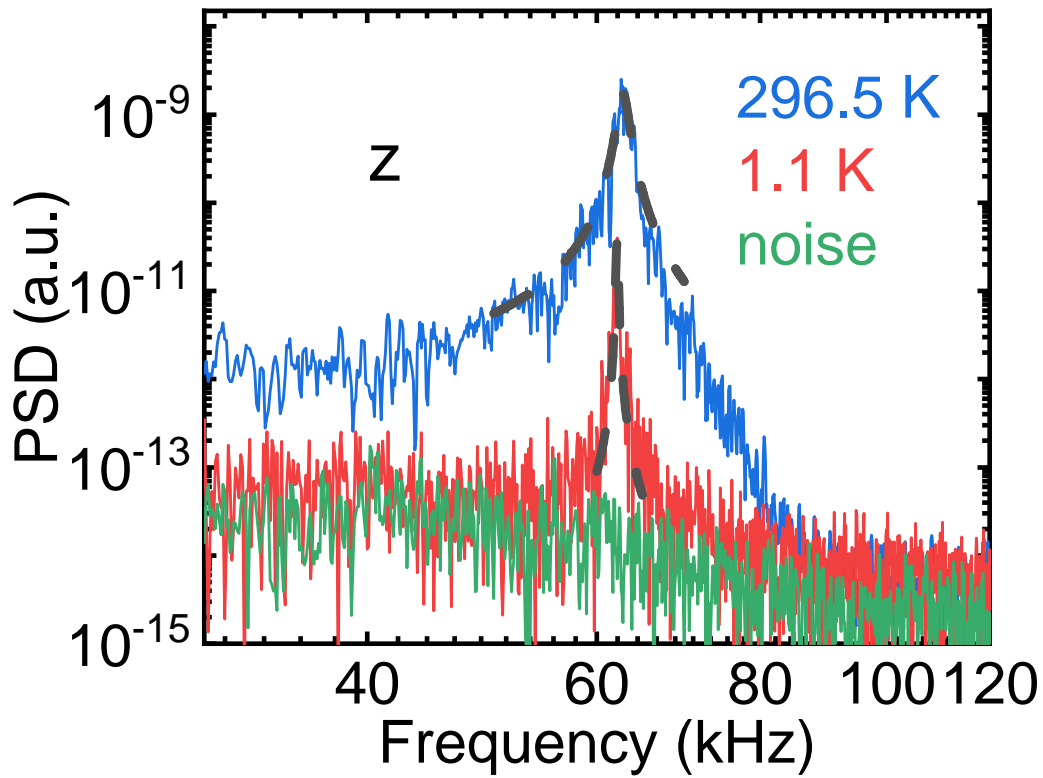


Fig. 4.16. Translational cooling of a levitated SiO_2 nanodumbbell in z direction. The blue PSD shows when feedback cooling is not applied at the pressure of 1 Torr. The PSD in red is the case when feedback cooling is applied at the pressure of 1.8×10^{-3} Torr. The green PSD shows the noise level of the system when nothing is trapped. The black dashes show the fitting for each PSDs.

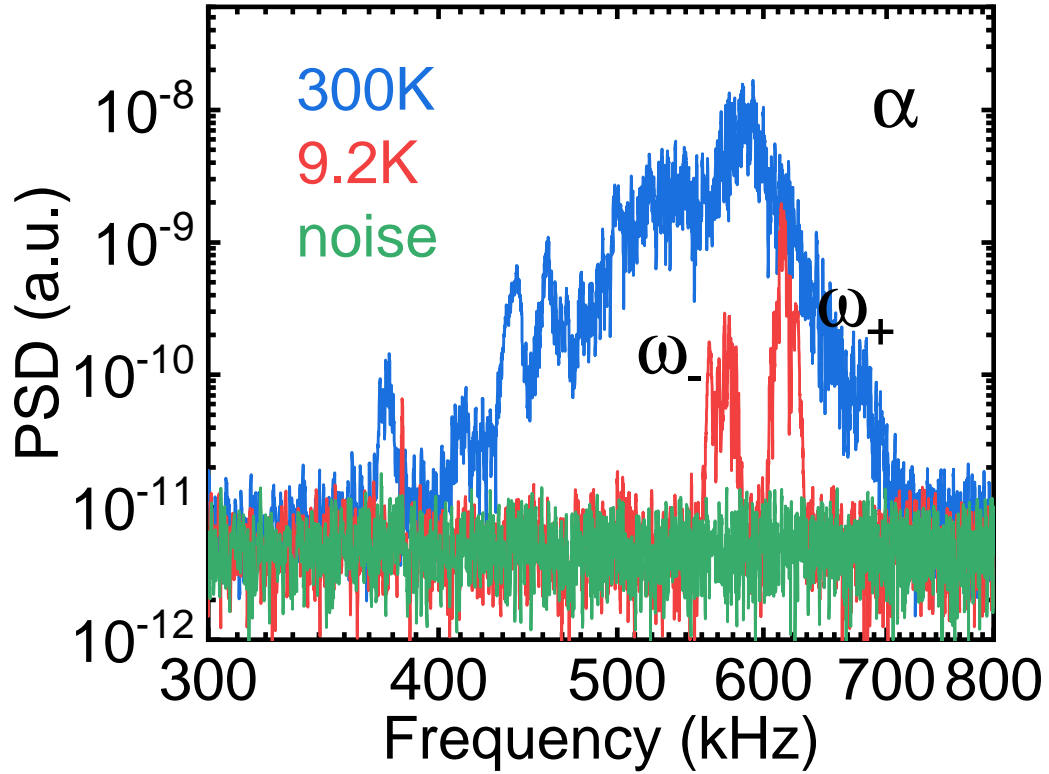


Fig. 4.17. Torsional cooling of a levitated SiO_2 nanodumbbell in α direction. The blue PSD shows when feedback cooling is not applied at the pressure of 1 Torr. The PSD in red is the case when feedback cooling is applied at the pressure of 1.8×10^{-3} Torr. The green PSD shows the noise level of the system when nothing is trapped. The black dashes show the fitting for each PSDs.

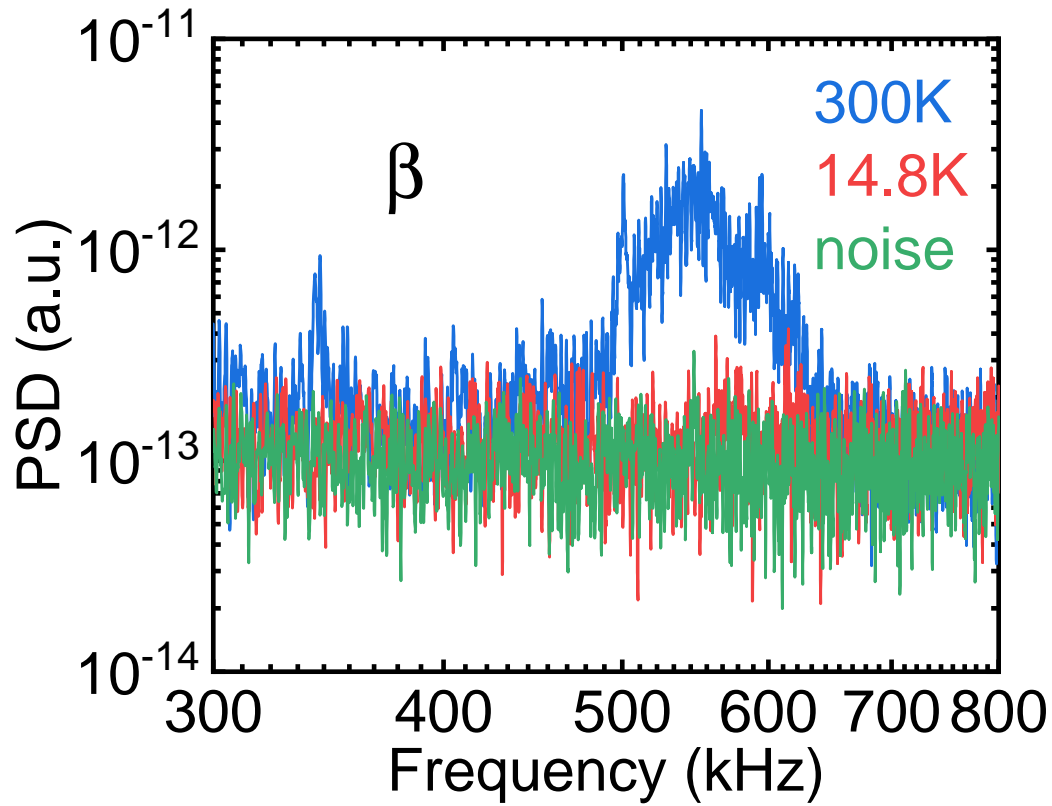


Fig. 4.18. Torsional cooling of a levitated SiO_2 nanodumbbell in β direction. The blue PSD shows when feedback cooling is not applied at the pressure of 1 Torr. The PSD in red is the case when feedback cooling is applied at the pressure of 1.8×10^{-3} Torr. The green PSD shows the noise level of the system when nothing is trapped. The black dashes show the fitting for each PSDs.

motions are estimated roughly from the underlying area of the PSD. Note that the noise floor was subtracted when calculating the temperature. The lowest effective temperatures achieved for the two torsional DOFs are 9.2 K (α) and 14.8 K (β) respectively. Currently, the temperature of β motion is mainly limited by the low signal-to-noise ratio of the β signal obtained from the x detector. In fact, the PSD of the cooled β vibration is close to its noise level (Fig. 4.18). In order to collect the signal from β direction with higher efficiency, installing another probing laser along the y axis could be a solution. To our best knowledge, this is the first report on 5D cooling of a levitated nanoparticle. The nanodumbbell has six motional degrees of freedom in total. The uncooled DOF, which is the spin motion (γ), does not directly interact with the laser because of the symmetry of the nanodumbbell.

4.5 Conclusion

In conclusion, demonstration of 5D cooling of a levitated nanodumbbell was discussed in this chapter. Details about 5D cooling of a levitated nanodumbbell by developing an active force and torque feedback cooling method was presented. Active force feedback cooling was realized by utilizing the radiation pressure of additional cooling lasers shot to the trapped particles. A home-built analog differential circuit was used to generate the cooling signal and the signals were fed in to three AOMs to control the power of each cooling lasers. Torsional cooling was realized by tilting the polarization angle of cooling lasers with respect to the trapping laser. This twist provided additional torque on the particle enabling cooling of its torsional motion. The only uncooled degree of freedom is the spin around its symmetric axis which has no direct interaction with the trapping laser. Our work is also relevant to cooling of other nonspherical particles, such as nanorods, microdisks and mirrors for exploring new physics [93, 94].

5. ROTATION COUPLED NONLINEAR MOTION

5.1 Motivation

Thanks to the extremely small mass of a levitated nanosphere, it has been proven that even the thermal energy is sufficient to drive the c.m. motion of the levitated nanosphere into the nonlinear regime as we go to vacuum [111]. This phenomena is not limited to a spherical particle but also applies to a non-spherical particle like nanodumbbells. Moreover, by simply comparing the shape of potential (Fig. 3.7) it can be assumed that in the case of torsional motions, the nonlinear characteristics will be even stronger than the c.m. motions. This is because while the potential distribution of a c.m. motion could be estimated as Gaussian, where the bottom of the potential is often assumed as a parabola, the potential shape of the torsional motion follows a sinusoidal function. Not only that, the depth of the potential is much shallower in the case of torsional motion which implies less energy is required to drive the motion to a nonlinear regime. Recently, nonlinear systems have drawn more attention by utilizing the intrinsic nonlinearity, practical functionalities such as frequency-tuning [112, 113] or resonance bandwidth expansion [114–116]. Not only that, strong nonlinearities can be potentially useful for generating nonclassical phonon states [33, 117]. Levitated phonon laser by exciting the c.m. motion already has been demonstrated [78].

In this chapter, we investigate the nonlinear characteristics of the torsional motion in more detail. From the measured PSDs of a levitated nanodumbbell (Fig. 3.8), we immediately notice that the torsional peaks (α and β) around 350 kHz are much broader than their expected linear linewidths in vacuum. To have a better understanding of these unexpected feature of spectrum as well as the real situation, we analyze the motion of the particle in both theory and experiment. On top of the non-

linearity coming from the sinusoidal potential, we also provide an explanation of a phenomenon which we call rotation coupling that further affects the torsional motion. The detailed analysis allows us to thoroughly understand the complex double peak of the torsional motions appeared in the PSDs and the real motion of the particle inside the optical trap.

5.2 Experimental description

In this experiment, nanodumbbells consisting of two 170 *nm*-diameter spheres (SS02N, Bangs Laboratories, Inc.) are used to study the nonlinear torsional dynamics. As the size of the particle increases, the motional signal also increases since the amount of scattering light increases. Thus, having a larger particle is advantageous in this case where we want to retrieve as much motional information as possible. The basic experimental setup is the same as the previous experiment where a nanodumbbell (with two 120 *nm*-diameter naonspheres) was cooled down in 5 degrees of freedom. In this chapter however, we apply feedback cooling only on the c.m. motions of the trapped nanodumbbell so the nonlinearity caused by the thermal c.m. motion can be significantly suppressed. This helps us to effectively investigate the characteristics of torsional motions in vacuum without having too much complexity.

5.3 Nonlinearity of torsional motion and rotation coupling

Now, we investigate the nonlinear characteristics of the torsional motion. The trapping potential of a c.m. motion for optical tweezers can be approximately expressed as a Gaussian function. It is important to understand that even though the bottom of a Gaussian potential can be approximated as a quadratic function (thus a harmonic potential), soon the nonlinearity rises as the trapped particle travels further away from the center. As a consequence, this causes a nonlinear motion in the translational degree of freedom for a trapped nanoparticle in vacuum [111,118]. In case of the torsional vibration, the nonlinearity is much stronger because the potential

$U(\alpha, \beta, x, y, z)$ is sinusoidally dependent on α and β (Fig. 3.7). The trapping depth of the rotational confinement is also much shallower than that of the c.m. confinements (Fig. 3.7).

We introduce $\xi = \alpha$, $\eta = \frac{\pi}{2} - \beta$ as small deviation of angles from the equilibrium orientation. If ξ and η are small enough, it becomes possible to approximate the system as a Duffing nonlinear oscillator. The force and torque can be determined from Eq. (3.1) as:

$$\begin{aligned}
F_x &\approx -k_x x \left[1 - \frac{\alpha_{\parallel} - \alpha_{\perp}}{\alpha_{\parallel}} (\xi^2 + \eta^2) - 2 \left(\frac{x^2}{\omega_x^2} + \frac{y^2}{\omega_y^2} + \frac{z^2}{z_0^2} \right) \right], \\
F_y &\approx -k_y y \left[1 - \frac{\alpha_{\parallel} - \alpha_{\perp}}{\alpha_{\parallel}} (\xi^2 + \eta^2) - 2 \left(\frac{x^2}{\omega_x^2} + \frac{y^2}{\omega_y^2} + \frac{z^2}{z_0^2} \right) \right], \\
F_z &\approx -k_z z \left[1 - \frac{\alpha_{\parallel} - \alpha_{\perp}}{\alpha_{\parallel}} (\xi^2 + \eta^2) - 2 \left(\frac{2x^2}{\omega_x^2} + \frac{2y^2}{\omega_y^2} + \frac{z^2}{z_0^2} \right) \right], \\
T_{\xi} &\approx -k_{\xi} \xi \left[1 - \frac{2}{3} \xi^2 - \eta^2 - 2 \left(\frac{x^2}{\omega_x^2} + \frac{y^2}{\omega_y^2} + \frac{z^2}{z_0^2} \right) \right], \\
T_{\eta} &\approx -k_{\eta} \eta \left[1 - \frac{2}{3} \eta^2 - \xi^2 - 2 \left(\frac{x^2}{\omega_x^2} + \frac{y^2}{\omega_y^2} + \frac{z^2}{z_0^2} \right) \right].
\end{aligned} \tag{5.1}$$

In our experiment, the translational motions x , y and z of the nanodumbbell are cooled using feedback cooling to keep the particle at low pressure and only focus on the effect of torsional nonlinearities. Therefore, it becomes possible to ignore the effects of the translational motions from the above equations [111]. The nonlinear c.m. motion frequencies (ω_{x_i} , $x_i = x, y, z$) and torsional frequencies ($\omega_{\xi}, \omega_{\eta}$) due to the torsional motions can be expressed as:

$$\begin{aligned}
\omega_{x_i}^2 &= \omega_{x_i,0}^2 \left[1 - \frac{\alpha_{\parallel} - \alpha_{\perp}}{\alpha_{\parallel}} (\xi^2 + \eta^2) \right], \\
\omega_{\xi}^2 &= \omega_{\xi,0}^2 \left(1 - \frac{2}{3} \xi^2 - \eta^2 \right), \\
\omega_{\eta}^2 &= \omega_{\eta,0}^2 \left(1 - \xi^2 - \frac{2}{3} \eta^2 \right).
\end{aligned} \tag{5.2}$$

Here, $\omega_{x_i,0}$, $\omega_{\xi,0}$ and $\omega_{\eta,0}$ are the intrinsic trapping frequencies when the vibration amplitudes are zero. Therefore, based on Eq. (5.2), a finite-amplitude vibration in any direction will decrease the frequencies of oscillations simultaneously in all directions. This leads to a conclusion that the frequency fluctuations has to be positively

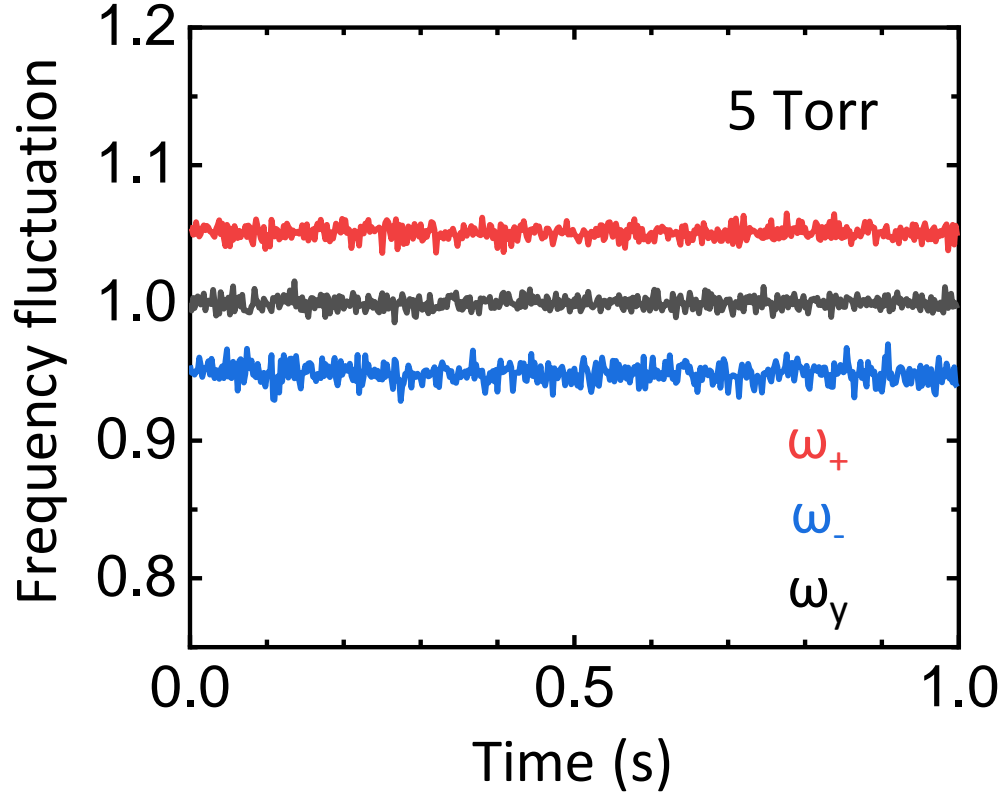


Fig. 5.1. Relative frequency fluctuations of the two torsional hybrid modes ω_+ (red) and ω_- (blue) are shown in comparison with the c.m. motion in y direction (grey) at the pressure of 5 Torr. The frequency for each data points are determined from a 2 ms signal data. The frequency of the two torsional hybrid modes are normalized by the average of the two ($\frac{\omega_+ + \omega_-}{2}$) and the c.m. motion is normalized by the average of itself.

correlated for all modes including both c.m. motions and torsional vibrations. For levitated nanoparticles, the strong correlation of frequency change between different dimensions is a good evidence of nonlinearity [111]. The measured frequency fluctuations are presented in Fig. 5.1, Fig. 5.2 and Fig. 5.3.

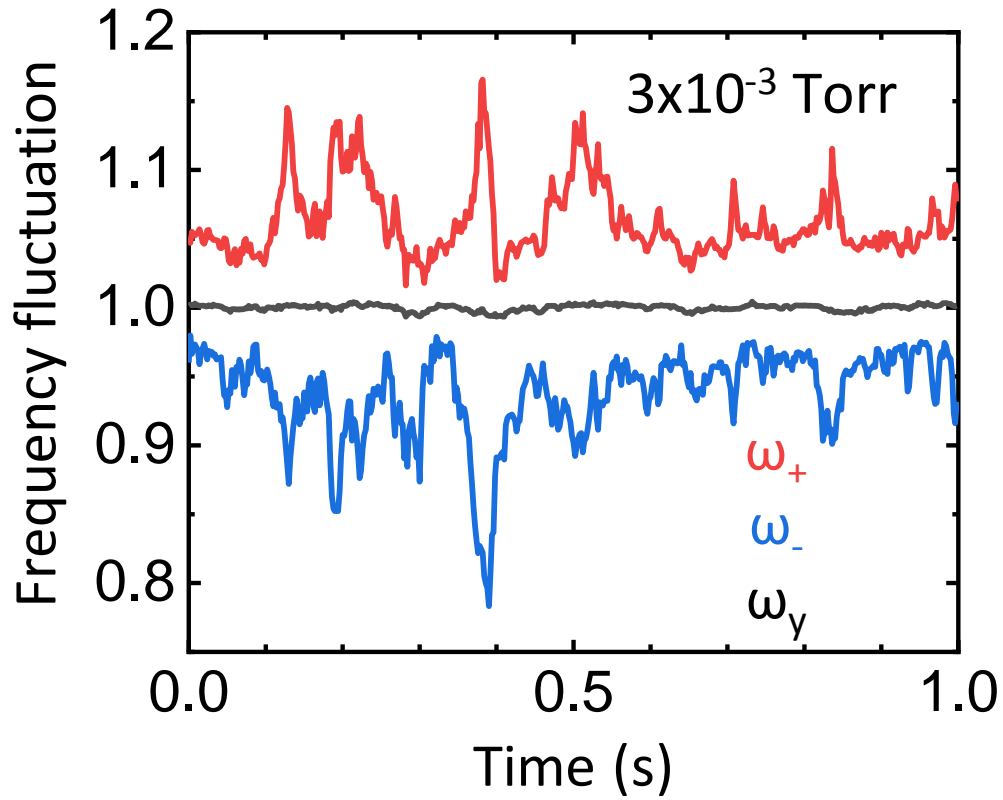


Fig. 5.2. Relative frequency fluctuations of the two torsional hybrid modes ω_+ (red) and ω_- (blue). Grey shows the c.m. motion along y -direction. The data was taken at the pressure of $3.33 \times 10^{-3} \text{ Torr}$. The frequency for each points are determined from a 2 ms signal data. As in Fig. 5.1, the frequency of the two torsional hybrid modes are normalized by the average of the two ($\frac{\omega_+ + \omega_-}{2}$) and the c.m. motion is normalized by the average of itself.

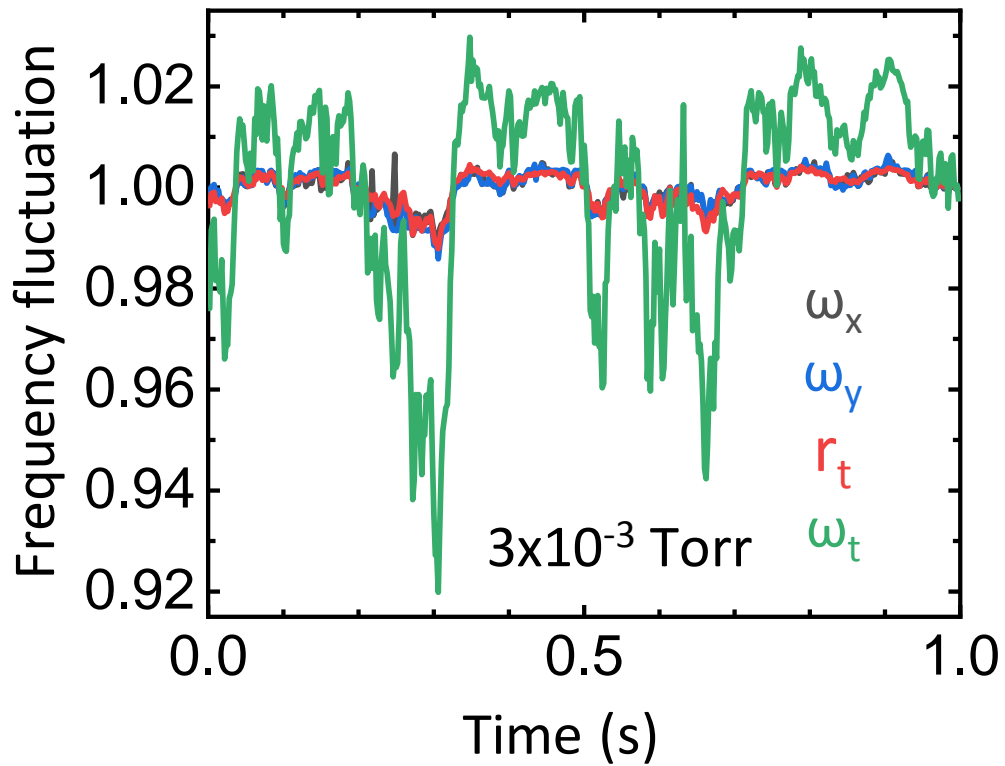


Fig. 5.3. Relative frequency fluctuations for translational motions and torsional motions at $3.33 \times 10^{-3} \text{ Torr}$. The black curve indicates the frequency fluctuation of x -direction and the blue curve shows the frequency fluctuation of y -direction. The characteristic frequency fluctuation for α -direction is shown in green. The red plot shows the scaled frequency change for ω_t based on the scaling factor retrieved from eq. 5.2.

When the pressure is relatively high (5 *Torr*), frequency fluctuations of each modes are small because of the high damping rate (Fig. 5.1). However, when the pressure is lowered, the rarefied surrounding gas no longer provides enough damping resulting in a large fluctuation of the oscillation frequency for every direction. Note that the damping rate also reduces as the pressure is lowered. Therefore, the measurement time (2 *ms*) becomes short enough to capture the fluctuation. As shown in Fig. 5.2, the thermal noise causes large frequency fluctuations of the two hybrid modes caused by the nonlinearity.

Besides the large frequency fluctuations, another consequence of nonlinearity is the strong correlation of frequency fluctuations in different modes as stated before. As expected from Eq. (5.2), the relative fluctuations in c.m. frequencies $\omega_{x_i}/\langle\omega_{x_i}\rangle$ at 3×10^{-3} *Torr* are positively correlated (Fig. 5.4). The correlation of the normalized c.m. motion frequency fluctuations ($\omega_x \star \omega_y$) becomes close to one (0.93 ± 0.02 at 3×10^{-3} *Torr*) as the pressure decreases (Fig. 5.4). This result is similar to the case for a levitated single nanosphere [111].

To further test Eq. (5.2), especially the nonlinear characteristic of torsional motions, we introduce another torsional frequency $\omega_t \equiv \sqrt{(\omega_\xi^2 + \omega_\eta^2)/2}$, and its adjusted relative fluctuation $r_t = 1 + \frac{6}{5} \frac{\alpha_\parallel - \alpha_\perp}{\alpha_\parallel} (\frac{\omega_t}{\langle\omega_t\rangle} - 1)$. The newly introduced torsional frequency (ω_t) retrieves the pristine frequency change of the torsional mode (in α -direction for this case) due to the thermal fluctuation. Thus, ω_t is expected to have similar correlation with other degrees of freedom. For a nanodumbbell with an aspect ratio of 1.9, we know that $\frac{\alpha_\parallel - \alpha_\perp}{\alpha_\parallel} = 0.126$ from our previous works on levitated nanodumbbells [53]. The adjusted relative frequency fluctuation r_t is plotted on top of the fluctuations in c.m. motion frequencies (Fig. 5.3). It can be immediately seen that r_t overlaps with $\omega_{x_i}/\langle\omega_{x_i}\rangle$ very well, which agrees with Eq. (5.2). Indeed the correlation reaches close to one for ($\omega_x \star \omega_t$) (Fig. 5.4). Another important aspect is the considerably larger frequency fluctuation of ω_t compared to that of the c.m. motion frequencies in Fig. 5.3. This is a direct confirmation that the torsional degree

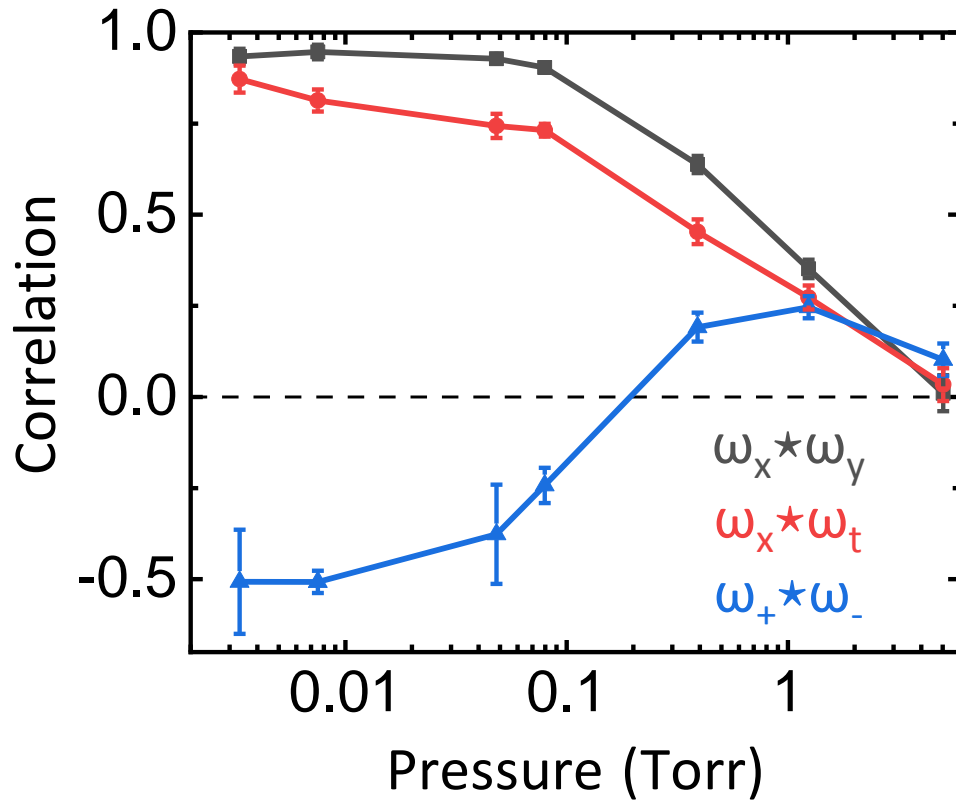


Fig. 5.4. Frequency correlations between different degree of freedoms. The correlations between different modes are plotted as a function of pressure. Each data point corresponds to an average of correlation for five sets of measurement. For each measurement, correlation is calculated from 500 PSDs. The error bar shows the standard deviation of the data set.

of freedom experiences stronger intrinsic nonlinearity than the translational degree of freedom.

5.4 Rotation coupled torsional motion

At the early stage of this project, we expected the two torsional motions to be nicely decoupled to the other degrees of freedom so that each torsional motion acts as an individual oscillator around its axis of confinement. Counter-intuitively, we found that the thermal Brownian rotation of the nanodumbbell around its symmetric axis strongly affects its torsional vibrations, even though the rotation is irrelevant to the trapping laser. Therefore, without considering the effect of rotation coupling, Eq. (5.2) can not explain the full picture of the measured torsional power spectral densities. For instance, the measured torsional power spectral densities have two peaks for both α and β motions (Fig. 3.8). Moreover from Fig. 5.4, it can be seen that the frequencies of these two peaks (ω_+ , ω_-) are negatively correlated at low pressure. These phenomena can not be explained by Eq. (5.2). The discrepancy comes from the fact that Eq. (5.2) does not consider the free Brownian rotation of the nanodumbbell around its symmetric axis. Nevertheless, the random rotation will couple the two torsional modes as [89]:

$$\begin{aligned}\ddot{\xi} &= -\omega_\xi^2 \xi - \omega_c \dot{\eta}, \\ \ddot{\eta} &= -\omega_\eta^2 \eta + \omega_c \dot{\xi}.\end{aligned}\tag{5.3}$$

Here, $\omega_c = (I_z/I_x)\omega_\gamma$ and ω_γ is the frequency of rotation around its symmetric axis. The solutions for ξ and η of Eq. (5.3) have two normal modes ω_+ and ω_- which can be interpreted as clockwise and counterclockwise precession modes. They can be understood as hybrid modes of the original torsional motions. The two hybrid modes can be determined as:

$$\omega_\pm = \frac{1}{\sqrt{2}} \left[2\omega_t^2 + \omega_c^2 \pm \sqrt{4\omega_t^2\omega_c^2 + \omega_c^4 + \Delta^4} \right]^{\frac{1}{2}}, \tag{5.4}$$

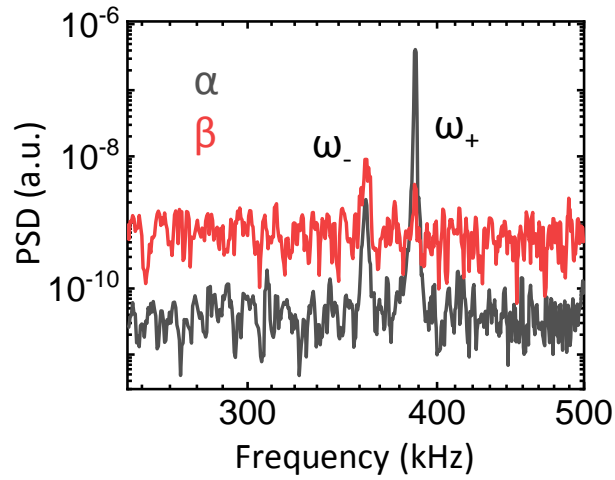
where $\Delta^2 = \omega_\xi^2 - \omega_\eta^2$. If $\Delta^4 \ll 4\omega_t^4$, which is indeed the case in our experiment, ω_t becomes $\omega_t = \sqrt{\omega_+\omega_-}$. Eq. (5.4) is used to calculate ω_t shown in Fig. 5.3. As it can

be seen from Eq. (5.4), ω_+ and ω_- change oppositely when ω_c changes. Therefore, due to the rotational fluctuation of the nanodumbbell, the two torsional peaks are moving in the opposite direction as in Fig. 5.2. The effect of rotational coupling competes with the thermal nonlinear effect (Eq. (5.2)) and finally becomes superior as the pressure is lowered. As a result, the correlation between the frequencies of the two hybrid modes $\omega_+ \star \omega_-$ becomes negative in high vacuum (Fig. 5.4).

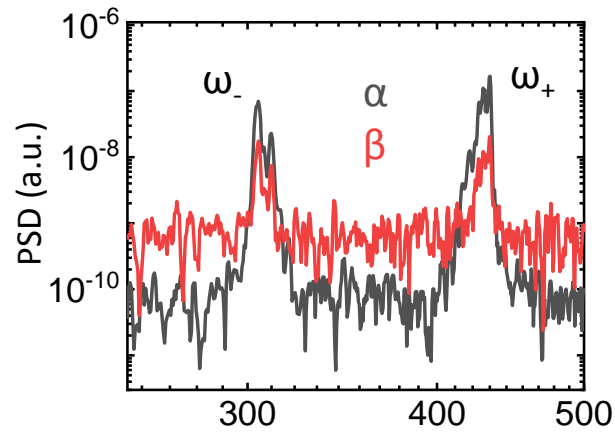
In order to confirm the behavior of the hybrid modes as well as to investigate the nature of complicated rigid-body rotation of a levitated nanodumbbell, we compare the experimental findings with numerical simulations. Simulation and experimental results of the power spectral densities of the two hybrid modes are shown in Fig. 5.5 and Fig. 5.6. As shown in the PSDs, the frequencies of the two hybrid modes ω_+ and ω_- becomes closer as the coupling frequency (ω_c) gets slower. Note that ω_c is determined from the geometry of the particle (I_z/I_x) and the rotational frequency ω_γ of the particle around its symmetry axis. This observation indicates that even though the rotation of the nanodumbbell does not directly interact with the trapping laser due to its symmetry, its angular velocity (ω_γ) can be observed in time by tracing the separation of the frequencies of the two hybrid modes. This finding potentially opens up the possibility to access to the “invisible” 6th degree of freedom without additional probing skims.

5.5 Conclusion

To conclude this chapter, investigation of the complex torsional nonlinear dynamics of a levitated nanodumbbell was performed. The motivation of this work came from the aspiration to understand the eccentric shape of the torsional PSDs. Compared to the PSDs of c.m. motions, the torsional PSDs were much broader and complex. In torsional motions, it turned out that the broad two peaks in the PSDs are resulted by two distinct factors: 1) nonlinearity and 2) rotation coupling. The large thermal nonlinearity of the torsional motion could be advantageous for various

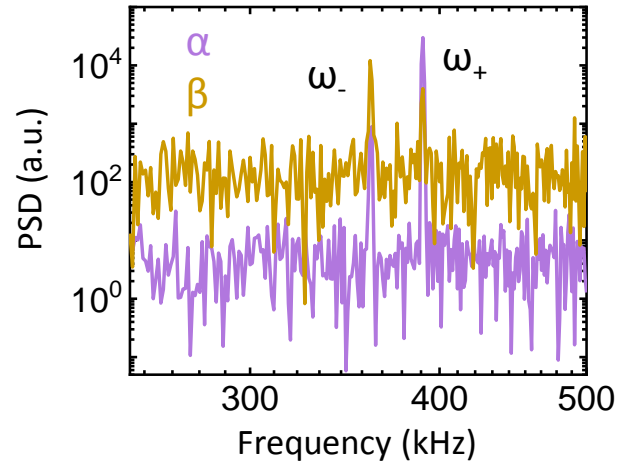


(a) Measured power spectral densities of torsional motions in α (grey) and β (red) directions when the frequency of rotation ω_c is small.

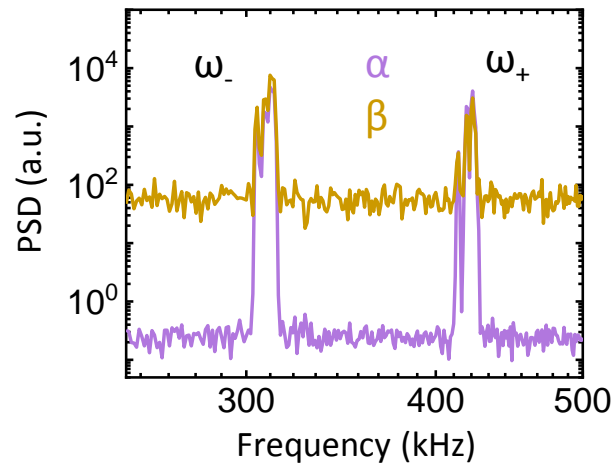


(b) Measured PSDs of torsional motions in α (grey) and β (red) directions when the frequency of rotation ω_c is large.

Fig. 5.5. Experimental results of rotation coupled torsional motions in α (grey) and β (red) directions. The PSDs are taken at 3×10^{-3} Torr and the measurement time is 2 ms.



(a) Simulated PSDs of torsional motions in α (purple) and β (yellow) directions when the frequency of rotation $\omega_c/2\pi$ is 17 kHz (small).



(b) Simulated PSDs of torsional motions in α (purple) and β (yellow) directions when the frequency of rotation $\omega_c/2\pi$ is 115 kHz (large).

Fig. 5.6. Simulation results of rotation coupled torsional motions in α (purple) and β (yellow) directions. The simulated time of motion is 1 ms and random noise is added to the background to mimic the experimental situation.

situations like nonlinear sensing or the creation of non-classical states [33, 117, 119]. We successively observed the coupling of this rotational DOF to the torsional motions by monitoring the relative frequency difference of the two hybrid modes (ω_+ and ω_-). Therefore, it became possible to observe the angular frequency of the nanodumbbell's rotation even though the rotation itself can not be directly observed. This finding paves a way to a full 6D detection of a levitated nanodumbbell. Moreover, this work helps us to have a better understanding about the dynamics of a levitated nonspherical particle involving the complex rigid-body motion.

6. FUTURE WORK

6.1 Improving motional cooling

Even though 5D cooling of a levitated nanodumbbell was performed using an optical tweezer in this dissertation, the motional temperatures of the particle are not sufficient for it to be used as a novel platform for advanced research and technology. The inherent yet critical obstacle to overcome is the rotation coupled torsional motion. Due to the coupling from the free Brownian rotation, the torsional motion evolves to two hybrid modes instead of having one normal mode for each directions. Moreover, the frequency of the two hybrid modes keep changing depending on the rotation speed (ω_γ). Eventually, it becomes extremely difficult to provide a right feedback signal to counter act the particle's motion. One possibility to resolve this problem could be using cavity cooling instead of active feedback cooling. Cavity cooling can be thought as more automated in a sense that when the cavity mirrors are positioned with the right distance, the energy of the targeted mode naturally flows in to the optical cavity mode to overcome the detuning [32]. Cavity cooling of translational motions of a levitated nanodumbbell already reach to a motional ground state in room temperature [43]. Thus, it could be a valuable approach to test torsional motion cooling by cavity cooling.

6.2 Engineering of a levitated particle

In order to critically achieve the motional cooling of a levitated particle, cooling in all dimensions is necessary. Even though the nanodumbbells have great uniqueness compared to a single particle without having extensive complexities for analysis, the rotational degree of freedom in the γ -direction is inaccessible in our system due to its

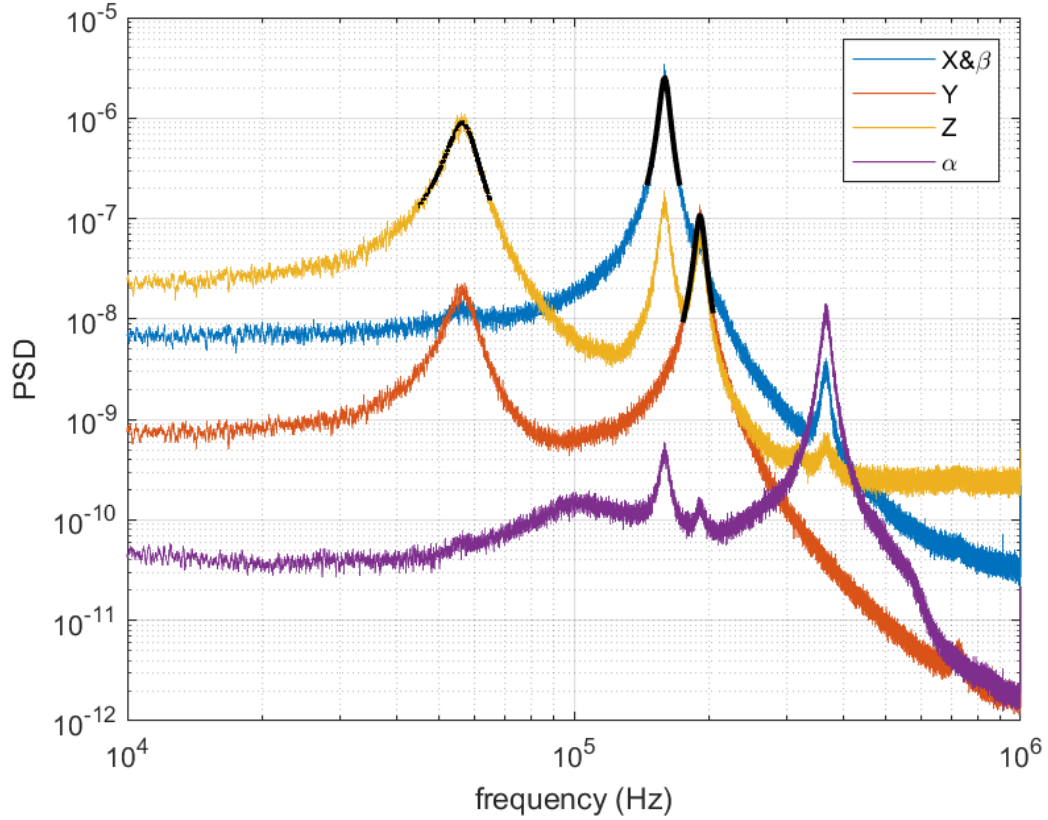


Fig. 6.1. Power spectral densities of a levitated nano trimer. PSDs of each direction are plotted in blue (x & β), orange (y), yellow (z) and purple (α). Black curve shows the fitting for x , y and z . The signal for the PSD is taken for 1 s .

symmetry. A careful design of a levitated particle such as an nano elliptic mirror might be a good candidate to solve the problem [30,94]. In order to explore the possibilities of levitating a disk like particle, we trapped a trimer in a triangle configuration. The damping rate ratio turned out to be $\Gamma_y/\Gamma_x = 1.15$ and $\Gamma_z/\Gamma_x = 1.04$ confirming that the particle is a triangular trimer (Fig. 3.9). We believe that the face of the particle is aligned parallel to the propagating direction of the trapping laser (z -direction) to minimize its potential. Fig. 6.2 shows a preliminary result of torsional motion cooling of a levitated triangle trimer. The shown PSD is for the α -direction of the

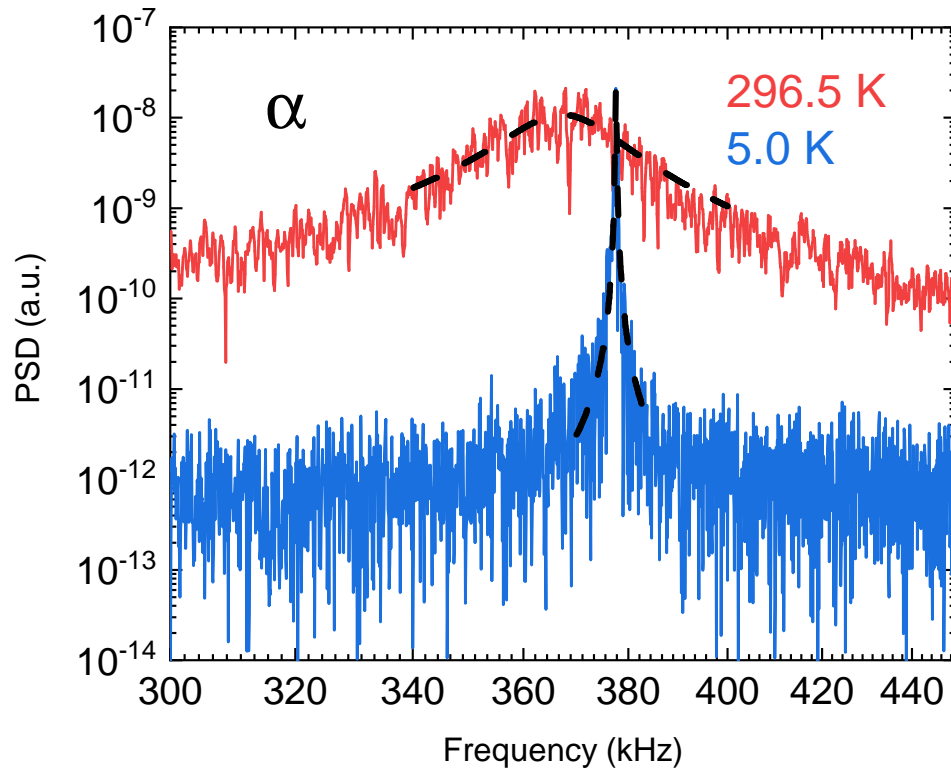


Fig. 6.2. Torsional cooling of a levitated trimer. PSDs of a torsional motion in α -direction are plotted for a situations without cooling at 10 Torr (red) and with cooling at 1.7×10^{-3} Torr (blue). The black dashed lines show the Lorentzian fitting.

particle. Note that the PSD can be fitted with Lorentzian curves. This implies that the motional degree of freedom is well decoupled because of its asymmetric geometry. The torsional vibration could be easily cooled down to few kelvins at around 1.7×10^{-3} Torr. Even though eventually the particle starts to rotate in high vacuum because of the weak confinement for the β -direction (since three particles are in triangular configuration), it could be overcome by intentionally increase the long axis for an elliptical disk.

6.3 On-chip optical tweezer

Besides the exceptional capability of a levitated optomechanical system as a tool for precision measurement, the possibility for the system to be adapted in real life is still far-fetched. The main reason is because of the size of the overall system. Leaving the size of the laser aside, the optical tweezer configuration including the vacuum chamber is too bulky to apply to most existing technologies requiring sensors. This fact is a huge disadvantage for the field of levitated optomechanics to gather the spot light. Efforts have been made to use optical fibers to trap particles [120] or integrate plasmonic structures [121,122] to overcome the shortcoming. Though these researches successfully explored new possibilities to reduce the size of the system, they are still not genuine enough to be called as an on-chip optical tweezer. Designing an on-chip optical tweezer with a conventional fabrication technique will be highly beneficial for the whole field to be appreciated to the engineering society and will derive new research and products in both academia and industrial society.

REFERENCES

REFERENCES

- [1] A. Ashkin, “Acceleration and trapping of particles by radiation pressure,” *Physical review letters*, vol. 24, no. 4, p. 156, 1970.
- [2] K. Svoboda and S. M. Block, “Optical trapping of metallic rayleigh particles,” *Optics letters*, vol. 19, no. 13, pp. 930–932, 1994.
- [3] R. M. Simmons, J. T. Finer, S. Chu, and J. A. Spudich, “Quantitative measurements of force and displacement using an optical trap,” *Biophysical journal*, vol. 70, no. 4, pp. 1813–1822, 1996.
- [4] G. Ranjit, M. Cunningham, K. Casey, and A. A. Geraci, “Zeptonewton force sensing with nanospheres in an optical lattice,” *Physical Review A*, vol. 93, no. 5, p. 053801, 2016.
- [5] U. Bockelmann, P. Thomen, B. Essevaz-Roulet, V. Viasnoff, and F. Heslot, “Unzipping dna with optical tweezers: high sequence sensitivity and force flips,” *Biophysical journal*, vol. 82, no. 3, pp. 1537–1553, 2002.
- [6] S. C. Kuo and M. P. Sheetz, “Force of single kinesin molecules measured with optical tweezers,” *SCIENCE-NEW YORK THEN WASHINGTON-*, vol. 260, pp. 232–232, 1993.
- [7] T. T. Perkins, S. R. Quake, D. E. Smith, S. Chu *et al.*, “Relaxation of a single dna molecule observed by optical microscopy,” *Science-AAAS-Weekly Paper Edition-including Guide to Scientific Information*, vol. 264, no. 5160, pp. 822–825, 1994.
- [8] J. Liphardt, S. Dumont, S. B. Smith, I. Tinoco, and C. Bustamante, “Equilibrium information from nonequilibrium measurements in an experimental test of jarzynskies equality,” *Science*, vol. 296, no. 5574, pp. 1832–1835, 2002.
- [9] D. Collin, F. Ritort, C. Jarzynski, S. B. Smith, I. Tinoco Jr, and C. Bustamante, “Verification of the crooks fluctuation theorem and recovery of rna folding free energies,” *Nature*, vol. 437, no. 7056, p. 231, 2005.
- [10] A. Alemany, A. Mossa, I. Junier, and F. Ritort, “Experimental free-energy measurements of kinetic molecular states using fluctuation theorems,” *Nature Physics*, vol. 8, no. 9, pp. 688–694, 2012.
- [11] J. C. Crocker and D. G. Grier, “Microscopic measurement of the pair interaction potential of charge-stabilized colloid,” *Physical review letters*, vol. 73, no. 2, p. 352, 1994.
- [12] —, “When like charges attract: the effects of geometrical confinement on long-range colloidal interactions,” *Physical review letters*, vol. 77, no. 9, p. 1897, 1996.

- [13] J. C. Crocker, J. Matteo, A. Dinsmore, and A. Yodh, “Entropic attraction and repulsion in binary colloids probed with a line optical tweezer,” *Physical review letters*, vol. 82, no. 21, p. 4352, 1999.
- [14] T. Li, S. Kheifets, D. Medellin, and M. G. Raizen, “Measurement of the instantaneous velocity of a brownian particle,” *Science*, vol. 328, no. 5986, pp. 1673–1675, 2010.
- [15] S. Kheifets, A. Simha, K. Melin, T. Li, and M. G. Raizen, “Observation of brownian motion in liquids at short times: instantaneous velocity and memory loss,” *science*, vol. 343, no. 6178, pp. 1493–1496, 2014.
- [16] A. Ashkin and J. Dziedzic, “Optical levitation in high vacuum,” *Applied Physics Letters*, vol. 28, no. 6, pp. 333–335, 1976.
- [17] T. M. Hoang, R. Pan, J. Ahn, J. Bang, H. T. Quan, and T. Li, “Experimental test of the differential fluctuation theorem and a generalized jarzynski equality for arbitrary initial states,” *Phys. Rev. Lett.*, vol. 120, p. 080602, Feb 2018. [Online]. Available: <https://link.aps.org/doi/10.1103/PhysRevLett.120.080602>
- [18] M. Frimmer, J. Gieseler, T. Ihn, and L. Novotny, “Levitated nanoparticle as a classical two-level atom,” *JOSA B*, vol. 34, no. 6, pp. C52–C57, 2017.
- [19] L. Rondin, J. Gieseler, F. Ricci, R. Quidant, C. Dellago, and L. Novotny, “Direct Measurement of Kramers Turnover with a Levitated Nanoparticle,” *ArXiv e-prints*, Mar. 2017.
- [20] J. E. Curtis and D. G. Grier, “Structure of optical vortices,” *Physical review letters*, vol. 90, no. 13, p. 133901, 2003.
- [21] R. Nambiar and J.-C. Meiners, “Fast position measurements with scanning line optical tweezers,” *Optics letters*, vol. 27, no. 10, pp. 836–838, 2002.
- [22] J. E. Curtis, B. A. Koss, and D. G. Grier, “Dynamic holographic optical tweezers,” *Optics communications*, vol. 207, no. 1, pp. 169–175, 2002.
- [23] F. J. Cao, L. Dinis, and J. M. Parrondo, “Feedback control in a collective flashing ratchet,” *Physical review letters*, vol. 93, no. 4, p. 040603, 2004.
- [24] M. Endres, H. Bernien, A. Keesling, H. Levine, E. R. Anschuetz, A. Krajenbrink, C. Senko, V. Vuletic, M. Greiner, and M. D. Lukin, “Atom-by-atom assembly of defect-free one-dimensional cold atom arrays,” *Science*, p. aah3752, 2016.
- [25] D. Barredo, S. de Léséleuc, V. Lienhard, T. Lahaye, and A. Browaeys, “An atom-by-atom assembler of defect-free arbitrary two-dimensional atomic arrays,” *Science*, vol. 354, no. 6315, pp. 1021–1023, 2016.
- [26] Y. Arita, M. Mazilu, T. Vettenburg, E. M. Wright, and K. Dholakia, “Rotation of two trapped microparticles in vacuum: observation of optically mediated parametric resonances,” *Optics letters*, vol. 40, no. 20, pp. 4751–4754, 2015.
- [27] Y. Arita, E. M. Wright, and K. Dholakia, “Optical binding of two microparticles levitated in vacuum,” *Proc.SPIE*, vol. 10252, pp. 10 252 – 10 252 – 2, 2017. [Online]. Available: <http://dx.doi.org/10.1117/12.2275310>

- [28] L. Allen, M. W. Beijersbergen, R. Spreeuw, and J. Woerdman, “Orbital angular momentum of light and the transformation of laguerre-gaussian laser modes,” *Physical Review A*, vol. 45, no. 11, p. 8185, 1992.
- [29] G. Gibson, J. Courtial, M. J. Padgett, M. Vasnetsov, V. Pas’ko, S. M. Barnett, and S. Franke-Arnold, “Free-space information transfer using light beams carrying orbital angular momentum,” *Optics express*, vol. 12, no. 22, pp. 5448–5456, 2004.
- [30] C. Lutz, M. Kollmann, and C. Bechinger, “Single-file diffusion of colloids in one-dimensional channels,” *Physical review letters*, vol. 93, no. 2, p. 026001, 2004.
- [31] L. P. Faucheux, L. Bourdieu, P. Kaplan, and A. J. Libchaber, “Optical thermal ratchet,” *Physical review letters*, vol. 74, no. 9, p. 1504, 1995.
- [32] T. J. Kippenberg and K. J. Vahala, “Cavity optomechanics: back-action at the mesoscale,” *science*, vol. 321, no. 5893, pp. 1172–1176, 2008.
- [33] M. Aspelmeyer, T. J. Kippenberg, and F. Marquardt, “Cavity optomechanics,” *Rev. Mod. Phys.*, vol. 86, pp. 1391–1452, Dec 2014. [Online]. Available: <https://link.aps.org/doi/10.1103/RevModPhys.86.1391>
- [34] S. Mancini, D. Vitali, and P. Tombesi, “Optomechanical cooling of a macroscopic oscillator by homodyne feedback,” *Physical Review Letters*, vol. 80, no. 4, p. 688, 1998.
- [35] P.-F. Cohadon, A. Heidmann, and M. Pinard, “Cooling of a mirror by radiation pressure,” *Physical Review Letters*, vol. 83, no. 16, p. 3174, 1999.
- [36] O. Arcizet, P.-F. Cohadon, T. Briant, M. Pinard, and A. Heidmann, “Radiation-pressure cooling and optomechanical instability of a micromirror,” *Nature*, vol. 444, no. 7115, pp. 71–74, 2006.
- [37] S. Gigan, H. Böhm, M. Paternostro, F. Blaser, G. Langer, J. Hertzberg, K. C. Schwab, D. Bäuerle, M. Aspelmeyer, and A. Zeilinger, “Self-cooling of a micromirror by radiation pressure,” *Nature*, vol. 444, no. 7115, pp. 67–70, 2006.
- [38] A. Schliesser, P. Del’Haye, N. Nooshi, K. Vahala, and T. Kippenberg, “Radiation pressure cooling of a micromechanical oscillator using dynamical backaction,” *Physical Review Letters*, vol. 97, no. 24, p. 243905, 2006.
- [39] T. Li, S. Kheifets, and M. G. Raizen, “Millikelvin cooling of an optically trapped microsphere in vacuum,” *Nat. Phys.*, vol. 7, p. 527, Mar 2011. [Online]. Available: <https://doi.org/10.1038/nphys1952>
- [40] J. Gieseler, B. Deutsch, R. Quidant, and L. Novotny, “Subkelvin parametric feedback cooling of a laser-trapped nanoparticle,” *Physical review letters*, vol. 109, no. 10, p. 103603, 2012.
- [41] V. Jain, J. Gieseler, C. Moritz, C. Dellago, R. Quidant, and L. Novotny, “Direct measurement of photon recoil from a levitated nanoparticle,” *Phys. Rev. Lett.*, vol. 116, p. 243601, Jun 2016. [Online]. Available: <https://link.aps.org/doi/10.1103/PhysRevLett.116.243601>

- [42] N. Kiesel, F. Blaser, U. DeliĆ, D. Grass, R. Kaltenbaek, and M. Aspelmeyer, “Cavity cooling of an optically levitated submicron particle,” *Proceedings of the National Academy of Sciences*, vol. 110, no. 35, pp. 14 180–14 185, 2013.
- [43] U. DeliĆ, M. Reisenbauer, K. Dare, D. Grass, V. VuletiĆ, N. Kiesel, and M. Aspelmeyer, “Cooling of a levitated nanoparticle to the motional quantum ground state,” *Science*, 2020. [Online]. Available: <https://science.sciencemag.org/content/early/2020/01/29/science.aba3993>
- [44] P. Fonseca, E. Aranas, J. Millen, T. Monteiro, and P. Barker, “Nonlinear dynamics and strong cavity cooling of levitated nanoparticles,” *Physical review letters*, vol. 117, no. 17, p. 173602, 2016.
- [45] P. Barker and M. Shneider, “Cavity cooling of an optically trapped nanoparticle,” *Physical Review A*, vol. 81, no. 2, p. 023826, 2010.
- [46] D. Windey, C. Gonzalez-Ballester, P. Maurer, L. Novotny, O. Romero-Isart, and R. Reimann, “Cavity-based 3d cooling of a levitated nanoparticle via coherent scattering,” *Physical review letters*, vol. 122, no. 12, p. 123601, 2019.
- [47] N. Meyer, A. De los Rios Sommer, P. Mestres, J. Gieseler, V. Jain, L. Novotny, and R. Quidant, “Resolved-sideband cooling of a levitated nanoparticle in the presence of laser phase noise,” *Physical review letters*, vol. 123, no. 15, p. 153601, 2019.
- [48] F. Monteiro, S. Ghosh, A. G. Fine, and D. C. Moore, “Optical levitation of 10-ng spheres with nano-g acceleration sensitivity,” *Physical Review A*, vol. 96, no. 6, p. 063841, 2017.
- [49] J. Ahn, Z. Xu, J. Bang, P. Ju, X. Gao, and T. Li, “Ultrasensitive torque detection with an optically levitated nanorotor,” *Nat. Nanotechnol.*, 2020.
- [50] J. Millen, T. Deesuwana, P. Barker, and J. Anders, “Nanoscale temperature measurements using non-equilibrium brownian dynamics of a levitated nanosphere,” *Nature nanotechnology*, vol. 9, no. 6, pp. 425–429, 2014.
- [51] S. Kuhn, A. Kosloff, B. A. Stickler, F. Patolsky, K. Hornberger, M. Arndt, and J. Millen, “Full rotational control of levitated silicon nanorods,” *Optica*, vol. 4, no. 3, pp. 356–360, 2017.
- [52] S. Kuhn, B. A. Stickler, A. Kosloff, F. Patolsky, K. Hornberger, M. Arndt, and J. Millen, “Optically driven ultra-stable nanomechanical rotor,” *Nature communications*, vol. 8, no. 1, pp. 1–5, 2017.
- [53] J. Ahn, Z. Xu, J. Bang, Y.-H. Deng, T. M. Hoang, Q. Han, R.-M. Ma, and T. Li, “Optically levitated nanodumbbell torsion balance and ghz nanomechanical rotor,” *Phys. Rev. Lett.*, vol. 121, p. 033603, Jul 2018. [Online]. Available: <https://link.aps.org/doi/10.1103/PhysRevLett.121.033603>
- [54] R. Reimann, M. Doderer, E. Hebestreit, R. Diehl, M. Frimmer, D. Windey, F. Tebbenjohanns, and L. Novotny, “Ghz rotation of an optically trapped nanoparticle in vacuum,” *Phys. Rev. Lett.*, vol. 121, p. 033602, Jul 2018. [Online]. Available: <https://link.aps.org/doi/10.1103/PhysRevLett.121.033602>

- [55] Y. Huang, Q. Guo, A. Xiong, T. Li, and Z.-q. Yin, “Time crystal based on a levitated charged nanoparticle,” *arXiv preprint arXiv:2001.10187*, 2020.
- [56] R. P. Feynman, R. B. Leighton, and M. Sands, *The Feynman lectures on physics, Vol. I: The new millennium edition: mainly mechanics, radiation, and heat*. Basic books, 2011, vol. 1.
- [57] M. O. Magnasco, “Forced thermal ratchets,” *Physical Review Letters*, vol. 71, no. 10, p. 1477, 1993.
- [58] J. M. Parrondo and P. Español, “Criticism of feynman’s analysis of the ratchet as an engine,” *American Journal of Physics*, vol. 64, no. 9, pp. 1125–1130, 1996.
- [59] L. Schimansky-Geier, M. Kschischo, and T. Fricke, “Flux of particles in saw-tooth media,” *Physical review letters*, vol. 79, no. 18, p. 3335, 1997.
- [60] T. Hondou and F. Takagi, “Irreversible operation in a stalled state of feynman’s ratchet,” *Journal of the Physical Society of Japan*, vol. 67, no. 9, pp. 2974–2976, 1998.
- [61] M. O. Magnasco and G. Stolovitzky, “Feynman’s ratchet and pawl,” *Journal of statistical physics*, vol. 93, no. 3, pp. 615–632, 1998.
- [62] C. Jarzynski and O. Mazonka, “Feynman’s ratchet and pawl: An exactly solvable model,” *Physical Review E*, vol. 59, no. 6, p. 6448, 1999.
- [63] I. Derényi and R. D. Astumian, “Efficiency of brownian heat engines,” *Physical Review E*, vol. 59, no. 6, p. R6219, 1999.
- [64] C. Van den Broeck, R. Kawai, and P. Meurs, “Microscopic analysis of a thermal brownian motor,” *Physical review letters*, vol. 93, no. 9, p. 090601, 2004.
- [65] J. Zheng, X. Zheng, C. Yam, and G. Chen, “Computer simulation of feynman’s ratchet and pawl system,” *Physical Review E*, vol. 81, no. 6, p. 061104, 2010.
- [66] R. D. Astumian and M. Bier, “Fluctuation driven ratchets: molecular motors,” *Physical review letters*, vol. 72, no. 11, p. 1766, 1994.
- [67] J. Prost, J.-F. Chauwin, L. Peliti, and A. Ajdari, “Asymmetric pumping of particles,” *Physical Review Letters*, vol. 72, no. 16, p. 2652, 1994.
- [68] R. D. Astumian and M. Bier, “Mechanochemical coupling of the motion of molecular motors to atp hydrolysis,” *Biophysical journal*, vol. 70, no. 2, pp. 637–653, 1996.
- [69] A. B. Kolomeisky and B. Widom, “A simplified “ratchet” model of molecular motors,” *Journal of statistical physics*, vol. 93, no. 3-4, pp. 633–645, 1998.
- [70] R. D. Astumian and I. Derényi, “Fluctuation driven transport and models of molecular motors and pumps,” *European biophysics journal*, vol. 27, no. 5, pp. 474–489, 1998.
- [71] N. Metropolis, A. W. Rosenbluth, M. N. Rosenbluth, A. H. Teller, and E. Teller, “Equation of state calculations by fast computing machines,” *The journal of chemical physics*, vol. 21, no. 6, pp. 1087–1092, 1953.

- [72] K. Maruyama, F. Nori, and V. Vedral, “Colloquium: The physics of maxwell’s demon and information,” *Reviews of Modern Physics*, vol. 81, no. 1, p. 1, 2009.
- [73] J. M. Parrondo, J. M. Horowitz, and T. Sagawa, “Thermodynamics of information,” *Nature physics*, vol. 11, no. 2, 2015.
- [74] D. Mandal and C. Jarzynski, “Work and information processing in a solvable model of maxwell’s demon,” *Proceedings of the National Academy of Sciences*, vol. 109, no. 29, pp. 11 641–11 645, 2012.
- [75] S. Ito and T. Sagawa, “Maxwell/’s demon in biochemical signal transduction with feedback loop,” *Nature communications*, vol. 6, 2015.
- [76] S. Toyabe and M. Sano, “Nonequilibrium fluctuations in biological strands, machines, and cells,” *Journal of the Physical Society of Japan*, vol. 84, no. 10, p. 102001, 2015.
- [77] F. Jülicher, A. Ajdari, and J. Prost, “Modeling molecular motors,” *Reviews of Modern Physics*, vol. 69, no. 4, p. 1269, 1997.
- [78] R. M. Pettit, W. Ge, P. Kumar, D. R. Luntz-Martin, J. T. Schultz, L. P. Neukirch, M. Bhattacharya, and A. N. Vamivakas, “An optical tweezer phonon laser,” *Nature Photonics*, vol. 13, no. 6, pp. 402–405, 2019.
- [79] D. E. Chang, C. Regal, S. Papp, D. Wilson, J. Ye, O. Painter, H. J. Kimble, and P. Zoller, “Cavity opto-mechanics using an optically levitated nanosphere,” *Proceedings of the National Academy of Sciences*, vol. 107, no. 3, pp. 1005–1010, 2010.
- [80] Y. Arita, M. Mazilu, and K. Dholakia, “Laser-induced rotation and cooling of a trapped microgyroscope in vacuum,” *Nature communications*, vol. 4, p. 2374, 2013.
- [81] J. Millen, P. Z. G. Fonseca, T. Mavrogordatos, T. S. Monteiro, and P. F. Barker, “Cavity cooling a single charged levitated nanosphere,” *Phys. Rev. Lett.*, vol. 114, p. 123602, Mar 2015. [Online]. Available: <https://link.aps.org/doi/10.1103/PhysRevLett.114.123602>
- [82] D. C. Moore, A. D. Rider, and G. Gratta, “Search for millicharged particles using optically levitated microspheres,” *Physical review letters*, vol. 113, no. 25, p. 251801, 2014.
- [83] B. R. Slezak, C. W. Lewandowski, J.-F. Hsu, and B. D’Urso, “Cooling the motion of a silica microsphere in a magneto-gravitational trap in ultra-high vacuum,” *New Journal of Physics*, vol. 20, no. 6, p. 063028, 2018.
- [84] O. Romero-Isart, M. L. Juan, R. Quidant, and J. I. Cirac, “Toward quantum superposition of living organisms,” *New Journal of Physics*, vol. 12, no. 3, p. 033015, 2010.
- [85] H. Shi and M. Bhattacharya, “Coupling a small torsional oscillator to large optical angular momentum,” *Journal of Modern Optics*, vol. 60, no. 5, pp. 382–386, 2013.

- [86] T. M. Hoang, Y. Ma, J. Ahn, J. Bang, F. Robicheaux, Z.-Q. Yin, and T. Li, “Torsional optomechanics of a levitated nonspherical nanoparticle,” *Physical review letters*, vol. 117, no. 12, p. 123604, 2016.
- [87] B. A. Stickler, B. Schirnski, and K. Hornberger, “Rotational friction and diffusion of quantum rotors,” *Phys. Rev. Lett.*, vol. 121, p. 040401, Jul 2018. [Online]. Available: <https://link.aps.org/doi/10.1103/PhysRevLett.121.040401>
- [88] M. Rashid, M. Toroš, A. Setter, and H. Ulbricht, “Precession motion in levitated optomechanics,” *Phys. Rev. Lett.*, vol. 121, p. 253601, Dec 2018. [Online]. Available: <https://link.aps.org/doi/10.1103/PhysRevLett.121.253601>
- [89] T. Seberston and F. Robicheaux, “Parametric feedback cooling of rigid body nanodumbbells in levitated optomechanics,” *Phys. Rev. A*, vol. 99, p. 013821, Jan 2019. [Online]. Available: <https://link.aps.org/doi/10.1103/PhysRevA.99.013821>
- [90] Z. Xu and T. Li, “Detecting casimir torque with an optically levitated nanorod,” *Phys. Rev. A*, vol. 96, p. 033843, Sep 2017. [Online]. Available: <https://link.aps.org/doi/10.1103/PhysRevA.96.033843>
- [91] W. Lechner, S. Habraken, N. Kiesel, M. Aspelmeyer, and P. Zoller, “Cavity optomechanics of levitated nanodumbbells: Nonequilibrium phases and self-assembly,” *Physical review letters*, vol. 110, no. 14, p. 143604, 2013.
- [92] B. A. Stickler, B. Papendell, S. Kuhn, B. Schirnski, J. Millen, M. Arndt, and K. Hornberger, “Probing macroscopic quantum superpositions with nanorotors,” *New J. Phys.*, vol. 20, no. 12, p. 122001, 2018.
- [93] S. Singh, G. Phelps, D. Goldbaum, E. M. Wright, and P. Meystre, “All-optical optomechanics: an optical spring mirror,” *Physical review letters*, vol. 105, no. 21, p. 213602, 2010.
- [94] A. Arvanitaki and A. A. Geraci, “Detecting high-frequency gravitational waves with optically levitated sensors,” *Physical review letters*, vol. 110, no. 7, p. 071105, 2013.
- [95] P. M. Johnson, C. M. van Kats, and A. van Blaaderen, “Synthesis of colloidal silica dumbbells,” *Langmuir*, vol. 21, no. 24, pp. 11 510–11 517, 2005.
- [96] T. Li, *Fundamental tests of physics with optically trapped microspheres*. Springer Science & Business Media, 2012.
- [97] J. Millen, T. S. Monteiro, R. Pettit, and A. N. Vamivakas, “Optomechanics with levitated particles,” *Rep. Prog. Phys.*, vol. 83, p. 026401, 2020.
- [98] Z.-Q. Yin, A. A. Geraci, and T. Li, “Optomechanics of levitated dielectric particles,” *Int. J. Mod. Phys. B*, vol. 27, no. 26, p. 1330018, 2013.
- [99] F. Tebbenjohanns, M. Frimmer, A. Militaru, V. Jain, and L. Novotny, “Cold damping of an optically levitated nanoparticle to microkelvin temperatures,” *Phys. Rev. Lett.*, vol. 122, p. 223601, Jun 2019. [Online]. Available: <https://link.aps.org/doi/10.1103/PhysRevLett.122.223601>

- [100] F. Tebbenjohanns, M. Frimmer, V. Jain, D. Windey, and L. Novotny, "Motional sideband asymmetry of a nanoparticle optically levitated in free space," *Phys. Rev. Lett.*, vol. 124, p. 013603, Jan 2020. [Online]. Available: <https://link.aps.org/doi/10.1103/PhysRevLett.124.013603>
- [101] E. F. Schubert, *Light-emitting diodes*. New York: Cambridge University Press, 2006.
- [102] L. Novotny, R. X. Bian, and X. S. Xie, "Theory of nanometric optical tweezers," *Physical Review Letters*, vol. 79, no. 4, p. 645, 1997.
- [103] V. Kaajakari *et al.*, *Practical MEMS: Design of microsystems, accelerometers, gyroscopes, RF MEMS, optical MEMS, and microfluidic systems*. Small Gear Publishing, 2009.
- [104] D. Kleckner and D. Bouwmeester, "Sub-kelvin optical cooling of a micromechanical resonator," *Nature*, vol. 444, no. 7115, pp. 75–78, 2006.
- [105] M. Poggio, C. Degen, H. Mamin, and D. Rugar, "Feedback cooling of a cantilever's fundamental mode below 5 mk," *Physical Review Letters*, vol. 99, no. 1, p. 017201, 2007.
- [106] T. Corbitt, C. Wipf, T. Bodiya, D. Ottaway, D. Sigg, N. Smith, S. Whitcomb, and N. Mavalvala, "Optical dilution and feedback cooling of a gram-scale oscillator to 6.9 mk," *Physical Review Letters*, vol. 99, no. 16, p. 160801, 2007.
- [107] J. Chan, T. M. Alegre, A. H. Safavi-Naeini, J. T. Hill, A. Krause, S. Gröblacher, M. Aspelmeyer, and O. Painter, "Laser cooling of a nanomechanical oscillator into its quantum ground state," *Nature*, vol. 478, no. 7367, pp. 89–92, 2011.
- [108] Y. Zheng, G.-C. Guo, and F.-W. Sun, "Cooling of a levitated nanoparticle with digital parametric feedback," *Applied Physics Letters*, vol. 115, no. 10, p. 101105, 2019.
- [109] J. Vovrosh, M. Rashid, D. Hempston, J. Bateman, M. Paternostro, and H. Ulbricht, "Parametric feedback cooling of levitated optomechanics in a parabolic mirror trap," *JOSA B*, vol. 34, no. 7, pp. 1421–1428, 2017.
- [110] J. Gieseler, *Dynamics of optically levitated nanoparticles in high vacuum*. Universitat Politècnica de Catalunya, 2014.
- [111] J. Gieseler, L. Novotny, and R. Quidant, "Thermal nonlinearities in a nanomechanical oscillator," *Nat. Phys.*, vol. 9, p. 806, Nov 2013. [Online]. Available: <https://doi.org/10.1038/nphys2798>
- [112] J. F. Rhoads, S. W. Shaw, and K. L. Turner, "The nonlinear response of resonant microbeam systems with purely-parametric electrostatic actuation," *Journal of Micromechanics and Microengineering*, vol. 16, no. 5, p. 890, 2006.
- [113] J. F. Rhoads, S. W. Shaw, K. L. Turner, J. Moehlis, B. E. DeMartini, and W. Zhang, "Generalized parametric resonance in electrostatically actuated microelectromechanical oscillators," *Journal of Sound and Vibration*, vol. 296, no. 4-5, pp. 797–829, 2006.

- [114] H. Cho, M.-F. Yu, A. F. Vakakis, L. A. Bergman, and D. M. McFarland, “Tunable, broadband nonlinear nanomechanical resonator,” *Nano letters*, vol. 10, no. 5, pp. 1793–1798, 2010.
- [115] S. C. Stanton, C. C. McGehee, and B. P. Mann, “Nonlinear dynamics for broadband energy harvesting: Investigation of a bistable piezoelectric inertial generator,” *Physica D: Nonlinear Phenomena*, vol. 239, no. 10, pp. 640–653, 2010.
- [116] H. Cho, B. Jeong, M.-F. Yu, A. F. Vakakis, D. M. McFarland, and L. A. Bergman, “Nonlinear hardening and softening resonances in micromechanical cantilever-nanotube systems originated from nanoscale geometric nonlinearities,” *International Journal of Solids and Structures*, vol. 49, no. 15-16, pp. 2059–2065, 2012.
- [117] S. Qvarfort, A. Serafini, P. F. Barker, and S. Bose, “Gravimetry through nonlinear optomechanics,” *Nat. commun.*, vol. 9, no. 1, p. 3690, 2018.
- [118] M. Yoneda and K. Aikawa, “Thermal broadening of the power spectra of laser-trapped particles in vacuum,” *J. Phys. B: At. Mol. Opt. Phys.*, vol. 50, no. 24, p. 245501, 2017.
- [119] R. L. Badzey and P. Mohanty, “Coherent signal amplification in bistable nanomechanical oscillators by stochastic resonance,” *Nature*, vol. 437, no. 7061, p. 995, 2005.
- [120] Z. Liu, C. Guo, J. Yang, and L. Yuan, “Tapered fiber optical tweezers for microscopic particle trapping: fabrication and application,” *Optics express*, vol. 14, no. 25, pp. 12 510–12 516, 2006.
- [121] M. L. Juan, M. Righini, and R. Quidant, “Plasmon nano-optical tweezers,” *Nature photonics*, vol. 5, no. 6, p. 349, 2011.
- [122] J. C. Ndukaife, A. V. Kildishev, A. G. A. Nnanna, V. M. Shalaev, S. T. Wereley, and A. Boltasseva, “Long-range and rapid transport of individual nano-objects by a hybrid electrothermoplasmonic nanotweezer,” *Nature nanotechnology*, vol. 11, no. 1, p. 53, 2016.